IOWA STATE UNIVERSITY
Digital Repository

Graduate Theses and Dissertations

Iowa State University Capstones, Theses and Dissertations

2016

Mixed mode transition to turbulence in boundary layers

Rikhi Bose
Iowa State University

Follow this and additional works at: http://lib.dr.iastate.edu/etd

 Part of the Aerospace Engineering Commons

Recommended Citation
Bose, Rikhi, "Mixed mode transition to turbulence in boundary layers" (2016). *Graduate Theses and Dissertations*. 15882.
http://lib.dr.iastate.edu/etd/15882

This Dissertation is brought to you for free and open access by the Iowa State University Capstones, Theses and Dissertations at Iowa State University Digital Repository. It has been accepted for inclusion in Graduate Theses and Dissertations by an authorized administrator of Iowa State University Digital Repository. For more information, please contact digirep@iastate.edu.

Mixed mode transition to turbulence in boundary layers

by

Rikhi Bose

A dissertation submitted to the graduate faculty

in partial fulfillment of the requirements for the degree of

DOCTOR OF PHILOSOPHY

Major: Aerospace Engineering

Program of Study Committee:

Paul A. Durbin, Major Professor

Jonathan Regele

Anupam Sharma

Hailiang Liu

Ming-Chen Hsu

Iowa State University

Ames, Iowa

2016

Copyright © Rikhi Bose, 2016. All rights reserved.

DEDICATION

To my Baba, Ma, Didi and Projesh ...

TABLE OF CONTENTS

LIST OF TABLES

LIST OF FIGURES

ACKNOWLEDGEMENTS

I express my sincere gratitude to my thesis supervisor Professor Paul Durbin, for providing the opportunity to work with him. His wisdom and knowledge has enriched my understanding of fluid dynamics. I consider myself fortunate to have been a part of his research group. I will also like to take this opportunity to thank Professor Tamer Zaki of John Hopkins University who provided the code used for the simulations. He always lent a patient ear whenever I approached him with a problem.

I have had the opportunity to have glorious labmates from whom I have learnt a lot. Their tenacity will remain as examples to emulate for my future endeavours. I will also like to thank all my friends with whom I have spent three good years at Ames. My father, mother and elder sister have always motivated me. I sincerely thank Professor Tapan K. Sengupta of IIT Kanpur for believing in me, which remains a great source of inspiration. Lastly, I thank my friend Projesh for supporting me through thick and thin. Without his insistence, probably I would not have completed this work.

ABSTRACT

Boundary layer transition has been investigated by means of direct numerical simulation. The incompressible Navier Stokes equations have been solved for flow over a smooth flat plate. General consensus is that laminar to turbulent transition is via orderly or bypass route. The motivation of the present simulations is to specifically study the transition mechanisms when precursor of orderly transition, the Tollmien-Schlichting waves and the precursor of bypass transition, the Klebanoff streaks, both take part in triggering transition, when neither by itself is sufficient. *Mixed mode* transition has been studied in both Blasius and adverse pressure gradient boundary layers. The Klebanoff streaks are instigated inside the boundary layer by invoking free-stream turbulence at inlet. Time-periodic TS wave eigenfunction has been superimposed to the inlet velocity profile. In adverse pressure gradient, the TS waves are spontaneously excited.

In both zero and adverse pressure gradients, three transition routes are obtained depending on perturbation magnitudes of the TS wave and intensity of free-stream turbulence. When intensity of free-stream turbulence is low, transition is via distortion of TS waves. Λ vortices form and their breakdown triggers transition. When intensity of free-stream turbulence is high, classical bypass transition is recovered. When the strength of both the TS wave and free-stream disturbances are low, transition is via apparent interaction of the TS waves and Klebanoff streaks. Helical structures form and break down to trigger transition. The critical layer of the helical instability is close to the wall. Previous studies demonstrate that the outer mode breakdown is most dominant in Blasius boundary layer. The inner mode has been found to be dominant in adverse pressure gradient boundary layers. Present simulations provide a clearer picture. The inner modes could also be dominant in zero pressure gradient boundary layers, provided, instability waves are present and the intensity of free-stream turbulence is about 1%. The outer modes are consequence of high amplitude Klebanoff streaks instigated

by high intensity free-stream turbulence. Stronger Klebanoff streaks stabilize the base profile and consequently the instability waves. Therefore, inner breakdown is suppressed.

Simulations in adverse pressure gradient demonstrate that the spontaneously excited instability waves are highly receptive to the inlet disturbance spectra. The growth rate of the instability waves are much higher due to inflectional base profile so that these could potentially couple with the Klebanoff streaks. The instability waves could be identified inside the boundary layer even at high levels of free-stream forcing. The instability waves were found to participate in transition process in all the cases simulated. This indicates that in adverse pressure gradient boundary layers, mixed mode transition is almost always relevant.

CHAPTER 1. INTRODUCTION

Many flows in engineering applications have an initial regime where flow transitions from laminar to turbulent. The consequence is higher friction and heat transfer at the boundary. In many applications this may be desired and in others, disadvantageous. For example, in heat exchangers turbulent flow increases the heat exchange efficiency. Alternatively, turbulent flow over turbine blades or airplane wings increases drag and fuel consumption. Therefore, understanding the mechanisms of transition to turbulence is pertinent to better engineering design and efficiency.

This thesis is on mechanisms of instability and transition in *mixed mode* transitional boundary layer flows. In the following sections a review of the modes at play triggering transition to turbulence in boundary layers is presented followed by a brief description of literature on mixed mode transition.

1.1 Orderly transition via Tollmien-Schlichting waves

The phenomenon of boundary layer transition has been rigorously studied now for more than the past hundred years. Initial development in the field was mainly based on linear theory. Rayleigh and Fjortoft's theorems disguised the fact that viscosity may play a role in transition. Initial contributions to linear viscous stability theory for boundary layers came from Heisenberg (1951), Tollmien (1929) and Schlichting (1933). They showed viscosity may also destabilize the boundary layer; for instance, the zero-pressure-gradient (ZPG) Blasius boundary layer is inviscidly stable. Linear viscous stability theory describes exponentially growing instability waves inside the boundary layer that arise through amplification of very small initial background disturbances. The wave-like perturbations, now known as 'Tollmien-

Schlichting' (TS) waves may be predicted from solution of the linear perturbation equations, the Orr-Sommerfeld equations. These waves were not detected until the 1940's, when Schubauer and Skramstad (1947) could identify the TS waves in lab experiments.

Experimentally, the TS waves are instigated by wall excitation or by acoustic waves. Otherwise, these waves could be excited by mechanisms such as leading edge scattering of free-stream vorticity and sound (Goldstein, 1983), or discontinuities in surface curvature, or inhomogeneities (Crouch, 1992). The process of longer and faster disturbances in the free-stream being converted to shorter and slower instability waves inside boundary layer is known as receptivity (Saric et al., 2002). TS waves are 2-D waves, invariant in the spanwise direction, which grow at a slow, viscous rate. These are only observed experimentally when the background disturbances are very low (typically $\sim 0.1\%$ of free-stream velocity U_∞). The appearance of TS waves does not ensure transition to turbulence. The instability waves grow beyond the critical point until the upper branch of the Neutral stability curve, followed by decay. They remain fairly organized if the amplitude does not reach sufficiently high magnitude, typically $\sim 1\%U_\infty$. At this stage spanwise variations develop. Instability waves become 3-D. Three dimensionality is due to parametric resonance between infinitesimal perturbations and a periodic base state, consisting of the boundary layer and finite amplitude instability waves. This was analyzed using a Floquet, secondary perturbation expansion by Herbert (1988). The perturbations at this stage are characterized by peaks and valleys. In the vorticity field, the 3-D phase is represented by Λ vortices (Klebanoff et al., 1962). At least three types of secondary instability are known – K, H and C type. These are due the alignment of the Λ vortices. Herbert (1988) attributed their appearance to subharmonic (H or C type) and fundamental (K type) resonance. Exact flow condition behind the appearance of each class of pattern is not yet known. In their DNS simulations, Bhaumik and Sengupta (2014) obtained K and H type transitions for high and low frequency wall forcing, respectively.

Λ vortices grow at a much higher rate than the parent TS wave due to resonance. This is followed by breakdown of these vortices and thence transition to turbulence is triggered. Transition is accomplished approximately at Reynolds number based on momentum thickness $Re_\theta \sim 5000$. The sporadic turbulent patches in an otherwise laminar flow was first discovered

by Emmons (1951). The leading and trailing parts of a turbulent spot travel with approximately U_∞ and $0.5U_\infty$ (Hodson and Howell, 2005). The turbulent spots spread in both streamwise and spanwise directions. The turbulent spots merge and transition to turbulence is accomplished.

1.2 Bypass transition

In their review article on DNS simulations of TS waves, Kleiser and Zang (1991) insinuated about 'transition induced by *mysterious* bypass mechanisms'. The word 'bypass' (Morkovin, 1969) was intended to represent all possible transition scenarios that exclude the TS waves. In many flow conditions the disturbance level is too high for the flow field to remain linear. In flow over turbine blades for example the wakes from the trailing edge of leading blade impinge upon the trailing blade and trigger transition. The free-stream turbulence intensity of the wakes are typically large ($Tu \sim 5\%U_\infty$). The disturbances grow at an inertial time scale and therefore the TS waves, growing at a slow viscous time scale may become redundant. In recent literature, bypass mechanism has become synonymous to transition beneath high intensity free-stream turbulence.

Westin et al. (1994) and Boiko et al. (1994) performed experiments to investigate boundary layer characteristics upstream of transition onset beneath nearly isotropic free-stream turbulence. It was observed, that, though the free-stream disturbances were broadband, the disturbance energy inside the boundary layer was mainly at low frequencies. The disturbances inside the boundary layer was primarily due to streamwise fluctuations. They also found that the rms of streamwise fluctuation velocity scales linearly with downstream distance. Contribution of low frequency components was the most towards the growth of the streamwise disturbances. The low frequency streamwise perturbations are boundary layer response to broadband free-stream turbulence, named as 'Klebanoff modes' by Kendall (1985) even though these can not be classified as 'modal' perturbations. Westin et al. (1994) also reported that these Klebanoff streaks had spanwise width of the size of boundary layer thickness. It is to be noted that anisotropy of the turbulence in free-stream may greatly alter the characteristics of the Klebanoff streaks (Leib et al., 1999). Specifically low frequency components may have a profound effect on the velocity fluctuations inside the boundary layer.

The Klebanoff modes have received a great deal of attention since it's identification. Their low frequency nature has been explained by the concept of shear sheltering (Hunt and Durbin, 1999). Boundary layer shear basically acts as a low pass filter to allow only low frequency components to penetrate inside it. The continuous modes of the Orr-Sommerfeld equation, first theorized by Grosch and Salwen (1978) and Salwen and Grosch (1981) also have the same property. The eigenmodes oscillate in free-stream but is damped inside the boundary layer. Jacobs and Durbin (1998) showed that the signature of low frequency continuous modes penetrate deeper inside boundary layer. Also, disturbances penetrate deeper at lower Reynolds numbers. These aspects make the continuous mode spectrum of the OS and Squire equations appropriate for modelling synthetic free-stream turbulence downstream of the leading edge and its signature inside the boundary layer. These modes have been used to generate the inflow turbulence herein.

The property of algebraic growth of the Klebanoff streaks has been thoroughly investigated as well. The growth is dictated by inviscid mechanism followed by viscous decay. The algebraic instability of the streamwise perturbation component amplifies due to shearing effect, was shown using rapid distortion theory by Phillips (1969). The physical mechanism governing the growth of these disturbances is attributed to lift-up of the mean momentum. This result was derived using variational formulation by (Butler and Farrell, 1992). Similar conclusions with other mathematical formulations were obtained by Andersson et al. (1999) and Luchini (2000). Zaki and Durbin (2005) showed similar lift-up of Klebanoff streaks inside boundary layer by summing up the Squire response to a monochromatic Orr-Sommerfeld continuous mode forcing. In these formulations, the lift-up effect is due to the nonsecular growth of perturbations due to the mutual forcing in the Orr-Sommerfeld and Squire coupled system of equations.

Even though Klebanoff streaks were identified as a precursor to bypass transition, it's connection to transition to turbulent spots remained unclear (Klebanoff, 1971). Direct simulations of bypass transition performed by Jacobs and Durbin (2000) shed light on the associated processes. They synthesized inflow turbulence using continuous modes. In their simulation, Klebanoff streaks amplified and lifted up close to the boundary layer edge, where high frequency free-stream disturbances initiated breakdown to turbulent spots. All laminar streaks do not

breakdown to turbulent spots. Prior to breakdown Klebanoff streaks attained amplitudes of the order of $20\%U_\infty$. Bimodal interaction work by Zaki and Durbin (2005) corroborated the same. Later several direct simulation studies were performed to study the bypass transition which elaborate a great deal about the final stages of transition. Simulations by Brandt et al. (2004), Nagarajan et al. (2007) and Ovchinnikov et al. (2008) to name a few of those works. The sinuous and varicose streak instability modes were proposed as precursors to turbulent spots using Floquet expansion of the secondary perturbations by Andersson et al. (2001). Brandt et al. (2004) identified the sinuous and varicose streak instabilities prior to streak breakdown in their DNS. Nagarajan et al. (2007) included the leading edge in their simulations. For a slender leading edge, streak instability was similar to Jacobs and Durbin (2000). But for a blunt leading edge, breakdown was via streamwise wave-like disturbances. In recent direct simulations and stability calculations by Vaughan and Zaki (2011) and Hack and Zaki (2014), these streak instability modes have been identified as *outer sinuous* and *inner varicose* modes respectively. 'Inner' or 'outer' nomenclature of these secondary perturbations are due to the relevant critical layers with respect to the local boundary layer thickness. A new class of inner instabilities has been identified in the present work.

1.3 Mixed mode transition

Several simulation and experimental results have indicated modal interaction between the Klebanoff streaks and TS waves. Yet, this transition scenario is less explored. Hughes and Walker (2001) obtained instability waves from surface stress measurements on the suction side of a compressor blade. The stator blade was situated downstream of a rotor blade. Hence it was a case of interaction of wakes with a boundary layer. They found out growing instability waves prior to turbulent spot formation and concluded that there are regimes where transition is neither orderly nor bypass. Similar indications were also obtained from simulations of flat plate boundary layer including the leading edge by Nagarajan et al. (2007). They obtained growing wave packets for a blunt leading edge geometry even in presence of Klebanoff streaks. These instability wave packets were of higher frequency than the TS wave packets. They concluded that the instability waves are generated due to wrapping up of long vortices around the leading

edge. Zaki et al. (2010) performed simulations of bypass transition over compressor blade. High intensity free-stream turbulence obtained from isotropic turbulence box simulation was used at inlet to perturb the flow. They observed 2-D waves on the suction side of the boundary layer without free-stream perturbation. In the free-stream disturbance cases, locally coherent 2-D instability waves were observed on the suction side of the blade. Therefore, there have been plenty of implications either from high-fidelity simulations or experiments of a mixed mode transition to turbulence route, different from purely orderly or bypass routes. Perhaps the mixed mode transition is much more relevant in adverse pressure gradient boundary layers. In adverse pressure gradient, due to highly inflectional base flow profiles, the growth rate of the TS mode is much larger. The TS waves can potentially engage in modal interaction with the Klebanoff streaks.

When both Klebanoff streaks and TS waves are present in the disturbance spectrum, the transition route is less clear. Their interaction might have contrasting effects. Flow could be stabilized and at the same time, there is evidence, that unsteady streaks could have destabilizing effect. Most of these results are from highly idealized simulations or experiments. Cossu and Brandt (2004) showed that the steady Klebanoff streaks stabilize the TS waves by decreasing the growth rate of the varicose fundamental mode. The reason of stabilization was attributed to the negative production of fluctuation energy due to the spanwise component. Experimental work by Fransson et al. (2005) and Fransson et al. (2006) agreed with the stability analysis results of Cossu and Brandt (2004). But when unsteady streaks were included in experiments performed by Boiko et al. (1994), the results were puzzling. TS waves were excited by a vibrating ribbon while ambient turbulence in the free-stream was about $Tu \approx 1.5\%$. The Klebanoff streaks induced inside the boundary layer were able to stabilize the TS wave growth rate, yet, transition was triggered at a lower Reynolds number compared to the case without the TS wave. Similar results have been obtained herein.

Fasel (2002) performed DNS simulations of modal interaction of Klebanoff streaks and TS waves. The monochromatic streaks were forced using volume forcing to generate low frequency streamwise vortices outside the boundary layer. Breakdown to turbulence was through formation of Λ vortices in K type pattern. It is to be pointed out that the interaction due to unsteady

streaks and TS waves are likely to generate oblique waves. The fact that the formation of Λ vortices are dependent on the frequency-wavenumber combination, is intuitive.

Perhaps, simulations most relevant to present simulations using broadband free-stream turbulence were by Liu et al. (2008a). They performed direct simulations of interaction of continuous and discrete mode disturbances. Klebanoff streaks forced by a monochromatic continuous mode interacted with TS wave inside the boundary layer. Inclusion of only monochromatic disturbances ensure a tidy boundary layer upstream of transition which makes it easier to identify the precursors. The disturbance eigenfunctions were prescribed at inlet downstream of the leading edge. The TS wave amplitude was high $1\%U_\infty$ at inlet. Interaction led to breakdown by formation of Λ-like vortical structures. They used continuous modes with both wide and narrow wavelengths. The interaction and vortex pattern evolution in wide streak cases in their work were forced by the incoming OS continuous mode. The spanwise wavelength of the Λ vortices exactly matched with the OS continuous mode wavelength and the streamwise pattern had been attributed to the difference in phase speeds of the discrete and continuous modes. The Klebanoff streaks distorted the TS waves to trigger early transition. In their narrower streaks cases, the width of the narrow streaks was similar to Klebanoff streaks forced by broadband disturbances. The breakdown was again through breakdown of Λ vortices. The width of the vortices was no more locked to the OS continuous mode. Rather, the width of the vortices was even larger than the wider streaks cases. Also, increasing continuous mode amplitude resulted in transition delay. Both narrow and wide streaks suppress the TS waves. The argument was that high amplitude wide streak cases promoted transition by augmenting secondary instability. Wide streaks ensure higher distortion. But in narrow streaks cases, transition is delayed. The distortion effect is less for narrow streaks. So the TS waves require to travel larger streamwise distance to reach sufficient amplitude for secondary instability. Transition is thereby delayed.

Their Floquet analysis of the same base flow ansatz (Liu et al., 2008b) was able to clarify the conclusions from DNS. The wide streak breakdown was due to fundamental parametric resonance while the narrow streak cases due to detuned parametric resonance. Though both wide and narrow streaks stabilize the TS wave, the fundamental secondary instability growth rate was higher resulting in early transition in DNS. The detuned secondary instability of

narrow streaks cases remained unaltered. Hence transition was delayed. Apart from their interesting results, it should be pointed out is that, even though these simulations give good insight into the interaction process and TS wave stabilization, monochromatic excitations do not account for the bypass transition scenario. At least two distinct continuous mode perturbations are necessary to incorporate bypass transition due to broadband free-stream turbulence, was shown by Zaki and Durbin (2005). Even then, the results represent highly idealized situations.

1.4 Motivation

Mixed mode transition might be as rapid as bypass transition. This is intriguing. The two modes individually might not be dangerous enough to trigger transition, but in presence of both, transition onset could be as early as in bypass. The TS mode might be stabilized, yet, transition onset might be delayed or it might be quicker than bypass transition, even under low disturbance conditions.

The main motivation of the present simulations arise from the startling observations by Liu et al. (2008a) and Zaki et al. (2010). In ZPG boundary layers, bypass route is very dominant over the instability waves. Yet, in bimodal idealized streak-TS mode interaction by Liu et al. (2008a), inclusion of both, a high amplitude TS wave ($1\%U_\infty$ at inlet) and a continuous mode ($\sim 1\%$ at inlet) were necessary to trigger the breakdown around $Re_x \approx 4.5 \times 10^5$. Moreover, as mentioned already, the pure bypass route was not included due to presence of a single continuous mode. In presence of broadband free-stream turbulence, a lot of fundamental questions arise. The TS wave is likely to be suppressed, but then how does it trigger early transition? Does the narrow streak simulations by Liu et al. (2008a) more relevant, or is there probability of alternate routes? The Floquet analysis and DNS of wide streaks (Liu et al., 2008b) also seem peculiar due to the mode locking of primary and secondary disturbances. Intuitively it is unlikely that the breakdown would be only by Λ vortices under broadband free-stream forcing, specifically when the TS mode strength is lower. What is the transition route when both free-stream forcing and TS mode strength are large. Does the 'inner' mode or the 'outer' mode prevail and when? Expectedly far more complex picture of mixed mode transition under realistic vortical disturbance conditions is not yet known. An interaction is expected. Those are obviously

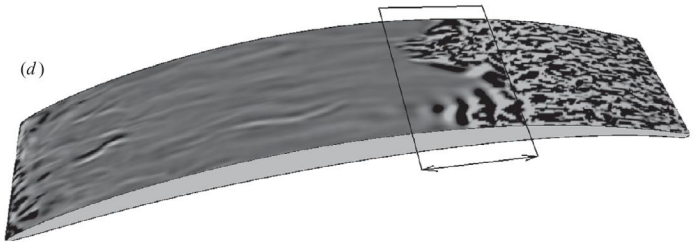

Figure 1.1: A discrete mode identifiable in the wall normal perturbation contours in the APG section in the suction side of a compressor blade.

not expected to be as clear as idealized simulations. These open questions motivate the ZPG simulations of the present research.

Mixed mode transition is a far more likely scenario in APG which has been identified experimentally and in simulations (Hughes and Walker, 2001; Zaki et al., 2010). Figure 1.1 shows such locally 2-D instability waves in the APG section in the suction side of a compressor blade from simulations by Zaki et al. (2010). The instability waves are spontaneously excited which have been identified in experiments as well (Walker and Gostelow, 1989). Walker and Gostelow (1989) and Gostelow et al. (1994) speculated that these instability waves participate in transition. The breakdown is by an inflectional instability in the wall normal profile of velocity. The discrete mode growth is much higher in APG. Therefore, an interaction is more likely even at moderate intensity free-stream turbulence. Zaki and Durbin (2006) demonstrated that coupling of boundary layer disturbances to continuous modes is higher in APG. They argued that higher coupling forces Klebanoff streaks of higher amplitude and triggers early transition. So, amplitudes of both Klebanoff streaks and instability waves increase. Therefore it is not evident whether mixed mode transition or the pure bypass route is the dominant route in APG. Both orderly and bypass transition in APG is dominated by 'inner varicose' mode precursors to breakdown (Vaughan and Zaki, 2011; Hack and Zaki, 2014). Could the interaction somehow alter the inner mode precursor? How could possibly the shift in critical layer from dominant outer mode (in ZPG) to inner mode (in APG) takes place? Mode interaction could be the answer.

1.5 Organization

The dissertation contains four chapters. A brief introduction of the orderly, bypass as well as mixed mode transition in boundary layer flows and the associated processes have been described in Chapter 1. Chapter 2 contains brief descriptions of the DNS domain, on the synthesis of the inlet free-stream turbulence, a very brief description of the numerical methods used for discretization. Results of the mixed mode transition simulations in ZPG and the obtained flow regimes have been characterized in detail, also in Chapter 2 using qualitative data and visualizations. Similar detail about the simulations performed with adversity in pressure gradient has been given in Chapter 3. It describes details about the base flow generation, instability of the base flow followed by the results. Finally, in Chapter 4, conclusions have been drawn.

1.5.1 Key results

- Neither the TS mode nor free-stream turbulence of $Tu = 1\%$ or 2% was sufficient to trigger transition in the computational domain in ZPG simulations. Their interaction triggered transition. For the strong TS mode case, the transition was almost at the same Reynolds number as in bypass transition beneath free-stream turbulence of $Tu = 3.5\%$.

- Three transitional regimes have been identified for the ZPG simulations depending on the strength of modes at inlet: secondary instability of TS mode, streak instability and pure bypass transition.

- Breakdown through formation of Λ vortices are not the only mixed mode route. Inclusion of broadband spectrum ensures recovery of bypass transition when free-stream forcing is high. A complete picture of mixed mode transition under more realistic conditions is obtained.

- The TS mode is indeed stabilized by the unstable Klebanoff streaks. The decay starts earlier. But nonetheless, early transition is triggered. The flow destabilization is probably due to increased growth rate of streaks when the base flow consisting of TS mode and

Blasius profile is unsteady (Vaughan and Zaki, 2011). Breakdown is via inner mode. The threshold streak amplitude required for inner mode transition is also lower.

- Discrete instability waves are instigated spontaneously in APG simulations as observed in experiments by Walker and Gostelow (1989); Gostelow et al. (1994). The discrete modes could be obtained even without free-stream turbulence being employed at inlet! How the free-stream modes trigger an unstable boundary layer mode remains unclear thus far. Probably, an infinitesimal amount of energy is sufficient for an unstable frequency to grow and become a TS wave. Locally the most unstable mode grows.

- From both ZPG and APG simulations, H or K type Λ vortex pattern is not obtained. Perhaps, in APG, idealized H, K or C type transition is not obtainable without external forcing.

- A new 'inner' instability, the *helical mode*, is visualized. This is instigated at the overlap of the tail-end of a slow Klebanoff streak and the head-end of a fast Klebanoff streak. The 'overlap' characteristic and the critical layer of these modes is similar to 'inner' modes. The genesis may be attributed to the tilting of the streamwise vorticity component. These are only obtained at moderate free-stream turbulence intensities ($Tu \sim 1\%$) and in presence of a weak instability wave. The trigger seems to be the interaction.

- The intermediate transition route between orderly and bypass routes have been identified: the helical instabilities. The helical structures could possibly due to resonant interaction of secondary and primary perturbations as no direct relation could be identified between helical, TS and Klebanoff streak frequencies and wavelengths. These modes are much shorter and rapidly breakdown to trigger transition.

- A database for future studies such as secondary biglobal stability analysis has been created. Database could also be used for mixed mode transition modelling in boundary layer flows under moderate free-stream turbulence forcing.

CHAPTER 2. NUMERICAL METHOD & INFLOW GENERATION

2.1 Introduction

This chapter is regarding the numerical technique used to solve the governing equations with appropriate boundary conditions. The governing equations have been stated in the next section. Section followed by that gives brief overview of the numerical method and boundary conditions. Of all the boundaries of the computational domain, the inflow boundary is the most critical. At the inflow boundary, disturbances are superimposed on the Blasius profile. Both free-stream turbulence (FST) and TS wave eigenfunction are prescribed as disturbance components that oscillate in time. So a separate section is dedicated for the inflow disturbance generation method. The grid refinement simulations have been described following the section regarding inflow generation. Finally, the code performance in parallel computing environment with message passing interface (MPI) has been provided in brief.

2.2 Governing equations

Incompressible Navier Stokes equations in primitive variables along with the continuity equations are solved. The nondimensionalized governing equations in tensorial notations are as follows

$$\frac{\partial u_i}{\partial t} + \frac{\partial u_i u_j}{\partial x_j} = -\frac{\partial p}{\partial x_i} + \frac{1}{Re}\frac{\partial^2 u_i}{\partial x_j \partial x_j} \tag{2.1}$$

$$\frac{\partial u_i}{\partial x_i} = 0 \tag{2.2}$$

Here, length scales in all directions are nondimensionalized by the inlet boundary layer thickness ($x_i = \frac{x_i^*}{\delta_0}$). Velocity components are nondimensionalized by the free-stream speed

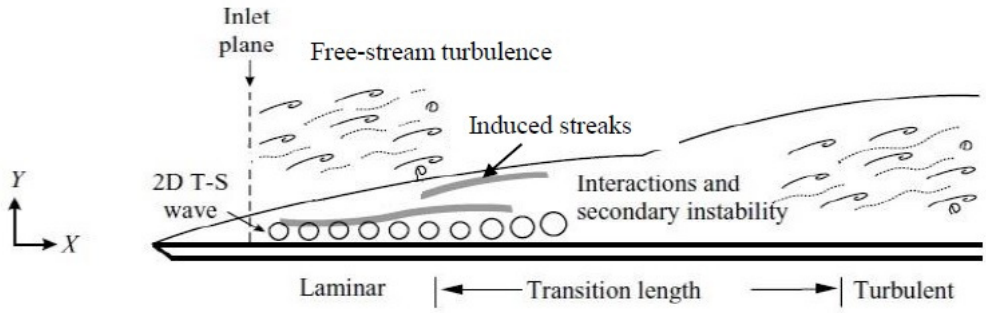

Figure 2.1: Schematic of mixed mode transition to turbulence scenario simulated in this work.

U_∞. Therefore, the dimensional time is scaled by $\frac{\delta_0}{U_\infty}$ and pressure by ρU_∞^2. Consequently, the Reynolds number is $Re = \frac{U_\infty \delta_0}{\nu}$. The total velocity components in streamwise, wall normal and spanwise directions have been denoted by U, V and W throughout the thesis. The perturbation components in these directions are denoted by u', v' and w'.

Figure 2.1 shows the physical flow simulated numerically. The inflow plane is downstream of the leading edge. The inflow plane is typically in the supercritical regime for a mixed mode transition simulation. The TS waves grow and interact with the Klebanoff streaks to trigger transition. The present simulations replicate the experimental setup used by Boiko et al. (1994). They excited the TS wave by wall forcing. Here, the TS wave eigenfunction is prescribed at inlet. So in this representative flow configuration, the inflow plane is downstream of the location of exciter placed on wall.

2.3 Numerical method

The numerical algorithm is based on a finite volume method formulated by Rosenfeld et al. (1991). This formulation allows for computations in a curvilinear grid. This property was useful for simulations of the APG cases herein. The finite volume formulation is in staggered

grid with pressure located at the cell center and the velocity components located at the faces of the computational cell. For a curvilinear grid these components might not be orthogonal to the cell faces. The component of the flux vector (obtained by contravariant transformation of the velocity vector at each face) at corresponding cell face on the other hand is orthogonal to the cell face. In the finite volume discretization, the flux components are the dependent variables. The covariant velocity components are derived from the computed flux after each time step.

Governing equations are spatially discretized by second order central difference finite volume formulation. Velocity gradient in each direction is obtaining by calculating the net flux in that direction divided by the volume of the cell.

2.3.1 Time advancement & pressure correction

The solution algorithm uses fractional time-stepping. For the nonlinear convection terms, time advancement is by explicit second order Adams Bashforth scheme. The discretization of the nonlinear convection terms uses a mixture of central difference and QUICK scheme to avoid numerical oscillations. One-fourth of the derivative was from QUICK contribution, which was found to be sufficient to compute a smooth base flow for both ZPG and APG cases. The diffusion terms are split into implicit diffusion terms or explicit diffusion terms. Terms, such as $\partial^2 u^\xi/\partial\xi^2 + \partial^2 u^\xi/\partial\eta^2 + \partial^2 u^\xi/\partial z^2$ are treated implicitly to implement fractional time-stepping and the rest of the terms are treated by second order accurate explicit Adams Bashforth scheme. Here, u^ξ is the contravariant flux component in the ξ direction normal to a cell face. The implicit diffusion terms are advanced by Crank-Nicolson scheme. The velocity field is obtained at an intermediate time step excluding the pressure terms and by exploiting the the implicitness of diffusion terms.

The pressure correction is obtained by an implicit Euler scheme that utilizes the continuity equation. This step ensures that a divergence free velocity field is obtained after completion of a full time advancement step by updating the intermediate velocity. Periodicity is assumed in the spanwise direction. This allows for the pressure correction to be first solved in the spectral space in the span. The following equations elaborate the computation of the pressure correction. The elliptic equation becomes an algebraic set of equations corresponding to each

spanwise wavenumber k_z.

$$\Big(\frac{\partial^2}{\partial x^2} + \frac{\partial^2}{\partial y^2} + \frac{\partial^2}{\partial z^2}\Big)p(x,y,z) = r(x,y,z) \tag{2.3}$$

$$\Big\{\frac{\partial^2}{\partial x^2} + \frac{\partial^2}{\partial y^2} - k_z^2\Big\}\hat{p}(x,y,k_z) = \hat{r}(x,y,k_z) \tag{2.4}$$

Here, $\hat{p}(x,y,k_z)$ are the Fourier coefficients. The variable in the right hand side in equation 2.3 is $r(x,y,z) = \frac{D\vec{V}}{Dt}$ is the divergence free condition due to continuity constraint imposed on intermediate velocity vector. The physical spanwise wavenumber gets modified due to computation in the discrete domain. Hence,

$$\Big\{\frac{\partial^2}{\partial x^2} + \frac{\partial^2}{\partial y^2} - \frac{2}{\Delta z^2}(1 - \cos k_z \Delta z)\Big\}\hat{p}(x,y,k_z) = \hat{r}(x,y,k_z) \tag{2.5}$$

where, Δz is the spanwise grid spacing. Due to this method, domain decomposition is only in the $x-y$ plane. The computed coefficients are then transposed in to the $x-y$ plane so that each processor has the coefficients at all the grid points in the $x-y$ plane for a given wavenumber. This is why the number of grid points in the spanwise direction must be larger than total number of processors used for the computation.

Fourier coefficient corresponding to each spanwise wavenumber is solved in $x-y$ plane using multi-grid technique. Five grid levels have been used. Three V cycle iterations were performed. After the iterations, the data for the pressure coefficients are transposed back. After inverse Fourier transformation of the coefficients, the pressure correction is obtained. The number of cycles is chosen instead of fixing the desired minimum residue. This is sufficient to obtain satisfactory convergence. The correction step is complete after updation of the flux components.

2.3.2 Boundary conditions

At the inlet boundary, Blasius boundary layer profile is defined as inflow. For excitation cases, the disturbances computed are appended to the Blasius profile. Brief discussion about the disturbance generation is given in the next section.

In the free-stream, the boundary condition is different for ZPG and APG cases. For the ZPG case, free-stream conditions for the Blasius boundary layer is used. Therefore, $U(y_{max}) = U_\infty$ and $W = 0$. Jacobs and Durbin (2000) specified the wall normal velocity at the top boundary as the wall normal velocity obtained from Blasius similarity solution at infinite wall normal distance. Then $V(y_{max}) = U_\infty \frac{d\delta^*}{dx}$. This boundary condition was found to be efficient in its implementation as well as accurate in laminar region. Same condition has been applied herein. For the APG simulations, free-slip and impermeability conditions are applied at the top boundary. This can be implemented in the contravariant flux components by setting $\frac{\partial u^\xi}{\partial \eta} = 0$ and $u^\eta = u^z = 0$.

The boundary conditions applied at wall is straight forward for a boundary layer flow over smooth flat surfaces for governing equations in primitive variables. No-slip boundary condition is used for all the velocity components.

To smoothly convect the turbulence out of the domain, convective outflow boundary condition is appropriate. This condition has been used at the outflow boundary for the present simulations.

$$\Big(\frac{\partial}{\partial t} + U_c \frac{\partial}{\partial x}\Big) u_i = 0 \tag{2.6}$$

In equation 2.6, $U_c = U_\infty$ was used for the ZPG simulations. For APG simulations, as U_∞ is a function of the downstream distance x, $U_c = U_{max}(x_{max})$ has been used. Here, $U_{max}(x_{max})$ is the maximum instantaneous streamwise velocity at the outflow boundary located at $x = x_{max}$.

In transitional flow computations, an explicit sponge region is regularly used at the outflow boundary to avoid upstream 'reflection' effects due to turbulent structures that are convected out of the domain. Jacobs and Durbin (2000) noted that an additive sponge region was not necessary for the present numerical technique for the bypass transition simulations. We also did not use a sponge region as there was no indication of upstream contamination affecting the computations.

2.4 Inflow generation

The free-stream and TS wave disturbances are appended to the Blasius similarity solution at the inflow of the computational domain. Both the components of the disturbances are obtained from solution of the disturbance equations linearized with respect to the mean flow with normal mode assumption, the Orr-Sommerfeld (OS)-Squire coupled equations. Detailed description about the FST generation has been given by Jacobs and Durbin (2000). Same methodology has been adopted in present simulations for FST generation.

2.4.1 OS discrete mode

The TS wave disturbance used for the DNS is the scaled eigenfunction obtained by solving the OS equation. The OS equation, obtained by applying normal mode assumption to linearized disturbance equations is as follows.

$$i(k_x U - \omega)(k_x^2\phi - \phi'') + ik_x U''\phi = -\frac{1}{\tilde{Re}}(\phi^{iv} - 2k_x^2\phi'' + k_x^4\phi) \tag{2.7}$$

Here, k_x is the streamwise wavenumber, ω is the circular frequency of the disturbances. The boundary conditions are that the disturbances are zero at the wall and decay to zero at free-stream. To solve for spatially unstable modes, k_x is complex and ω is real. This equation has been solved using Compound Matrix Method (CMM). The solution procedure to circumvent the issues related to steepness of the OS equation has been discussed extensively in literature and not repeated herein. For reference, one can look up the book by Drazin and Reid (1981).

The TS mode disturbance used for the ZPG simulations has been shown in figure 2.2. At this Reynolds number, this is the least stable linear disturbance. The nondimensional frequency of the TS wave disturbance is $F = \frac{\omega\nu}{U_\infty^2}10^6 = 124$ and its spatial wavenumber $k_x\delta_{99} = 0.6808 - 0.004i$. Clearly, as the imaginary part of the complex wavenumber is negative, the mode is spatially unstable at the inlet Reynolds number $Re_b = \sqrt{U_\infty x_0/\nu} = 400$.

In figure 2.3, the growth rate of the TS wave from DNS has been plotted at a chosen wall normal height for both streamwise (u') and wall normal (v') perturbation velocity components and compared with the growth rate predicted by LST at the inlet Reynolds number. The

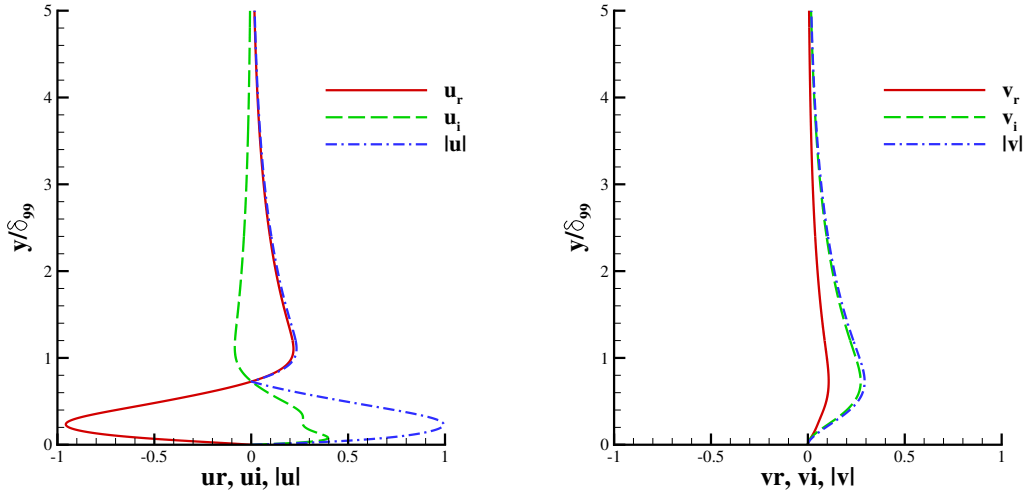

Figure 2.2: Mode shape of the OS discrete eigen function at $Re_b = 400$ and $F = 124$ used for mixed mode transition cases in ZPG.

TS wave amplitude was $1\%U_\infty$ defined as the maximum perturbation velocity at the inlet with respect to the free-stream velocity. The growth rate shows very good match initially and deviates from LST predictions only after $x = 50$. This is to be expected, as to capture the actual growth rate of the instability using linear theory, the Parabolic Stability equations have to be solved.

2.4.2 OS-Squire continuous modes

The continuous modes of the Orr-Sommerfeld equation are obtained by assuming a boundedness condition for disturbances in the free-stream (Grosch and Salwen, 1978). That is the only difference in formulation between the discrete and continuous mode disturbances. The free-stream boundary condition is assumed to be oscillatory. So for the solution of the form,

$$\phi_c = Ae^{-Q^{1/2}y} + Be^{Q^{1/2}y} + Ce^{-k_x y} \tag{2.8}$$

boundedness is satisfied if Q is real and negative. $Q = -k_y^2$ may be assumed, where, k_y is the wall normal wavenumber of the disturbance. Jacobs and Durbin (1998) noted, that

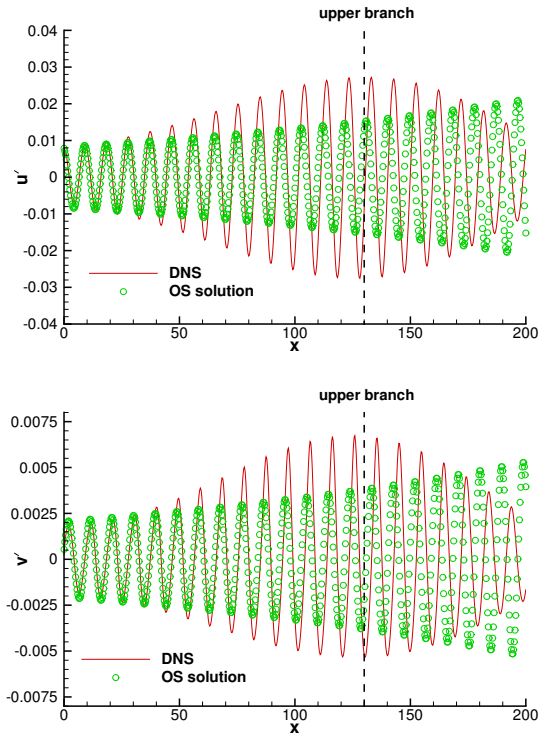

Figure 2.3: Comparison of growth of u' and v' perturbations as predicted by linear stability theory and DNS.

the solution at the free-stream carries phase information. Using the phase information, they formulated a boundary condition that was implemented including two boundary points that eliminated the spurious oscillations at lower boundary for higher frequency disturbances. The same methodology has been used for solution of the OS continuous modes herein.

The real and imaginary components of the OS continuous modes have been plotted for two frequencies in figure 2.4 at the inlet Reynolds number ($Re_b = 400$) for the computational domain. Solutions are for $\omega = 0.1$ and 0.01. The solutions oscillate in the free-stream and quickly decay as it moves closer to the wall. The horizontal dashed line indicates the 99% boundary layer thickness. Comparison of the solutions reveal that the lower frequency component penetrates deeper inside the boundary layer. Jacobs and Durbin (1998) showed that shear sheltering prevents the high frequency components from penetrating the boundary layer. Disturbances with same frequency and wavenumber penetrate deeper at lower Reynolds numbers. Another

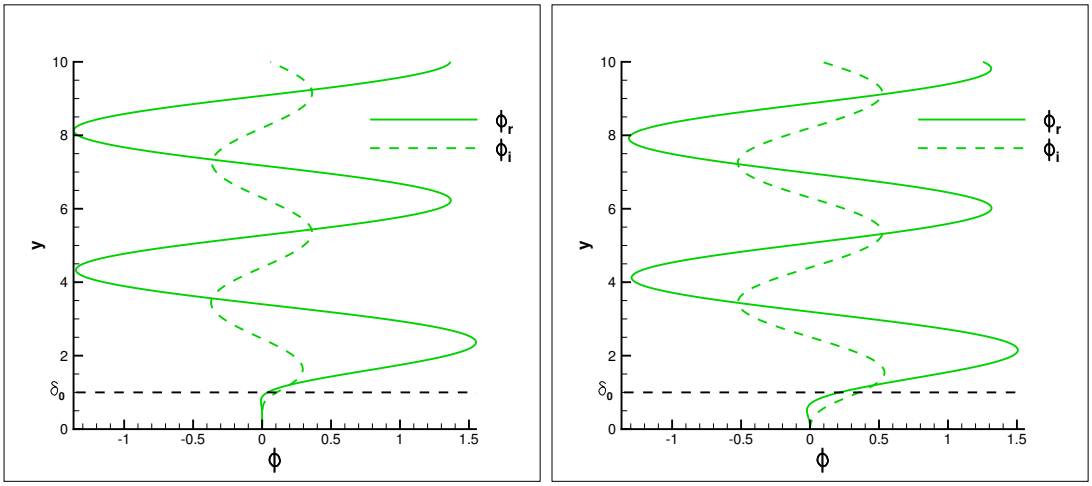

Figure 2.4: Left: Mode shape of the OS continuous mode eigen function for $Re_b = 400$, $F = 177$ and $k_y = 1.654$. Right: Mode shape of the OS continuous mode eigen function for $F = 17.7$ at the same Re_b and k_y. The horizontal dashed line indicates the 99% boundary layer thickness.

parametric property of the continuous mode is the deeper penetration of the mode for higher k_y (Zaki and Durbin, 2005). But for higher k_y, dissipation is also enhanced, so that the mode decays quicker.

Orr-Sommerfeld equation gives disturbances that provide horizontal vorticity field. For a 3D disturbance, the wall normal vorticity equation, the Squire equation is also required to be solved.

$$(U - c)\chi - \frac{1}{i\alpha Re}\{\chi'' - (\alpha^2 + \beta^2)\chi\} = -\frac{\beta}{\alpha}\frac{dU}{dy}v \tag{2.9}$$

In this equation, the wall normal disturbance v in the right hand side is from the solution of OS continuous mode, which acts as a source of wall normal vorticity. The spanwise vorticity due to base flow is tilted upward by the v component. Consequence is the generation of wall normal vorticity. The boundary conditions are similar to OS continuous modes.

In figure 2.5, Squire mode eigenfunctions have been plotted at the inlet Reynolds number of the computational domain. 99% boundary layer thickness at inlet denoted by δ_0 is also shown in these plots. The difference between plots in figure 2.5 is the disturbance frequency. The Squire mode also oscillates in the free-stream and decays rapidly inside boundary layer. The

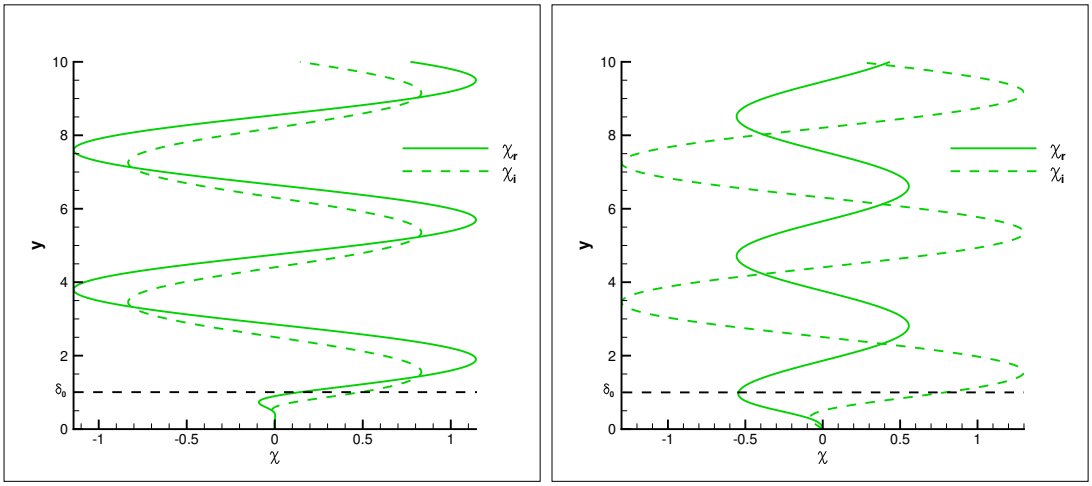

Figure 2.5: Left: Mode shape of the Squire continuous mode eigen function for $Re_b = 400$, $F = 177$, $k_y = 1.654$ and $k_z = 1.654$. Right: Mode shape of the Squire continuous mode eigen function for $F = 17.7$ at the same Re_b, k_y and k_z. The horizontal dashed line indicates the 99% boundary layer thickness.

decay is quicker for the higher frequency ($\omega = 0.1$) disturbance.

Evidently, the continuous modes have special characteristics. These oscillate in the free-stream and decays inside boundary layer. Moreover, the low frequency disturbances penetrate further inside the boundary layer. The Klebanoff streaks are also low frequency streamwise disturbances inside the boundary layer. Thus continuous mode disturbances can induce Klebanoff streak-like signature inside the boundary layer. Jacobs and Durbin (2001) noted that these properties made the continuous modes ideal for modeling FST downstream of the leading edge.

2.4.3 Inflow free-stream turbulence

The solutions of the OS-Squire disturbances represent a complete basis for an arbitrary disturbance (Salwen and Grosch, 1981). Here, the free-stream disturbances have been expanded in terms of the continuous mode eigenfunctions. The disturbance eigenfunctions are computed with parallel flow approximation. These are only prescribed at the inlet. The numerical solution downstream of the inlet takes care of the evolution of these disturbances inside

the computational domain. The disturbances induce broadband Klebanoff streaks inside the boundary layer. Jacobs and Durbin (2001) only used OS continuous modes. Both OS and Squire eigenfunctions have been used in the present work (Hack and Zaki, 2014).

Multiple modes of the continuous spectrum have been used to construct broadband FST. 32 modes each for frequency, wall-normal and spanwise wavenumbers have been used. The coefficients of the basis eigenfunctions are desired to be isotropic at free-stream and must satisfy continuity. Jacobs and Durbin (2001) prescribe those as follows,

$$\hat{u} = -\zeta \frac{ik_y}{|k|} \cos\gamma + \xi \sin\gamma \tag{2.10}$$

$$\hat{v} = -\zeta \frac{\sqrt{k_x^2 + k_z^2}}{|k|} \tag{2.11}$$

$$\hat{w} = -\zeta \frac{ik_y}{|k|} \sin\gamma - \xi \cos\gamma \tag{2.12}$$

where, ζ and ξ correspond to OS continuous and Squire modes for each $\vec{k}$. $\tan\gamma = k_x/k_z$ gives the tilt of the horizontal vortex system due to OS continuous modes.

Expressions for ζ and ξ provide the desired randomness to the FST, which are, $\zeta = f_k e^{i\theta_1} \cos\tau$ and $\xi = f_k e^{i\theta_2} \sin\tau$. Here θ_1, θ_2 and τ are uniformly distributed random phases. f_k a scalar that is derived from the desired energy spectrum. The kinetic energy ($K.E.$) of the fluctuations are obtained from amplitudes of the Fourier coefficients using following expression.

$$K.E. = \frac{1}{2} \sum_{\vec{k}} \hat{u}_i \hat{u}_i{}^* = \frac{1}{2} \sum_{\vec{k}} (\zeta\zeta^* + \xi\xi^*) = \frac{f_k^2}{2} \tag{2.13}$$

This discrete expression of the disturbance energy is related to a desired energy spectrum. The von Karman energy spectrum has been used for the present work. Figure 2.6 shows the obtained spectra corresponding to the amplitude of the basis modes. The slope of the spectra is proportional to $k^{-5/3}$ and k^4 at high and low wavenumbers, respectively.

$$K.E = \sum_{\vec{k}} \frac{E(k)}{4\pi k^2} \left(\frac{2\pi}{L}\right)^3 \tag{2.14}$$

Further detail about the construction of the inlet disturbance spectra is provided in Jacobs and Durbin (2001).

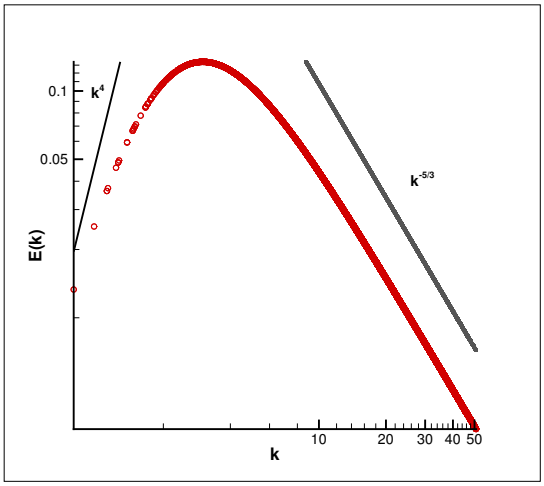

Figure 2.6: $E(k)$ plotted against k corresponding to Fourier coefficients used for inflow free-stream turbulence generation.

2.5 Grid refinement

It is essential to accurately capture the Klebanoff streaks, TS waves and turbulent spots in the laminar and transitional regime. It has been suggested in literature that the mesh resolution requirements are not as stringent for bypass transition as it is for natural transition (Voke and Yang, 1995). But it is important to note that the Klebanoff streaks do not have clear development phases when compared to natural transition through TS waves. The breakdown is local and spot inception, irregular. Often the streaks breakdown to spots when the adjacent fluid remains calm. Hence, to study the flow physics of the transition process, fine grid resolution is necessary in laminar and transitional region to accurately compute the dynamics. But also important is to consider a large enough domain so that the periodicity boundary condition does not affect the flow evolution. This is a constraint. Large domain considerably increases the computational cost but it is nonetheless necessary.

In the left frame of figure 2.7, the location of wall normal grid points has been shown for the ZPG simulations. The grid is stretched in the wall normal direction using hyperbolic tangent function. The ordinate has been scaled by the inlet boundary layer thickness. Almost 30 grid points resolve Blasius profile at inlet. The stretching ratio of the wall normal grid points has

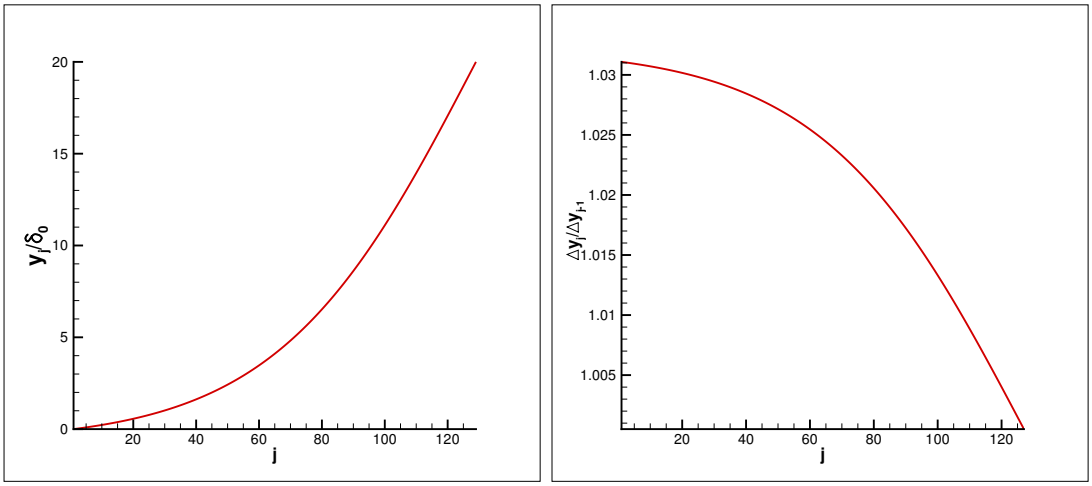

Figure 2.7: Left: Location of wall normal grid points in ZPG. Right: Stretching ratio of wall normal grid used for simulations of both ZPG and APG.

been also shown in the right frame of figure 2.7. In APG simulations, the stretching ratio is kept constant downstream of inlet, even though the top boundary diverges outward to incorporate adversity in pressure gradient. The stretching ratio remains within 3% throughout the domain.

The grid refinement study was based on the mixed mode transition case in ZPG with FST of intensity $Tu = 1\%$ and TS wave amplitude $A = 1\%$ at inlet. The domain size and base grid was motivated by the direct simulations of mixed mode transition in ZPG performed by Liu et al. (2008a). The inlet Reynolds number in present simulations is same as theirs, as we selected the same TS wave for mode interaction simulations for ease of comparison. The domain size was $320\delta_0 \times 20\delta_0 \times 16\delta_0$. Simulations were also performed in smaller spanwise domain with width $8\delta_0$. The result was found to remain unchanged. The base grid was $1024 \times 128 \times 64$. The grid was systematically refined in all three directions. In the initial grid refinement simulations, the Quick contribution towards calculating the nonlinear convection terms was switched off. Therefore, those simulations were prone to numerical noise in free-stream. In figure 2.8, the time and span averaged skin-friction coefficient (C_f) has been plotted against the Reynolds number with respect to distance from leading edge, $Re_x = U_\infty(x_0 + x)/\nu$. The laminar (for Blasius profile) and turbulent skin-friction (from correlation) coefficients have been also plotted. Significant overshoot in C_f after completion of transition is noted for all cases. Similar levels

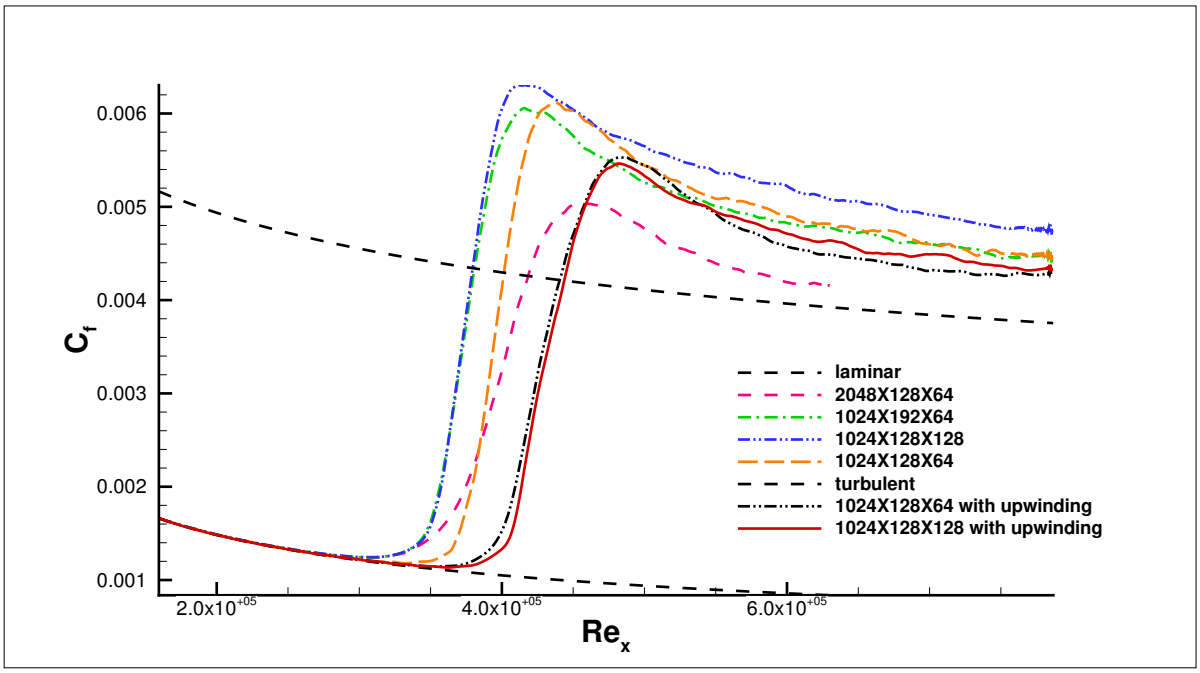

Figure 2.8: Time and span averaged C_f for mixed mode transition case in ZPG with free-stream turbulence intensity $Tu = 1\%$ and TS amplitude $A = 1\%$ at inlet for various grid resolutions.

of overshoot were noted in highly resolved forced orderly transition simulations by Sayadi et al. (2013). The overshoot is minimum when 2048 grid points were used in the streamwise direction (this simulation was performed with a streamwise domain size of $240\delta_0$ with 1536 grid points in that direction, so that streamwise resolution was doubled). Grid refinement in all directions gave different results.

When an admixture of Quick scheme and central difference was used, the numerical oscillations in the free-stream were eliminated. The simulations with 64 and 128 grid points in the spanwise direction indicate that further grid refinement in the spanwise direction would be unnecessary. Transition was triggered (indicated by minimum C_f) and accomplished (location of maximum C_f) later when the numerical oscillations were absent. $\Delta x+$ and $\Delta z+$ have been plotted as a function of Re_x in the left frame of figure 2.9. $\Delta y+$ corresponding to the first grid point above the wall has been plotted versus Re_x in the right frame of figure 2.9 for the case simulated with the final grid with $1024 \times 128 \times 128$ grid points. This is for the simulation with

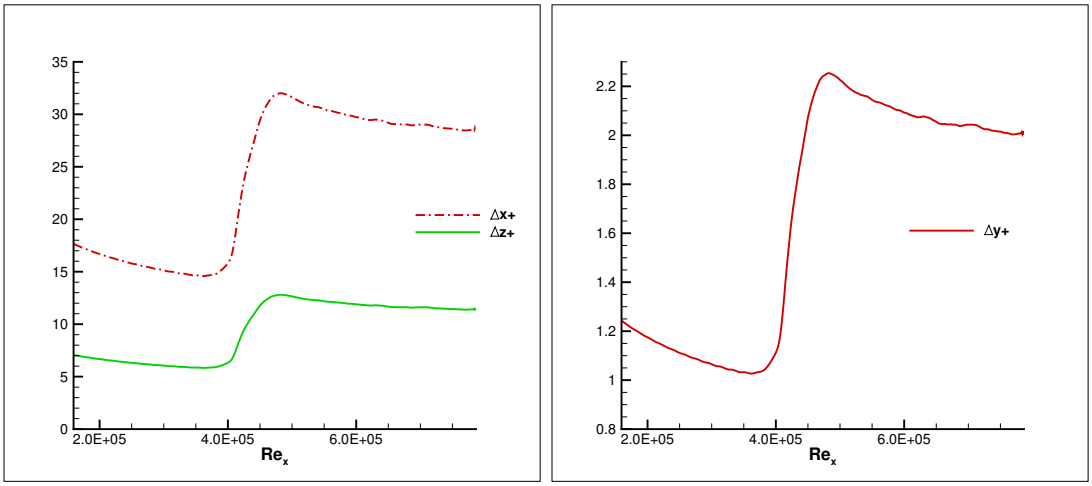

Figure 2.9: Left: $\Delta x+$ and $\Delta z+$ plotted against Re_x for the final grid ($1024 \times 128 \times 128$) used for simulations in ZPG. This is for the same case as in figure 2.8. Right: $\Delta y+$ plotted against Re_x for the same case.

the Quick scheme. The maximum value of $\Delta x+ \sim 32$, $\Delta z+ \sim 13$ and $\Delta y+ \sim 2.3$ at the station where C_f is maximum.

Jacobs and Durbin (2001) noted, that for the bypass transition simulations, one requires to resolve the Klebanoff streaks in the transitional flow regime. The Klebanoff streaks are very long in the streamwise direction but quite narrow in the spanwise direction. Their spanwise width is $\Delta z+ \sim 30$. The final grid resolves 3 Klebanoff streaks at the location of maximum C_f. Bypass transition simulations with FST intensity $Tu = 3.5\%$ were performed to examine the spanwise grid resolution. In the left frame of figure 2.10, skin friction coefficient C_f averaged in time and in the homogeneous spanwise direction has been plotted for the final grid with $1024 \times 128 \times 128$ grid points. For comparison another simulation was performed keeping all other parameters constant except the number of grid points in the span. The resolution in the spanwise direction had been doubled ($nz = 256$). C_f for that simulation has been also shown in the same plot. Both simulations approximately follow the same curve. $\Delta z+$ has been plotted for both of these simulations in the right frame of figure 2.10. For the finer spanwise resolution case the maximum $\Delta z+ \sim 6$ which is same as Jacobs and Durbin (2001). Yet, figure 2.10 demonstrates the sufficiency of spanwise grid resolution of the final grid with 128 grid points

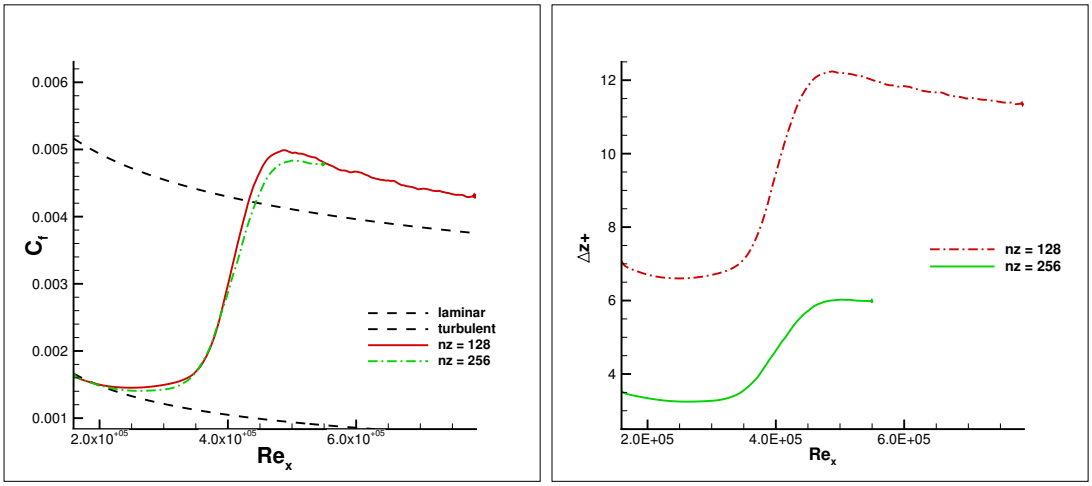

Figure 2.10: Left: Time and span averaged C_f for the bypass transition case in ZPG with free-stream turbulence intensity $Tu = 3.5\%$ at inlet for different spanwise resolutions. Right: $\Delta z+$ plotted against Re_x for the bypass case with different spanwise resolutions.

in that direction.

The overshoot in the C_f plot at the location of maximum C_f is partly due to low resolution in the streamwise direction. But as noted earlier, similar overshoot is observed in very highly resolved simulations by Sayadi et al. (2013). Clearly, $\Delta x+$ and $\Delta z+$ are marginal in the post-transition turbulent region. The overshoot in that region is due to lack of grid resolution. That region is not the focus of the present study, which is addressed to the process of transition.

2.6 Code performance

Most of the computations reported here were performed in the Stampede Supercomputer of the Texas Advanced Computing Center (TACC) located at University of Texas at Austin. Also most of the simulations were run with 64 processors. The domain is decomposed in the streamwise and wall normal directions. So each processor solves for all the grid points in the span for a given subdomain in the $x-y$ plane except for the pressure. The multigrid technique is also implemented in the $x-y$ plane for each spanwise wavenumber. A transpose operation is performed prior to this step so that each processor has complete data for a specific spanwise wavenumber. After the multigrid iterations, inverse transpose operation is performed. Finally

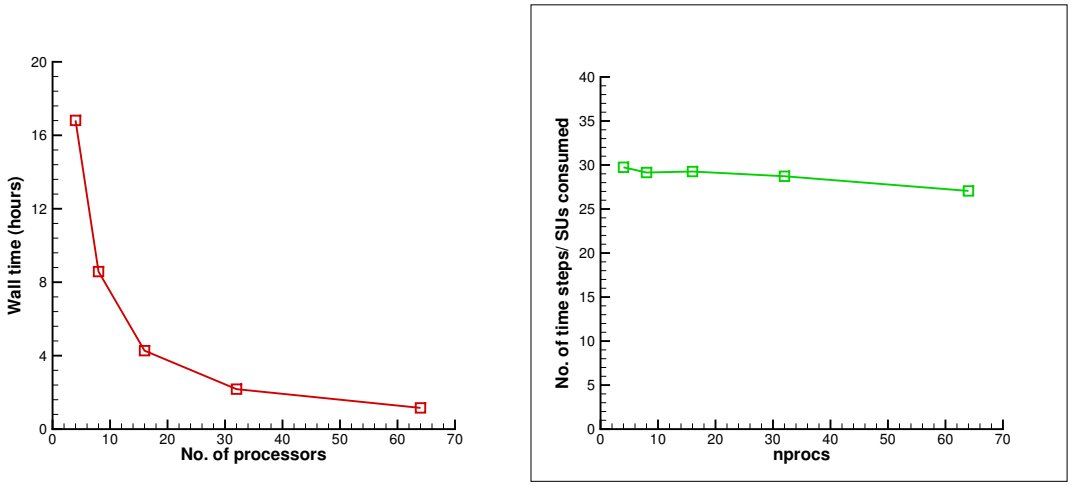

Figure 2.11: Left: Time taken to solve a selected problem of given size and initial condition for varying number of processors. Right: Number of time steps solved per SUs consumed on Stampede when number of processors used is varied.

the intermediate velocity is updated using pressure correction to obtain the velocity field in the new time step. The mode of communication is the message passing interface (MPI) library.

In the left frame of figure 2.11, the number of hours taken to solve a predefined problem is plotted when the code is run with different job sizes. Domain decomposition was altered only in the streamwise direction. The problem was for the bypass transition simulation with $Tu = 3.5\%$ at inlet. All conditions were the same for each run except the number of processors being used. The initial and boundary conditions and the simulation time at which the simulations were started for each run remained same. The problem was run for a fixed number of time steps. The wall time in hours have been plotted versus the number of processors used for each run. If the number of processors used is doubled, for a perfectly scalable code, one would expect a curve similar to Wall time $\times$ No. of processors = constant. The obtained curve is very similar to such a hyperbolic profile. The number of time steps computed for each SU consumed for each of these runs have been plotted versus number of processors used in the right frame of figure 2.11. 1 processor running for an hour is denoted as 1 Service Unit (SU) on XSEDE resources. This plot shows that the number of time steps solved for each SU consumed does not appreciably change as the number of processors used for the same problem is increased.

This indicates that the time consumed for inter processor communication does not appreciably affect the code performance as increasing number of processors are used to solve the problem.

CHAPTER 3. TRANSITION TO TURBULENCE BY INTERACTION OF FREE-STREAM AND DISCRETE MODE PERTURBATIONS

Modified from a paper published in Physics of Fluids: Bose and Durbin (2016b)

Abstract

Mixed mode transition is studied by direct numerical simulation. Low frequency streaks are induced within the boundary layer by free-stream turbulence and an Orr-Sommerfeld discrete mode eigenfunction is introduced at the inlet. Amplitudes are selected such that the interaction of these modes can cause transition. Aside from the highest amplitude of free-stream turbulence, neither disturbance alone is sufficient to cause transition within the flow domain.

Results are classified into three routes to transition, depending upon the 2D Tollmien-Schlichting mode strength and free-stream turbulence intensity.

1) At low turbulence intensities, formation and breakdown of Λ vortices instigates transition. A strong TS mode at low turbulence intensities undergoes secondary instability which is neither H or K type. The pattern and spanwise size of Λ vortices depend upon frequency and spanwise width of Klebanoff streaks upon which they are generated.

2) When the TS mode amplitude is low, transition is via streak instability. The streaks are induced by the free-stream turbulence, but this case differs from conventional bypass transition in the mechanism of inception of turbulent spots. Three dimensional visualizations of the perturbation flow field show growing, helical undulations similar to $n = 1$ instability modes observed in axisymmetric jets and wakes.

3) At high turbulence intensities, the flow undergoes bypass transition. The TS wave has a small effect, but its influence is seen at the larger of the two amplitudes studied.

3.1 Introduction

Transition in attached subsonic boundary layers is usually described as following either a *bypass* or an *orderly* route. The former occurs under free-stream turbulence or in other substantially perturbed environments; the latter originates as instability waves in a quiet environment. However, there is evidence that in some circumstances these two routes may be present simultaneously and interact. That regime can be called *mixed mode* transition.

Orderly transition starts from instability waves, proceeds through secondary instabilities, then breaks down locally, into turbulent patches. On smooth, flat or convex surfaces, without cross-flow, the primary instability is a discrete Tollmien-Schlichting (TS) wave. The vorticity in a 2-D TS wave lies perpendicular to the flow direction. Secondary instability was analyzed by Herbert (1988) as resonant instability of a finite-amplitude TS-wave ansatz. The secondary instability is waviness along the axis of the primary vortex; it develops into an array of Λ vortices, which lift from the wall. The vortex pattern is described as K, H or C type, depending on its arrangement (White, 1991). The apex of the vortex lifts away from the wall and break down to turbulence is seen around its tip.

Bypass transition is caused by free-stream turbulence. It starts from non-modal perturbations, named 'Klebanoff modes', and also known as 'streaks'. These are positive and negative jet-like perturbations to the mean flow. The perturbations are very elongated in the streamwise direction, and the u' component of velocity is dominant. Rapid distortion theory (Phillips, 1969; Landahl, 1980; Durbin and Wu, 2007) provides a simple explanation of how streamwise elongated jets amplify in a shear flow: components with $k_1 \sim 0$ persistently extract energy from the mean shear while shorter wavelengths are limited by pressure gradient. As they intensify, the jets lift from the wall and break down locally, into turbulent patches. The breakdown appears to start as an inflectional instability triggered by small scale perturbations from the free-stream.

The present work is on the interaction between orderly and bypass mechanisms. Interaction between free-stream turbulence and TS waves has been investigated in Fasel (2002) and Liu et al. (2008a). The latter specifically investigated the interaction between orderly and bypass

mechanisms, but the free-stream disturbance was *monochromatic*, and there is some question of whether the particular response is representative of broadband disturbances. The present paper addresses the case of *broadband* free-stream turbulence. When the TS amplitude is large enough, it confirms some previous ideas, but shows how they depend on the free-stream perturbation. Some new behaviors are uncovered herein, especially the discovery of helical mode breakdown when the TS amplitude is lower.

In broad terms, three regimes are seen in the present work. In the first, TS waves are distorted by Klebanoff mode jets. With the broadband spectrum, the jets are localized and they set the size of Λ vortices that form. Sometimes a series of Λ's is seen on a single jet, but the spatial patterns associated with K or H type instability (seen in orderly transition) do not occur. This is not surprising, as the distortions are forced by interactions, rather than being caused by resonant instability. The size of the vortices is similar to K and H-type, so there may be some sense in which they are in the right size range to extract energy from the flow.

A new behavior is seen at lower TS amplitudes. This is the second regime. Transition occurs downstream of the upper branch, where the TS waves are decaying. Nevertheless, they trigger a transition well upstream of where it would occur in their absence. Transition occurs on the streaks; the TS wave is in the background. Isolated Klebanoff mode jets lift up from the wall, where breakdown occurs via helical instabilities. The helices move with about one-half of the free-stream speed. *Helical breakdown* has not previously been recognized.

The third regime is bypass transition, with only a small effect of the TS waves. This occurs when the free-stream turbulent intensity is over 2%.

3.2 DNS domain and inlet disturbance

The domain is rectangular and starts with a Blasius boundary layer and perturbations prescribed at the inlet. The inlet Reynolds number is determined by the growth criteria of the TS wave at a chosen frequency. In the present simulations, the TS mode has a nondimensional frequency $F \equiv 10^6\omega\nu/U_\infty^2 = 124$ and is unstable at $Re_b = 400$, (Liu et al., 2008a) with a complex spatial eigenvalue of $\alpha\delta_{99} = 0.6808 - 0.004i$. Hence, at the inlet a Blasius profile is specified with $Re_b \equiv \sqrt{U_\infty x_0/\nu} = 398$.

The domain length is 320 times the 99% inlet boundary layer thickness (δ_0). It extends to $20\delta_0$ in the wall normal and $16\delta_0$ in the spanwise directions. Sensitivity studies confirmed that the domain width is large enough to not affect the size of the flow structures.

The computational domain starts at a distance x_0 from the leading edge. The streamwise distance downstream of the inlet plane is denoted as x from here onwards. The streamwise domain extends well beyond the upper branch of the neutral stability curve for 2D TS waves, which lies at $Re_b = 650$. $1024 \times 128 \times 128$ grid points were used in the streamwise, wall normal and spanwise directions. The grid parameters were motivated by those selected for similar computations in Jacobs and Durbin (2001). Grid and domain independence was studied in preparation for the simulations. The present grid resolution is sufficient to capture the whole process of instability and consequent transition. For example, in the bypass transition case for $Tu = 3.5\%$ in figure 3.3, that coarsest resolution in + units is $\triangle x^+ \sim 30$, $\triangle y^+ \sim 2.15$ and $\triangle z^+ \sim 12.25$, at the location of maximum skin-friction. 29 wall normal grid points resolve the boundary layer at the inlet.

The three-dimensional incompressible Navier-Stokes equations have been discretized by the finite volume method of Rosenfeld et al. (1991) on a staggered grid. The solution algorithm uses fractional time stepping. The nonlinear convection terms have been discretized by a second order Adam-Bashforth scheme, and linear diffusion terms were discretized by an implicit, Crank-Nicolson scheme. A blend of QUICK and central differences has been used in the convection terms to avoid numerical oscillations; these oscillations were seen only in the free-stream. The maximum coefficient of the QUICK contribution was one-fourth. Periodicity has been assumed in the span. The Poisson solver for the pressure-correction uses a spectral method in that direction and Gauss-Seidel, with multi-grid in the x-y plane.

Two different TS wave amplitudes (A) have been studied, 1% and 0.5%, defined, in percentage, as the maximum of the streamwise and wall normal perturbation velocity at the inlet, divided by the mean free-stream velocity.

Inlet, free-stream turbulence was synthesized from Orr-Sommerfeld and Squire continuous modes, by the method of Jacobs and Durbin (2001), Brandt et al. (2004) and Hack and Zaki (2014). This is a well-established method, and has been validated against experiment. 32

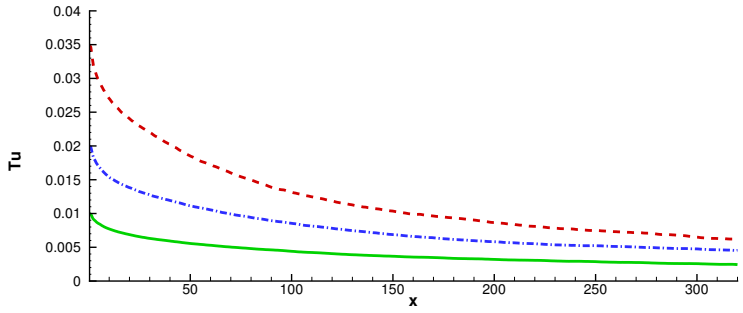

Figure 3.1: Free-stream decay of turbulence intensity for different Tu at inlet.

modes for a set of frequency, wall normal wavenumber, and spanwise wavenumber were used. The Fourier coefficients for the Orr-Sommerfeld and Squire modes are isotropic, satisfy continuity, and are based on a von-Karman spectrum with the peak at wavenumber $k_p \sim 2.6$, nondimensionalized by the streamwise integral scale, L_{11}.

Free-stream turbulence intensities $Tu = \sqrt{(u_{rms}^2 + v_{rms}^2 + w_{rms}^2)/3}$ of 1%, 2% and 3.5% were used. The decay of free-stream perturbations with streamwise distance x from the inlet plane for each of these cases is shown in figure 3.1.

Instantaneous curves of skin-friction coefficient (C_f) are shown in figure 3.2 when either a TS wave or the free-stream turbulence is specified at the inlet. None of the inflow perturbations individually cause the flow to transition. For $Tu = 3.5\%$ (not included in figure 3.2), bypass transition is observed within the present domain. For $Tu = 1\%$ and 2%, though, bypass transition would occur beyond the present domain, so it is not seen in figure 3.2. (We have verified in a separate simulation, starting further downstream, that $Tu = 2\%$ transitions after the end of our domain.)

Only the low frequency components of the free-stream disturbances are able to penetrate the boundary layer, due to shear sheltering (Jacobs and Durbin, 1998). This is reflected in the instantaneous C_f curve for $Tu = 1\%$; it remains below the zero-pressure-gradient (ZPG) Blasius boundary layer curve because the plane selected for this plot is in a low, frequency negative streak. For $Tu = 2\%$, the plane crosses from a negative streak to a positive one and back again to another negative streak.

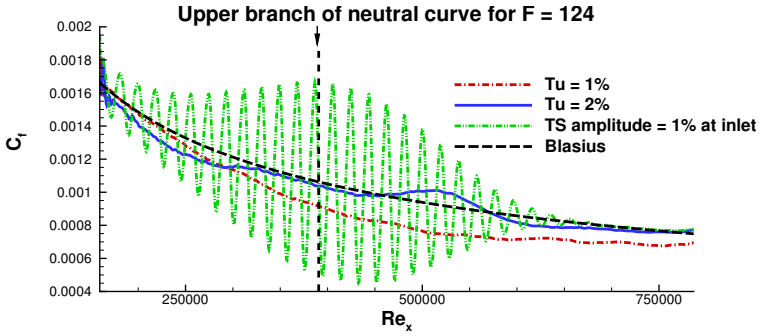

Figure 3.2: Instantaneous, spanwise localized skin-friction coefficients (C_f) as functions of Re_x when either a TS wave or free-stream turbulence is prescribed at the inlet.

For the case with a single TS wave, the curve undulates around the Blasius curve. It shows the exponential growth and decay, associated with crossing the lower and upper branches. The location of the upper branch is indicated in the figure. This solution of the full, incompressible NS equations clearly shows that the evolution of the mode matches very well with the predictions of the linear stability theory.

3.3 Overview of mode interaction

The flow perturbed by a 2-dimensional, discrete TS wave and free-stream turbulence, follows three transition routes, depending on the discrete mode amplitude (parameter A) and the Tu prescribed at inlet. The mean skin friction coefficient (C_f) has been plotted against the Reynolds numbers Re_x in figure 3.3(a) and Re_θ in figure 3.3(b), for all the cases considered. Here, Re_x and Re_θ are based on length scales defined by the streamwise distance from the leading edge ($x_0 + x$) and the local momentum thickness θ. The velocity scale is U_∞ for both. Neither the TS wave, nor low intensity free-stream turbulence, by themselves is able to trigger transition. But figure 3.3 shows that even in the presence of low Tu, the flow undergoes transition for the lower TS amplitude ($A = 0.5\%$): the low amplitude TS mode is evidently sufficient to destabilize the streaky boundary layer underneath low intensity free-stream turbulence.

Reynolds numbers Re_x and Re_θ at the onset of transition to turbulence are tabulated in

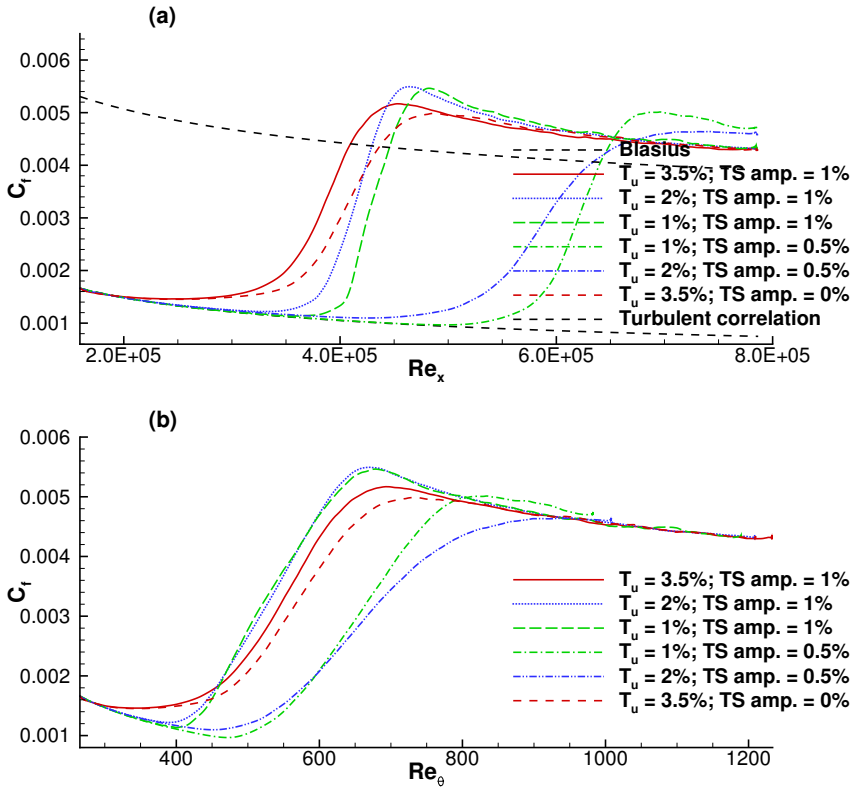

Figure 3.3: Time and span-averaged skin-friction coefficient (C_f): (a) as a function of Re_x; (b) Re_θ.

table 3.1, for all the cases considered in this section. The third and fourth columns show the value of Re_x and Re_θ respectively. These values are the location of minimum C_f, corresponding to cases shown in figure 3.3. These Reynolds numbers, therefore, indicate the streamwise location of the onset of the transition process. For future reference, the conversion between x and Re_x is $Re_x = 1960(81.34 + x)$.

Table 3.1: Reynolds numbers at the onset of transition to turbulence for different perturbation amplitudes at inlet.

Tu ($\%U_\infty$)	A ($\%U_\infty$)	Re_x at minimum C_f	Re_θ at minimum C_f
1	0.5	496,919	471.64
2	0.5	426,480	451.59
1	1	362,148	400.62
2	1	328,479	387.95
3.5	0	250,081	346.85
3.5	1	240,896	337.7

The flow did not transition within the computational domain when $A = 0.2\%$ for either the $Tu = 1\%$, or the 2% case; and, therefore, those cases have not been shown in the figure. For $Tu = 1\%$ and $A = 1\%$, transition takes place very close to the location of bypass transition with $Tu = 3.5\%$ and no TS wave. The fact that the flow transitions for Tu as low as 1% in the presence of a strong TS mode is intriguing — more so because it takes place almost at the same streamwise location as the bypass case of $Tu = 3.5\%$.

Another noticeable feature of these curves is the overshoot in C_f, which also occurs in cases of transition through secondary instability, as per the literature, but is not seen in pure bypass transition. Overshoot does not occur when $Tu = 3.5\%$ for any A, showing that this is a bypass case, whether or not TS waves are present. When plotted versus Re_θ, the overshoot becomes less apparent.

The following subsections separately describe observed mechanisms in the various cases of figure 3.3. They are organized into three types of behavior.

3.3.1 Low to moderate free-stream turbulence intensity & high TS wave amplitude: Λ vortices

When a high amplitude TS wave is injected at the inlet, under low to moderate free-stream turbulence, visualizations suggest a mechanism similar to secondary instability of the TS wave. However, it differs in that it is forced by the Klebanoff streaks. Λ vortices are seen to align with the long, low frequency streaks. In figures 3.4 and 3.5, the free-stream intensities are $Tu = 1$ and 2%; the instability wave has a, relatively high, amplitude of $A = 1\%$ at the inlet. Under each of these, individually, the flow remained laminar within the computational domain. Together they caused transition.

In figure 3.4, instantaneous streamwise (u') and wall normal (v') perturbation velocity contours have been plotted in a horizontal plane at a wall normal height $y = \delta_0/3$. Both plots include the inlet and extend up to $x = 200$, where the flow is already turbulent. The vertical strips of consecutive light and dark contours in the contour plots are due to the crests and troughs of the 2D TS wave. Close to the inlet, the TS waves show very little modulation of v' in the spanwise direction, but u' is significantly modulated. As the flow evolves downstream, long, streamwise Klebanoff streaks become apparent in the u' contour plot. The streaks intensify downstream. As a consequence of superposition, in the plots, the TS wave becomes increasingly fragmented in the span. These fragmented, high shear regions evolve downstream to form Λ-shaped vortices. Λ-shaped vortices are identifiable in figure 3.4 around $x \sim 110$ in both u' and v' contour plots.

The v' contour plot, expectedly, does not show the effect of the streaks, as those are predominantly manifested in the u' component. The v' perturbations, on the other hand, are considerably affected after the the Λ vortices begin to form.

In figure 3.5, vortical structures within the boundary layer prior to transition are visualized by isosurfaces of the Q-criterion (Dubief and Delcayre, 2000) defined by $Q = \frac{1}{2}[|\Omega|^2 - |S|^2] > 0$ where, Ω and S are the rate-of-rotation and rate-of-strain tensors, respectively. The base flow contains weak streaks induced by the free-stream turbulence; they are seen in u-component contours in figure 3.4, but are not visualized by the Q-contours. The Λ vortices and the Ω-

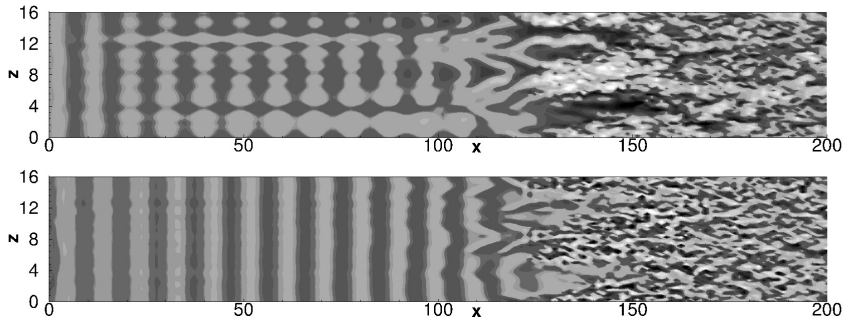

Figure 3.4: Instantaneous u' (top) and v' (bottom) fluctuation velocity contours for $Tu = 1\%$ and $A = 1\%$ in the horizontal $x-z$ plane at $y = \delta_0/3$. Contours are plotted for $-0.3 \leq u' \leq 0.3$ and $-0.1 \leq v' \leq 0.1$.

shaped vortex rings at the tip of the Λ vortices are characteristic of pre-transitional boundary layers at these levels of constituent flow perturbations.

Free-stream turbulence generally leads to bypass transition through the interaction of high frequency components of the free-stream perturbations and streaks forced inside the boundary layer at much lower frequencies (Jacobs and Durbin, 2001). In the present case, on the other hand, the TS wave becomes the seed for natural transition when it is distorted by the streaks. For a high amplitude TS wave under low to moderate levels of free-stream turbulence, the Λ vortices and their breakdown are the dominant transition route.

In figure 3.5(b), the free-stream turbulence level is higher. In addition to the Q isosurfaces, in-plane fluctuation velocity vectors at a height $y = \delta_0/3$ from the wall are included. The velocity vectors show that the Λ vortices are stationed on negative streaks. A sequence of vortices is seen, as the successive periods of the wave are distorted by the long streak. This alignment is a forced response, as opposed to the resonant mechanism of K or H-type secondary instability.

Toward the center of figure 3.5(b), one sees patches of higher velocity, induced by isolated vortices. Although these are in-plane velocity vectors, similar local velocity vectors show that the vortices are rotating upward under their induced velocity. The streamwise streaks also lift,

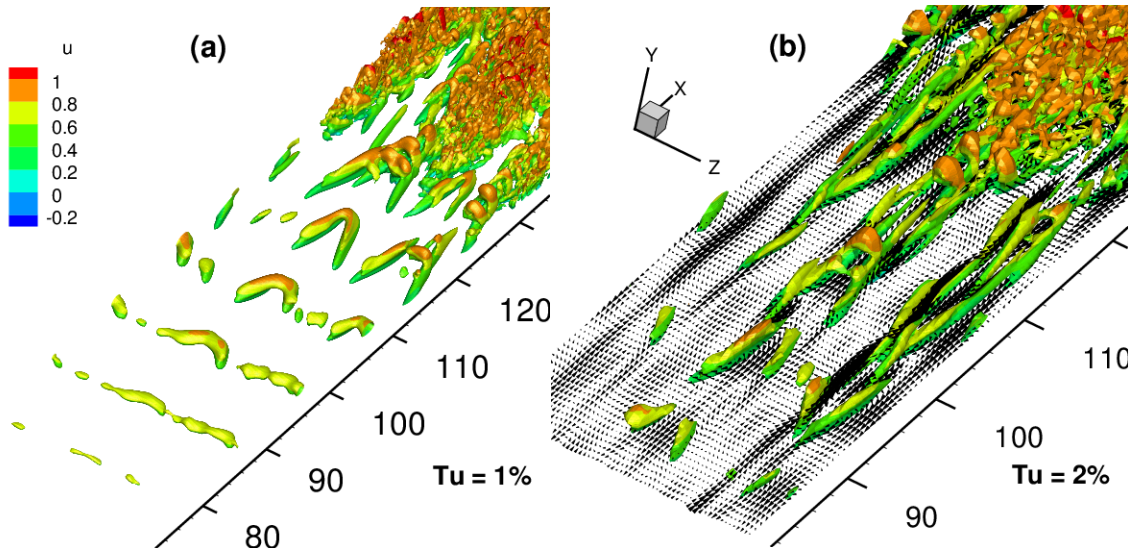

Figure 3.5: Instantaneous isosurfaces of Q criterion, plotted for $Q = 0.01$, color contoured by streamwise mean velocity u plotted for $A = 1\%$: (a) for $Tu = 1\%$; (b) $Tu = 2\%$. In the plot for $Tu = 2\%$, the in-plane perturbation velocity vectors are shown at $y = \delta_0/3$. Every other grid point has been used in both streamwise and spanwise directions to clearly show the vectors.

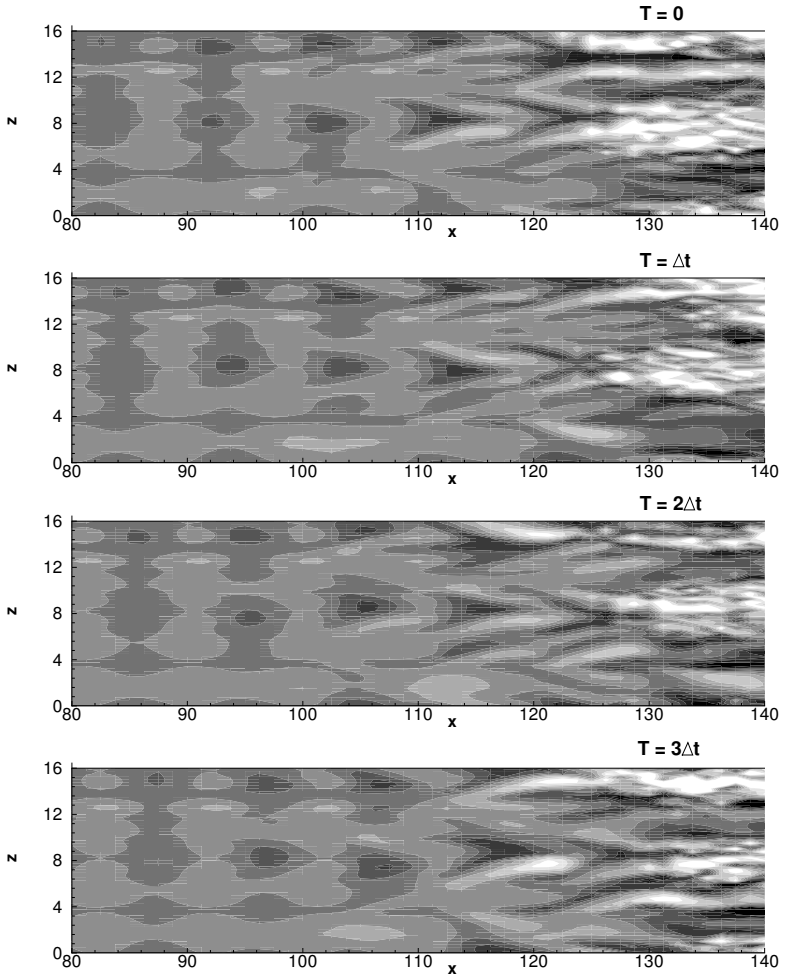

Figure 3.6: Instantaneous u' velocity component, for $Tu = 1\%$ and $A = 1\%$ at $y = \delta_0/3$. Contours are plotted for $-0.2 \leq u' \leq 0.2$. The frames are separated by $\triangle t = 0.09\tau$ where τ represents one flow-through time.

but less steeply (Phillips, 1969; Durbin and Wu, 2007).

In the lower part of the figure, streamwise elongated vortices can be noted; however, they are not of Λ form. These long streamwise vortices, associated with lifted streaks are, perhaps, a more characteristic response of a boundary layer undergoing transition through a bypass route. Hence, for moderate free-stream forcing of $Tu = 2\%$, the bypass route already tends to affect the final stages of the transition process. However, the streamwise vortices in figure 3.5 retain a nominal streamwise variation at the TS wavelength. Note that this modulated bypass route is seen adjacent to a line of Λ vortices: bypass and orderly routes coexist.

In figure 3.6, contours of the streamwise fluctuation velocity (u') are plotted at representative time instants, in a plane located at wall normal height $\delta_0/3$, for $Tu = 1\%$ and TS $A = 1\%$. The frames are separated by a constant time interval in which the TS wave travels $\triangle x \sim 10$ downstream, with phase speed $c_{TS} \sim 1/3$. The darker contours are negative values. From the figure it becomes apparent that the streamwise fluctuation due to streaks is of the same order of magnitude as the TS wave ($1\% - 10\%$). Vertical light and dark patches due to the TS wave become fragmented.

Close to the inflow, the TS waves remain intact, as the induced streaks have lower amplitude. The streaks and the TS wave grow in magnitude while convecting downstream. The TS wave grows at a slow viscous scale, while the streaks grow algebraically (Phillips, 1969; Landahl, 1980). When the fast growing streaks become of same order of magnitude as the TS wave, this shows up in contour plots of u' (figures 3.4 and 3.6).

The formation and evolution of a Λ vortex may be observed from the plots in figure 3.6. In the top frame, at $x \sim 83$ the trough of a TS wave is just noticeable, around the midspan location. It sits beneath a negative streak. In the very next trough downstream, the formation of a Λ vortex has already begun. A developed Λ vortex can be seen at $x \sim 110$. In the next frame, the trough previously seen at $x \sim 83$ has moved to $x \sim 93$. The vortex previously seen around $x \sim 110$ has intensified and is now at $x \sim 120$. It starts breaking down close to its tip, at $x \sim 127$. In the next frame, the vortex seen in the previous frame at $x \sim 93$ has moved to $x \sim 103$. The core of the negative patches intensify as the vortices move downstream. This region belongs to the zone in between the two legs of the Λ vortex. In the lowest frame, the

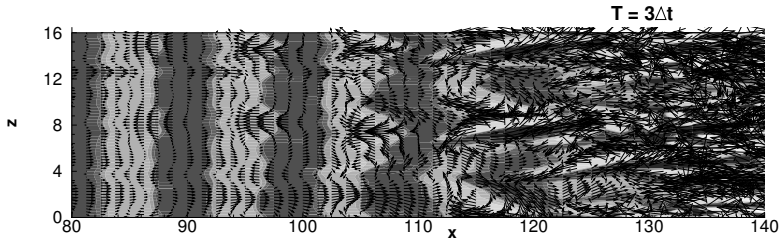

Figure 3.7: Instantaneous v' velocity component, for $Tu = 1\%$ and $A = 1\%$ at $y = \delta_0/3$. Contours are plotted for $-0.1 \leq v' \leq 0.1$. In-plane perturbation velocity vectors are also shown.

formation of this Λ vortex is complete and is centered at around $x \sim 115$. The vortex evolving just behind this one is not aligned in span, as can be clearly seen.

In figure 3.7, a v' contour plot and the in-plane velocity vectors are shown in the same plane and at the same time instant as in the bottom frame of figure 3.6. The darker are negative values. The streaks are streamwise velocity fluctuations, so they do not distort wall normal velocity profiles until they become intense, and tilt up from the wall (Jacobs and Durbin, 2001; Durbin and Wu, 2007). The secondary instability is manifested in the v' contour plots only after the Λ vortices form. Then, the flow in between the legs of the Λ vortices sees strong lift-up, creating upstream directed, perturbation velocity vectors in these regions. The streamwise stretched, positive v' contours, after $x \sim 110$, are the tip regions of Λ vortices.

The patterns of Λ vortex evolution observed in our work are distinctively different from H or K type secondary instability (Herbert, 1988). In figure 3.6, it may be observed that the vortices are not exactly aligned with each other in the span. It is also obvious from the figures 3.5, 3.6 and 3.7 that neither of the rows of Λ vortices are staggered relative to the next row, as is seen in H-type secondary instability of a TS wave.

Borodulin et al. (2006, 2011) performed experiments on natural transition in adverse-pressure gradient, flat-plate boundary layers in controlled environments (the free-stream turbulence levels were kept below 0.06%). Broadband TS waves were excited at the wall by 'deterministic noise'. The perturbation signal was random both in time and space. The resultant patterns of Λ vortices obtained in their work was irregular. However, it was quite different

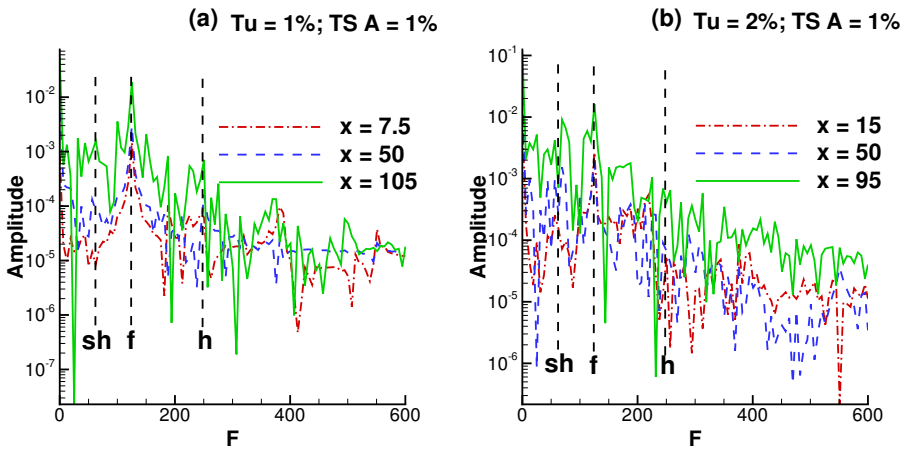

Figure 3.8: Frequency spectrum of the streamwise perturbation velocity u' at midspan, at the wall normal location where u'_{rms} is maximum, at indicated streamwise stations. f=TS frequency, sh=subharmonic, h=harmonic.

to the present DNS, in which the vortices are formed by streaks caused by free-stream modes.

Liu et al. (2008a) and Liu et al. (2008b) performed DNS and Floquet analysis of the interaction of streaks induced by a single OS continuous mode and a discrete mode. They observed that the pattern of Λ vortices was determined by the parametrically excited streamwise mode with the highest growth rate. Their simulations contained Klebanoff streaks and is therefore relevant to our DNS, even though the streaks were of fixed frequency and spanwise wavenumber. In our computations, the forward and backward perturbation jets within the boundary layer are a result of free-stream turbulence generated with a spectrum of modes and, therefore, the penetrating perturbations do not have definite frequency and spanwise wavenumber. However, the duration and spanwise scale of the streaks do determine the instantaneous pattern of the Λ vortices.

The forward and backward perturbation jets within the boundary layer are a result of free-stream turbulence generated with a spectrum of modes and, therefore, the penetrating perturbations do not have definite frequency and spanwise wavenumber. However, the duration and spanwise scale of the streaks do determine the instantaneous pattern of the Λ vortices. In figure 3.8, frequency spectra of u' are plotted at three stations, for both of the free-stream

turbulence intensities. The streamwise coordinates of these stations are indicated in the corresponding plots. These points are located at midspan and at the wall normal distance where u'_{rms} is maximum. The free-stream turbulence forces a broadband spectrum of disturbances within the boundary layer. The nondimensional fundamental frequency (marked as f in the plots) corresponds to the TS wave with $F = 124$. The subharmonic and harmonic frequencies are also shown. Close to the inflow, the fundamental frequency is the dominant mode; the streaks, comprising of frequencies lower than the fundamental, are at least an order of magnitude lower. The streaks grow faster in magnitude while traveling downstream. By the time the flow undergoes secondary instability, the low frequency components have grown to the same order of magnitude as the fundamental. For $Tu = 2\%$, the low frequency spectrum fills in and grows to higher levels than the primary TS wave.

In the mixed mode transition DNS and Floquet stability studies by Liu et al. (2008a,b), both wide ('mode 2' cases) and narrow ('mode 5' cases) streaks with constant spanwise wavelength were forced by an OS continuous mode. The TS mode remains the same in the results presented herein and their studies except its amplitude. The streamwise pattern had been attributed to the difference in phase speeds of the discrete and continuous modes and therefore remained same in both cases. Under the effect of broadband disturbances presented here, the instantaneous streaks are not periodic in time and hence the pattern evolution is less regular (figures 3.6, 3.7 and 3.8).

Liu et al. (2008a) performed DNS and Floquet stability analysis of the interaction of streaks induced by a single OS continuous mode and a discrete mode. In wide streak ('mode 2') cases of Liu et al. (2008a), the spanwise wavelength of the Λ vortices exactly matched with the OS continuous mode wavelength. In the DNS results presented herein, the spanwise size of Λ vortices is determined by the instantaneous width of the low-speed perturbation streaks which have approximate size in the range $1 - 1.5\delta_0$ which is very close to the spanwise size of the narrow streak cases ('mode 5') of Liu et al. (2008a). The spanwise separation of these vortices is determined by the width of the adjacent high-speed streaks. The spanwise separation in the current simulations lies in the range $4.5 - 6.5\delta_0$ which is again very close to the narrow streaks cases of Liu et al. (2008a). Therefore, it may be that an optimum spanwise size range exists for

the Λ vortices in which the secondary instability may effectively extract energy from the primary disturbances. Herbert (1988) had also indicated such optimum spanwise size parameter for natural transition through H-type secondary instability. Therefore, the interaction and pattern evolution of 'mode 5' cases are more pertinent to the present simulations. The description of the individual Λ vortices in the horizontal plane in narrow streaks cases of Liu et al. (2008a) are also similar to the present observations.

In figure 3.6, the Λ vortices are seen to break down at their tips. To illustrate the breakdown mechanism, a single Λ vortex may be followed. A single vortex is tracked by plotting a time series of the velocity field in a vertical plane passing through its tip. Figure 3.9 is a time series of the Λ vortex seen at $x \sim 110$ in the top frame of figure 3.6. The dark contours indicate negative spanwise perturbation velocity w', into the page and vice versa. In the top frame, the vortex just ahead of the tracked vortex has already started to break down. The in-plane vector field shows that the tip of a Λ vortex forms on a trough of the TS wave through which a backward streak is passing. The tip lifts up nearly to the edge of the boundary layer. The negative streamwise perturbation is highest close to the free-stream. Just beneath the tip of the Λ vortex, a small localized zone of high streamwise shear is created.

In the second frame, the tip of the vortex has elongated. Also, looking at the perturbation vector field, one can notice a streamwise wavy pattern evolving. In the third frame, the tip of the vortex has sheared off from the mother Λ vortex, and may be identified as an Ω shaped vortex loop in the Q isosurface plots. Once this loop is formed, it induces a strong wall normal perturbation. In the fourth frame a more complex pattern emerges prior to breakdown. The start of the Λ's forming, to eventual breakdown, occurs over a streamwise stretch of approximately three TS wavelengths.

3.3.2 Low to moderate free-stream turbulence intensity & low TS wave amplitude: streak breakdown

In the instantaneous plot for C_f as a function of Re_x, figure 3.2, we observed that neither $Tu = 1\%$ nor 2% was sufficient to trigger transition within our computational domain — even though low frequency streaks were generated and amplified within the boundary layer. In the

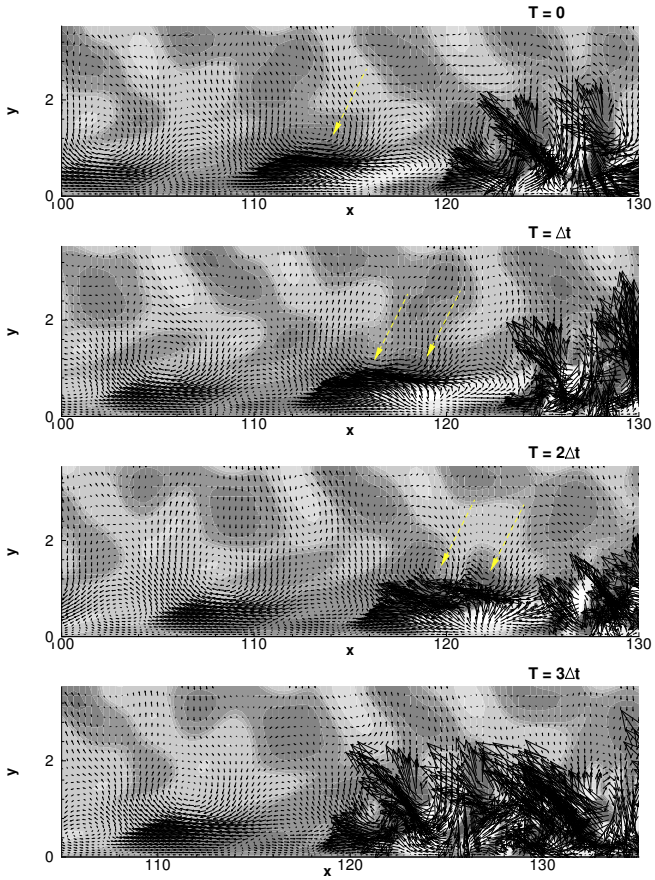

Figure 3.9: Instantaneous fluctuation velocity field for $Tu = 1\%$ and $A = 1\%$ in the vertical $x - y$ plane passing through the tip of a Λ vortex at representative times. Contours are plotted for $-0.05 \leq w' \leq 0.05$. In-plane perturbation velocity vectors are also shown. The frames are separated by $\triangle t = 0.025\tau$ where τ represents one flow-through time. The yellow arrows indicate the tips of the mother Λ vortex and the sheared off Ω shaped vortex.

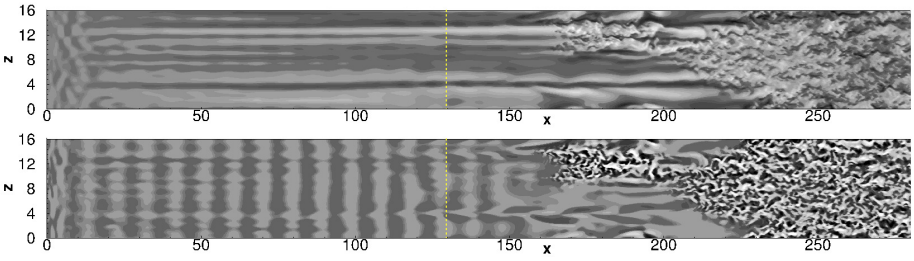

Figure 3.10: Instantaneous u' (top) and v' (bottom) contours for $Tu = 2\%$ and $A = 0.5\%$ in the horizontal $x - z$ plane at $y = \delta_0/2$. Contours are plotted for $-0.3 \leq u' \leq 0.3$ and $-0.1 \leq v' \leq 0.1$. The vertical dashed line indicates the upper-branch of the neutral curve at the TS frequency.

previous subsection, a strong TS wave was seen to undergo transition by secondary instability. In this section the TS wave is weaker ($A = 0.5\%$), and the mechanism that triggers transition is totally different. The observations in this case are quite novel.

With a weak TS wave at the inlet, the streaks now are of the same order of magnitude as it. This is evident from the u' and v' velocity contours in the horizontal plane at $y = \delta_0/2$, plotted in figure 3.10. In the u' contour plot (top frame) the TS wave is dominated by the low frequency streaks from inlet, onwards.

As expected, the TS wave shows up more prominently in the v' contour plot. Intensification of streaks, and decay of the TS wave after the upper branch, are apparent. Low momentum fluid, corresponding to negative jets, tends to lift up from the wall. As a result the vertical strips, indicating the TS wave, become increasingly distorted with downstream distance. Eventually, after the upper branch station, the v' contour plot also shows long streamwise streaks.

Λ vortices are not seen in these cases. Streak instability results in the genesis of turbulent spots, as in bypass transition. In figure 3.11, the peak value of u'_{rms} in the wall normal direction has been plotted as a function of Re_x for $Tu = 1\%$ and 2%. Both plots include the cases of excitation by free-stream turbulence, with and without the TS wave. u'_{rms} initially increases downstream at the same rate for both cases. A bit after the upper branch, u'_{rms} grows rapidly and the streak instability sets in.

Profiles of scaled u'_{rms} are plotted against y in figure 3.12, at stations upstream of break-

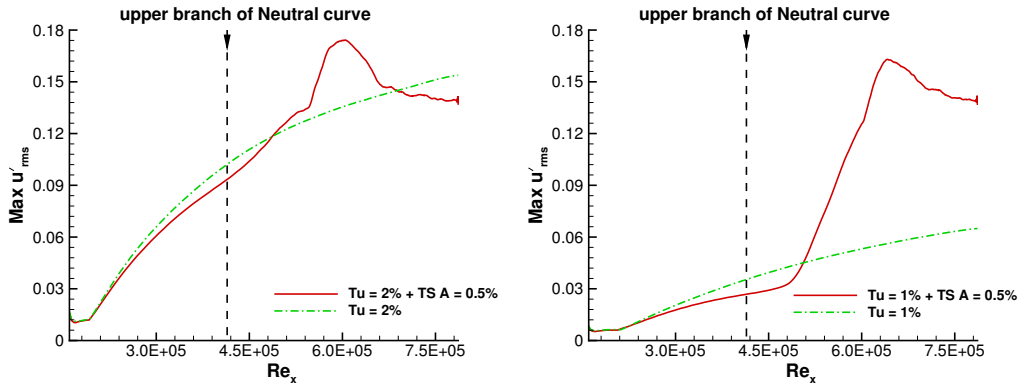

Figure 3.11: Maximum wall normal u'_{rms} versus Re_x: $Tu = 2\%$ (left) and $Tu = 1\%$ (right).

down, for both a strong and a weak TS mode. Inside the boundary layer, the strong TS mode case, plotted in the left frame of figure 3.12, resembles the TS eigenfunction prescribed at the inlet. (The free-stream turbulence appears to be higher at the left because the plots are scaled on local intensity.) This is the *inner mode* profile described in Vaughan and Zaki (2011). The inner mode becomes a TS eigenfunction in the limit of vanishing streak amplitude.

On the other hand, the peak *rms* for the weak TS mode case, shown in the right frame, occurs at higher wall normal heights than an *inner mode*. The wall normal height (y) of the $u'_{rms}(x)$ peak is $y/\delta_{99}(x) \sim 0.45$. This is a characteristic of secondary instability of streaks. As the flow evolves downstream, the tip of the profiles of u'_{rms} lifts higher from the wall for the low TS amplitude cases.

When only free-stream turbulence with low intensity ($Tu = 1\%$ and 2%) excites the flow, transition is not triggered within the domain; but in the presence of a mild TS wave ($A = 0.5\%$), the streaks undergo instability and transition after the TS wave starts decaying — that is, beyond the upper branch.

In figure 3.13, instantaneous vortical structures prior to transition have been visualized by isosurfaces of the Q-criteria for both Tu cases. The boundary layer is clearly more streaky for $Tu = 2\%$ than for $Tu = 1\%$. Also, while the decaying TS spanwise vortices may still be

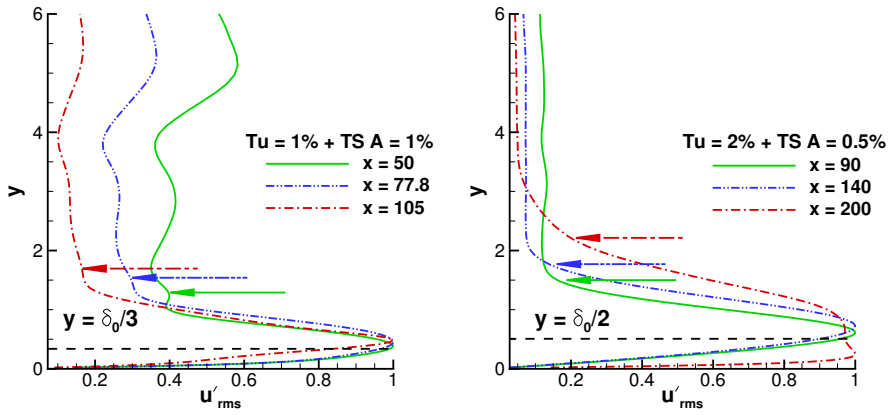

Figure 3.12: Scaled wall normal profiles of u'_{rms} at selected streamwise stations for a strong TS mode case (left) and a weak TS mode case (right). The horizontal black dashed lines indicate the wall normal height at which contour plots have been shown for the corresponding cases.δ_{99} at each station has been shown by an arrow with same color and legend as the profile legend.

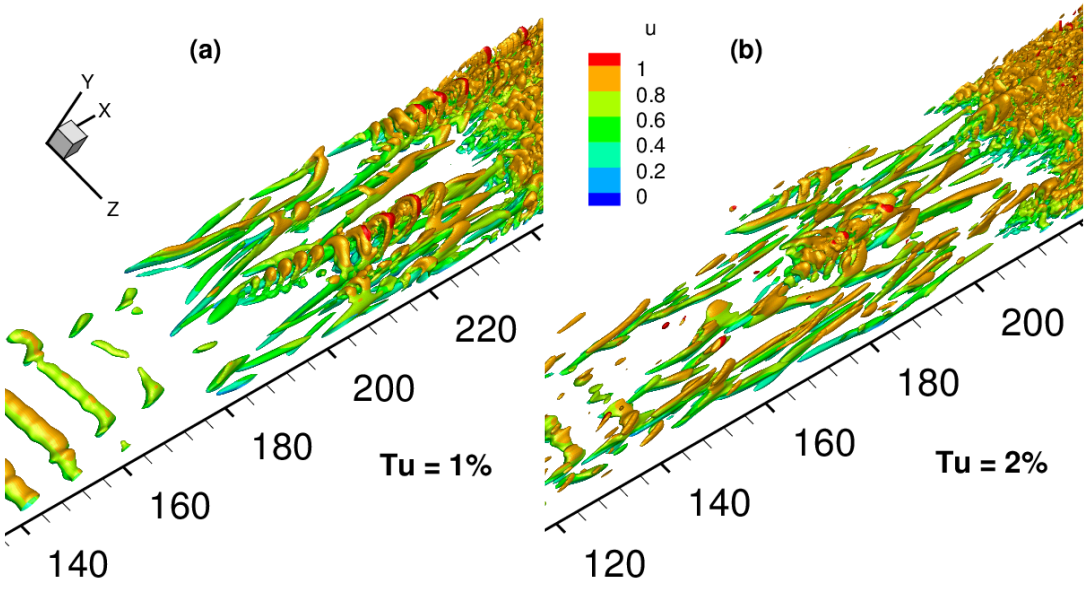

Figure 3.13: Instantaneous isosurfaces of Q criterion plotted for $A = 0.5\%$ depicting turbulent spots: (a) $Tu = 1\%$ and (b) $Tu = 2\%$. The surfaces are plotted for $Q = 0.002$ and color contoured by the mean streamwise velocity u.

identified for $Tu = 1\%$, in the $Tu = 2\%$ case, the TS rolls are not distinguishable. The data were saved at an instant when the turbulent spot formation takes place. For $Tu = 1\%$, the flow structures superficially resemble Λ vortices, but the legs of these vortices are much longer than the high amplitude TS wave case (figure 3.5). A closer look at the left frame reveals that some of the tips are not part of the long vortical structures. The long streamwise structures are streaks which lift up from close to the wall and are inclined towards each other. The apparent tips are actually roll-up vortices forming above the long streaks; they are a breakdown mode of elevated streaks. What is their nature?

The breakdown of streaks into turbulent spots is well documented (Zaki and Durbin (2005); Schlatter et al. (2008); Vaughan and Zaki (2011)). Undulations have been described as having similarity to Kelvin-Helmholtz instability, or to sinuous, shear layer instability modes. However, the process is three-dimensional and localized in a short region. To illustrate the breakdown mechanism seen in our simulations, the perturbation velocity field is plotted in an $x - y$ plane passing through an incipient turbulent spot of figure 3.13. The contours are shown in figure 3.14. The wall normal velocity v' is contoured (dark contours are negative) and in-plane perturbation velocity vectors are shown, at five time instants, with equal time interval. The fourth frame of this figure corresponds to the same instant as figure 3.13.

A large wavelength streamwise wave pattern may be observed in the top frame of figure 3.14. As the undulating instability travels downstream, it intensifies. As shown in the fourth frame from the top, the perturbations ultimately roll-up, then break down to turbulence. The approximate wavelength before breakdown is $2\delta_0 - 2.5\delta_0$ which is shorter than the waves seen in the top frames, with wavelength $\sim 10\delta_0$. Recall that the TS mode wavelength is approximately $\sim 10\delta_0$. The phase speed of the long waves is $\sim 1/3$ (similar to the inlet TS wave) while the speed of the shorter waves, that break into turbulence, is $\sim 1/2$. So, the streak instability appears to be triggered by the TS mode, but the TS mode does not play a direct role in the ultimate breakdown mechanism.

Figure 3.15 shows contours of streamwise perturbation velocity in the same $x - y$ plane as figure 3.14. A Kelvin cat's eye pattern is prominently identifiable in this figure. This plot is similar to figures in Zaki and Durbin (2005) and Schlatter et al. (2008).

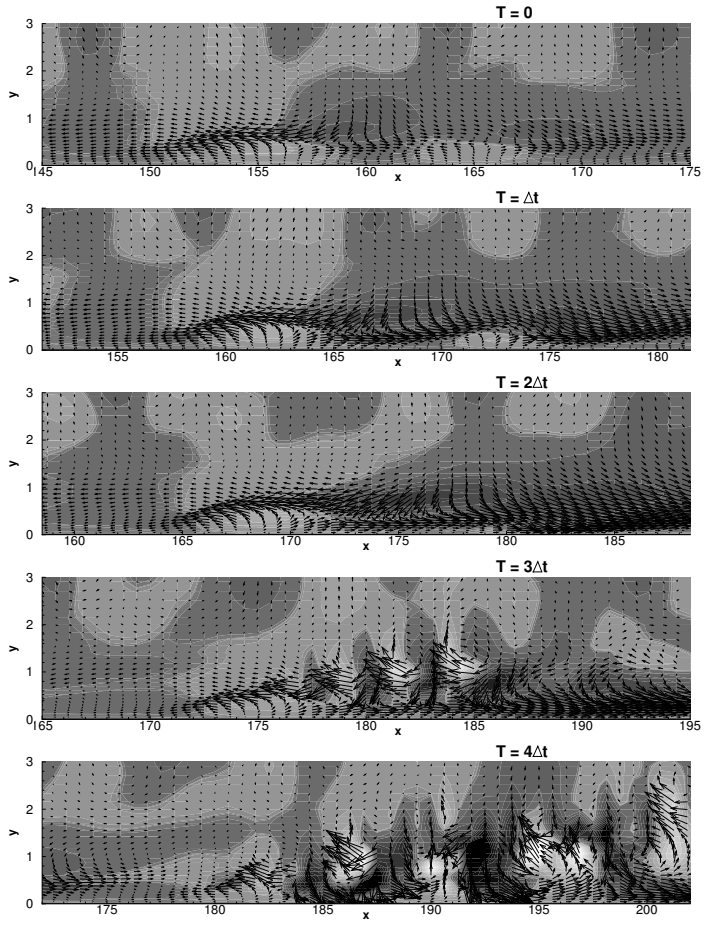

Figure 3.14: Instantaneous v' contours for $Tu = 2\%$ and $A = 0.5\%$ in the $x - y$ plane passing through the incipient turbulent spot in figure 3.13(b) at representative times. Contours are plotted for $-0.1 \leq v' \leq 0.1$. In-plane perturbation velocity vectors are shown. The frames are separated by $\triangle t = 0.0625\tau$ where τ represents one flow-through time.

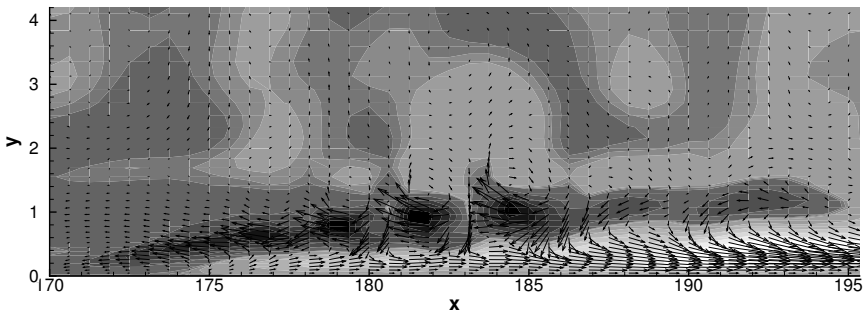

Figure 3.15: Instantaneous u' field for $Tu = 2\%$ and $A = 0.5\%$ in the $x - y$ plane passing through a turbulent spot at a representative time instant in figure 3.13(b) . Contours are plotted for $-0.3 \leq u' \leq 0.3$. In-plane perturbation velocity vectors have been shown.

Streak instabilities have been described previously (Zaki and Durbin, 2005; Schlatter et al., 2008; Vaughan and Zaki, 2011; Hack and Zaki, 2014; Andersson et al., 2001). Brandt et al. (2004) described the secondary instability of streaks as progressing through either spanwise symmetric (varicose) secondary instability or antisymmetric (sinuous) structures. Both Vaughan and Zaki (2011) and Hack and Zaki (2014) designate the secondary instability modes of streaks as sinuous or varicose type. None of these previous works had a TS wave in their inlet spectrum. The present visualizations have a different appearance; the undulations before breakdown are *helical*.

A negative streak superimposed on a mean profile may be imagined as a far wake profile, while a positive streak may be imagined as a streamwise jet. From a stability perspective they can be regarded as positive and negative jet profiles. In linear stability studies of axisymmetric jets, the perturbation quantities are written such that streamwise harmonic disturbances include a phase variable to accommodate modes that may spiral around the jet axis. In normal mode analysis, the exponential growth rate for axisymmetric wakes and jets are written as (Batchelor and Gill, 1962)

$$[u_x, u_r, u_\phi] = [\hat{u_x}(r),\ \hat{u_r}(r),\ \hat{u_\phi}(r)]\, e^{ik_x(x-ct)+in\phi}$$

where, the integer $n = 0$ implies toroidal axisymmetric modes and $n \neq 0$ are helical modes.

In reporting inviscid instability of axisymmetric jets, Batchelor and Gill (1962) show that for a smooth jet velocity profile, only $n = 1$ yields amplifying disturbances. For the top hat jet velocity profile all possible k_x and n were found to be unstable. In the monograph on jet instability by Michalke (1984), for several velocity profiles, the critical Reynolds number for the $n = 0$ mode was found to be greater than for $n = 1$, implying that the latter modes are always more likely to trigger transition. Both Batchelor & Gill and Michalke's analyses were inviscid. Among linear viscous instability studies, Kambe (1969) reported the first nonaxisymmetric mode ($n = 1$) to be most unstable. Similar predictions were made by Lessen and Singh (1973) and Mollendorf and Gebhart (1973).

The structures seen prior to streak breakdowns have striking resemblance to axisymmetric and nonaxisymmetric modes in wake/jet instability. This motivated us to look into the three dimensional picture of streak breakdown from the perspective of the instability modes of jets (positive streaks) and wakes (negative streaks). From here onwards, following the convention used in instability of wakes and jets, $n = 1$ refers to helical modes.

In figure 3.16, time evolution of isosurfaces for a specific negative streamwise perturbation velocity have been plotted for both free-stream turbulence intensities ($Tu = 1\%$ and 2%) with TS amplitude $A = 0.5\%$. Frames (a) to (e) are for $Tu = 2\%$ while frames (f)–(h) are for $Tu = 1\%$. Frames (c) and (g) are the same time instant at which Q isosurfaces were plotted in figure 3.13. Contours for wall normal fluctuation velocity are shown in the vertical $x - y$ plane in frames (c) and (g); they clearly have the Kelvin Helmholtz type appearance, that was identified via two dimensional plots in Zaki and Durbin (2005). The three-dimensional surfaces provide a different perspective.

The low-speed streaks are shown in frames (a) and (e). As these streaks travel downstream, wavy perturbations develop. The wavy perturbations are evident in frames (b) and (f). In frames (c) and (g), the helical modes are clearly identifiable; the wavy structure is spiralling around the streaks. The helical structures are clearer away from the wall than close to it, because the high shear and wall proximity invalidates the axisymmetric approximation.

The dark v' contours frames (d) and (h) in figure 3.16 represent negative wall normal perturbations. At the time instant of the plot, the helical structure corresponding to u' has

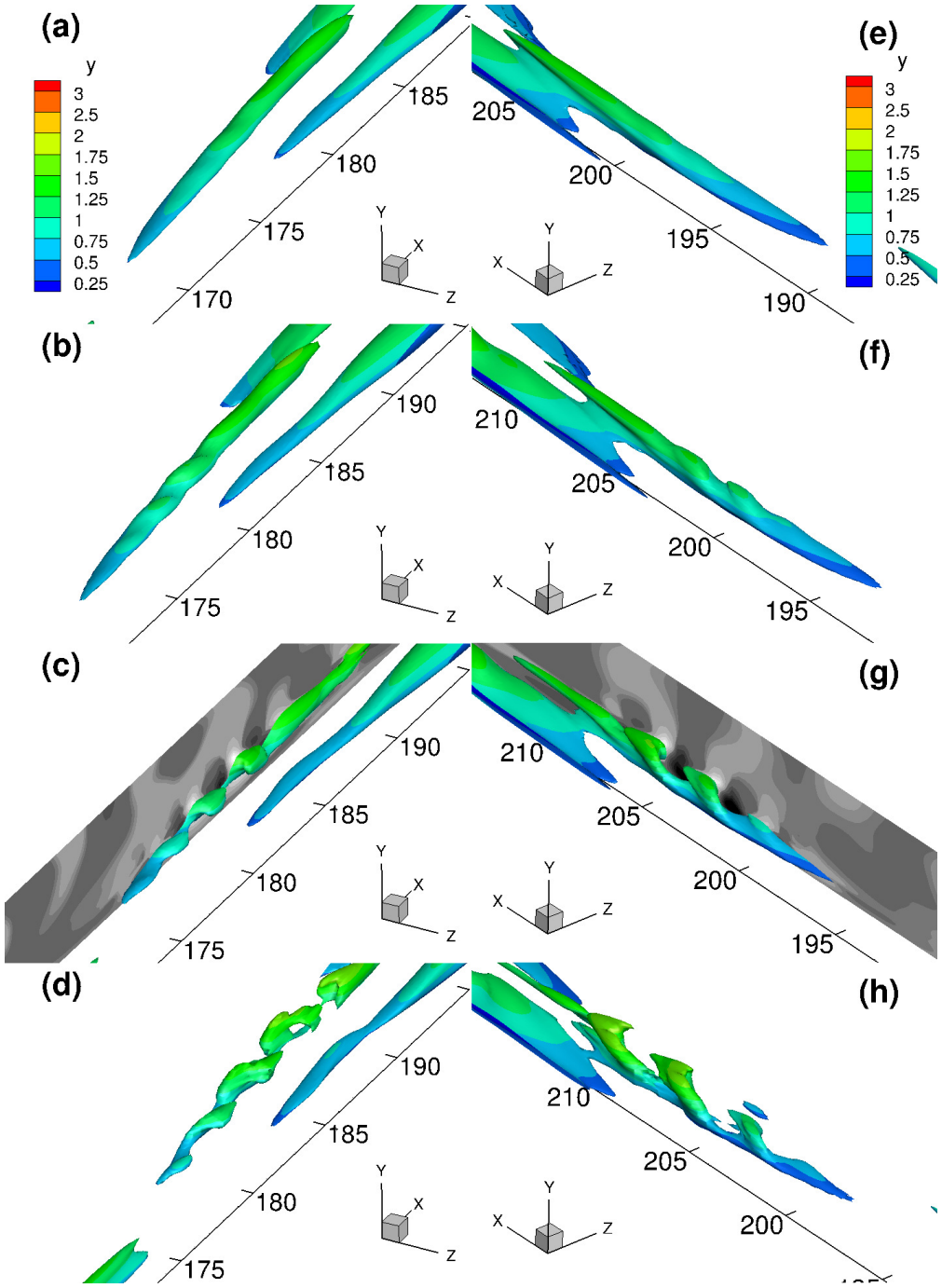

Figure 3.16: Time series of isosurfaces of u': (a)–(d) $u' = -0.2$ for the case $Tu = 2\%$ and $A = 0.5\%$ case; (e)–(h) $u' = -0.1$ for $Tu = 1\%$ and $A = 0.5\%$. (c) and (g) correspond to the same time instants as in figure 3.13. The frames are separated by $\triangle t = 0.01875\tau$ where τ represents one flow-through time. Isosurfaces are contoured by wall distance (y). In the $x - y$ plane, contours are plotted for $-0.1 \leq v' \leq 0.1$.

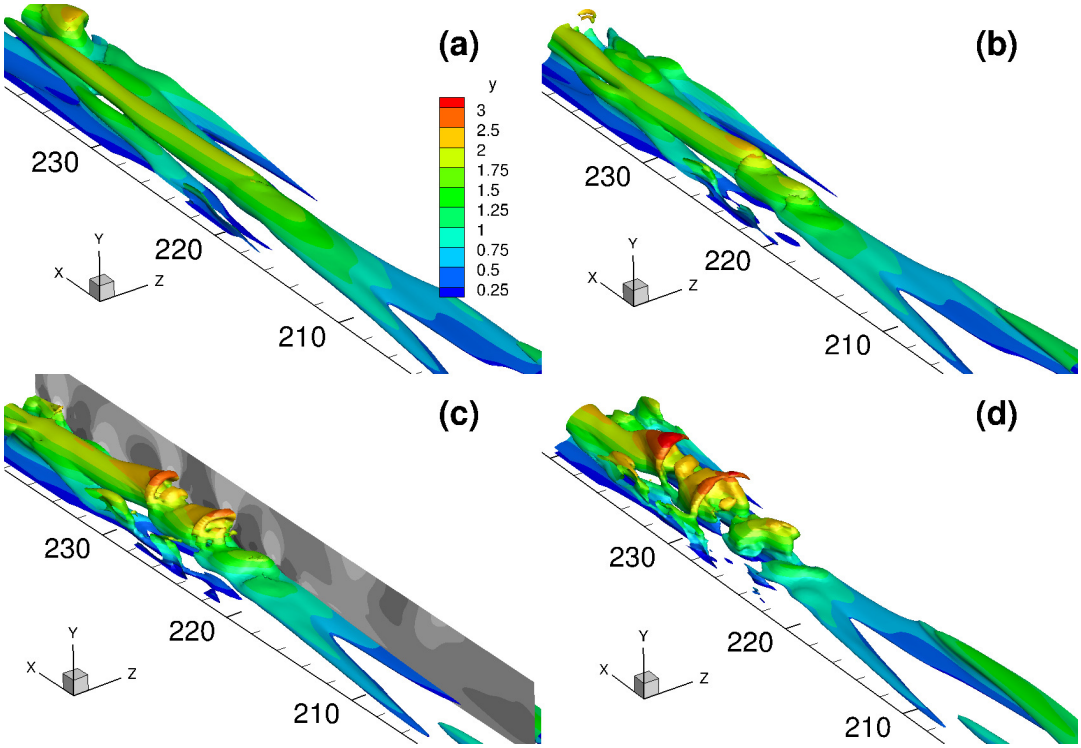

Figure 3.17: Time series of isosurfaces of $u' = -0.05$ for $Tu = 1\%$ and $A = 0.5\%$ case. The frames are separated by $\triangle t = 0.01875\tau$ where τ represents one flow-through time. Isosurfaces are contoured by y. Contours are plotted for $-0.2 \leq v' \leq 0.2$ in the vertical plane in frame (c).

phase $\phi = \pi$ (assuming the conventional anticlockwise increment of ϕ) at the same streamwise location that v' is at its peak ($\phi = \pi/2$), thus implying a phase difference of $\pi/2$ between the u' and v' components. This is indeed the case for normal mode eigenfunctions for jets and wakes: continuity, imposes an automatic phase difference of $\pi/2$. The time sequence in figure 3.16 is representative of features seen repeatedly in animations. For the $Tu = 1\%$ case, the $n = 1$ mode preceded breakdown in *all of the spot formation sequences* that we visualized in the course of one and a half flow-through times. For $Tu = 2\%$, the $n = 1$ mode was the precursor to breakdown in some, but not all instances.

For $Tu = 2\%$ no instance of $n = 0$ was seen. For $Tu = 1\%$, though, a few instances of the $n = 0$ mode, extending above the boundary layer, were observed. Hence, one can expect to find both of these modes, as well as their superpositions, appearing for low turbulent intensity. In figure 3.17, a time series of u' isosurfaces has been plotted, at a constant time interval, for a case showing the $n = 0$ mode. The toroidal mode shape may be clearly identified in frames (c) and (d). The isosurfaces show that the flow structures are symmetric in the spanwise direction w.r.t. the unstable negative streak. The y-contours coloring the surfaces indicate that the mode is seen at the edge of the boundary layer. The mode decays inside the boundary layer due to shear and loses symmetry w.r.t the center line of the negative streak.

The v' contours in the $x - y$ plane depict the wavy nature of the disturbances. Streamwise fluctuation velocity contours in horizontal planes slicing through the spot at different wall normal heights are shown in figure 3.18. The tip of the toroidal $n = 0$ mode may be identified by the streamwise harmonic nature of the contours in the top frame. As the plane is moved closer to the wall, the positive contours split into two maxima on the two sides of a negative streak. In the last frame closest to the wall, the low-speed streak is flanked by the streamwise harmonic positive and negative u' contours. The contours are approximately symmetric, corresponding to $n = 0$. The streamwise wavelength of this mode may be calculated from figure 3.18 as $\sim 4.25\delta_0$, which is almost double the wavelength of the $n = 1$ mode.

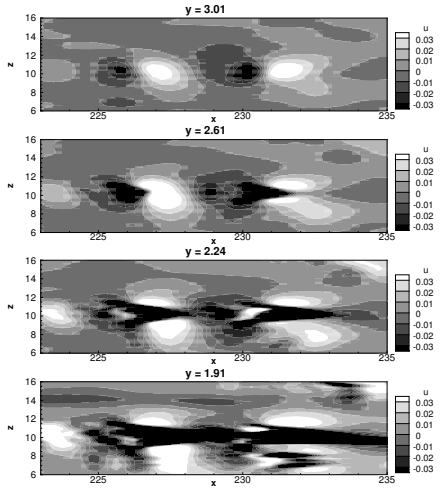

Figure 3.18: Streamwise fluctuation velocity contours in $x-z$ planes at gradually decreasing wall normal heights cutting through $n = 0$ secondary instability mode at the same instant as figure 3.17(c) for $Tu = 1\%$ and $A = 0.5\%$. δ_{99} at $x = 230$ is 2.22.

3.3.3 High free-stream turbulence intensity: bypass transition

This is the least interesting case, as it is similar to bypass transition. In the plots of C_f in figure 3.3, the high $Tu = 3.5\%$ cases were seen to transition at approximately the same streamwise Reynolds number in the presence or the absence of the TS wave. Several other papers looked into cases of bypass transition of zero pressure gradient boundary layers (Jacobs and Durbin, 2001; Durbin and Wu, 2007; Schlatter et al., 2008; Hack and Zaki, 2014; Brandt et al., 2004). None of these contained a TS wave. However, the transition mechanism observed in presence of the strong TS wave in our simulations is similar to the bypass mechanism in those previous papers: The negative streaks move up toward the top of the boundary layer. They are perturbed by higher frequency free-stream turbulence and localized streak instability leads to a turbulent spot forming.

In figure 3.19, contours of the u' and v' components of the perturbation velocity are plotted in a horizontal plane at $y = \delta_0/2$. The breakdown of streaks through spot formation is clearly visible. The streaks have a low frequency compared to the TS wave. Their amplitude as large at the TS wave, if not more. The TS mode is visible in the v' contour plots. In this case though, the distortion of the TS mode takes place much earlier due to high lift-up associated

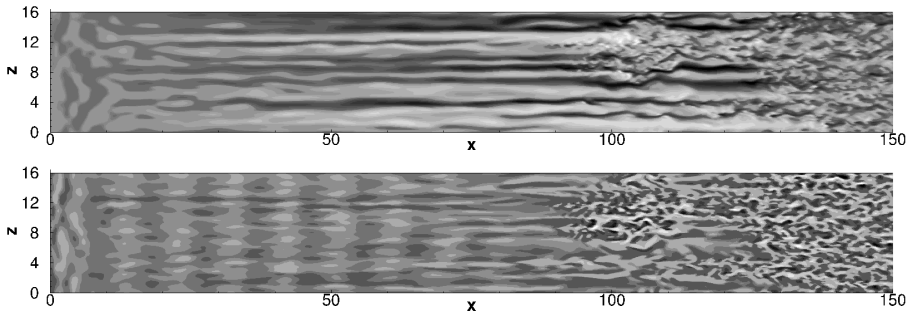

Figure 3.19: Instantaneous streamwise (top) and wall normal (bottom) fluctuation velocity contours for $Tu = 3.5\%$ and $A = 1\%$ in the $x - z$ plane at $y = \delta_0/2$. Contours are plotted for $-0.4 \leq u' \leq 0.4$ and $-0.15 \leq v' \leq 0.15$.

with strong, narrow, low-speed streaks.

In figure 3.20, flow structures prior to breakdown are shown by isosurfaces of $u' = \pm 0.15$ at the same time instant as the contour plots in figure 3.19. In the top frame of this figure, long streamwise streaks are depicted. In the lower frame, the zone surrounding the turbulent spot at $x \sim 100$ is zoomed, and shown in plan view. The bottom frame contains highlighted rectangular boxes, drawn by dashed lines. The contours within these boxes show fluttering negative streaks, as they break down to form another turbulent spot. These flickering low-speed jets are surrounded by high-speed jets which are relatively stable. The evolving perturbations are somewhat antisymmetric w.r.t. the negative streak, and therefore might be designated as sinuous. These are quite different in form from the helical breakdown at lower turbulent intensity (§3.3.2). The helical undulations travel with speed $\sim 1/2U_\infty$ while the sinuous undulations move with speed $\sim U_\infty$.

3.4 Conclusion

Flow regimes exist where interaction of Tollmien-Schlichting waves and Klebanoff streaks instigate transition, while either is insufficient by itself. They are instances of mixed mode transition. Direct simulation was used to study mixed mode regimes. Several routes to transition were observed, as a function of the TS amplitude, A, and turbulence intensity, Tu.

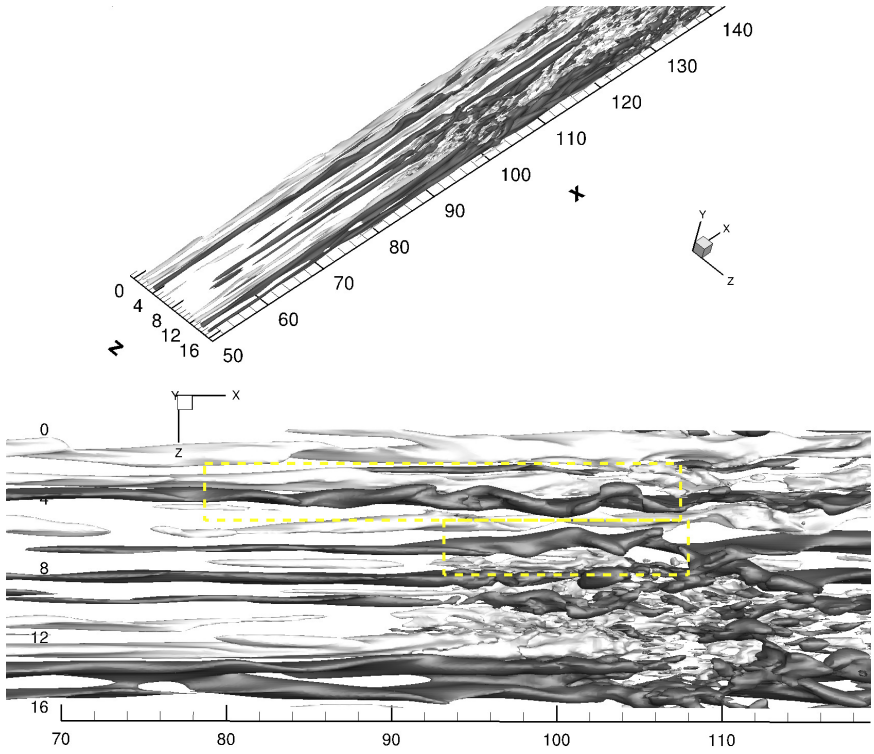

Figure 3.20: Isosurfaces of $u' = -0.15$ shaded dark and $u' = 0.15$ shaded light, for $Tu = 3.5\%$ and $A = 1\%$, at the same time instant as in figure 3.19. In the bottom frame, a top view of structures prior to spot formation are shown.

In absence of an inflection point in the velocity profile, bypass transition is the dominant mechanism for high turbulence intensity ($Tu = 3.5\%$). Bypass transition was observed even in presence of a strong TS mode ($A = 1\%$). A 'flickering instability', occurs on elevated, negative jets, and rapidly breaks down to form turbulent spots.

The TS wave plays a more direct role when the intensity of free-stream turbulence is low. For $Tu \leq 2\%$, Klebanoff streaks distort the TS wave. The distortion grows and develops into Λ vortices. The Λ vortices align with negative jets, and their spanwise size depends on the width of the jets. They have close to the spanwise size of the most unstable subharmonic secondary instability found by Herbert (1988); however, frequency spectra and flow visualization show clearly that the secondary instability is neither K nor H type. They are highly unstable and break down from their tips within 2 to 3 TS wavelengths after their inception.

The transition mechanism at lower TS wave amplitudes ($A \leq 0.5\%$) and moderate Tu is completely different, and quite fascinating. Undulation of the streaks initiates the process of transition. In isosurface plots of the perturbation velocity they appear as helical shapes. They move with 1/2 of the free stream speed. With $Tu = 1\%$ most turbulent spots that were observed in the present simulation developed as a helical breakdown. The symmetric $n = 0$ mode also was detected for weak streaks, but this mode is most noticeable outside the boundary layer, and usually does not lead to a turbulent spot.

The TS mode starts to decay after the upper branch station. Nevertheless, it is required for helical breakdown to occur.

Although the present study is of a zero pressure gradient boundary layer with a TS wave prescribed at the inlet, mixed mode transition will play a greater role in adverse pressure gradient boundary layers. Instabilities grow naturally on the inflectional profile. Hence, mixed mode transition can occur in a natural setting, without prescribing TS waves at the inlet.

CHAPTER 4. MIXED MODE TRANSITION IN APG BOUNDARY LAYERS: INTERACTION OF INSTABILITY WAVES AND KLEBANOFF STREAKS

4.1 Introduction

Boundary layer transition in zero pressure gradient (ZPG) has been studied quite extensively thus far, both experimentally and by simulations. Two possible transition mechanisms are the orderly natural transition and the bypass routes (White, 1991). In the Intoduction section, both orderly and bypass routes have been discussed in some detail. Perhaps to emphasize on these two transition routes, experiments or simulations have largely been performed at either very low or high disturbance levels. But in simulations of mixed mode transition in ZPG, three instead of two routes were identified. The intermediate regime was specifically interesting. In this regime, strength of both free-stream disturbances and TS waves were weak. A new type of breakdown, helical breakdown (Bose and Durbin, 2016b) was observed. This regime was only observed in presence of the both disturbances with both contributing significantly towards amplifying perturbations. In APG, instability waves may arise 'spontaneously' (Gostelow et al., 1994). Therefore, mixed mode transition is a far more likely scenario in APG boundary layers.

Transition in adverse pressure gradient (APG) boundary layers is more complex, simply because, the TS waves amplify at a much faster rate as the base flow is inflectional. Experimental studies in APG thus far, for example, by Walker and Gostelow (1989) and Gostelow et al. (1994) demonstrate a few transitional phenomenon that are counter-intuitive. Walker and Gostelow (1989) observed that the TS waves spontaneously amplify in APG when free-stream disturbance level is low. Under controlled conditions, when free-stream turbulence level was less than 0.3%, flow transitioned even without explicitly exciting the TS waves! In similar

experiments, by Gostelow et al. (1994), at varying pressure gradient and free-stream turbulence levels, another intriguing observation was made. The transtion inception and length were shorter when $Tu \sim 0.3\%$ compared to $Tu \sim 1.2\%$! They speculated that TS waves participate in transition and very dangerous subharmonic instabilities trigger quick transition for $Tu = 0.3\%$. It is to be noted that free-stream tubulence levels in their experiments were similar to the intermediate regime in ZPG simulations (Bose and Durbin, 2016b). On the other hand, Abu-Ghannam and Shaw (1980) reported insensitivity of transition length at high turbulence intensity in APG. These experimental results are puzzling and contradictory. Beneath high level of free-stream disturbances, instability waves may be bypassed and flow could be dominated by the Klebanoff streaks. Therefore, it could be, that at intermediate levels of free-stream disturbance, spontaneously excited TS waves play a destabilizing role. Transition via modal interactions is likely. This provided motivation for current simulations in APG.

In the present work based on DNS of transitional APG boundary layers, free-stream turbulence level was between 0.1% and 2%. The pressure gradient level is similar to bypass transition simulations in APG by Hack and Zaki (2014). The discrete waves are indeed excited and remain intact in transitional regime at turbulence intensity $\sim 1\%$. The transition mechanism involved is essentially bypass, yet the modes of instability in the transitional regime prior to breakdown to turbulence are quite different than the instability modes observed at high turbulence intensities. Vaughan and Zaki (2011) by linear Floquet stability analysis showed that, in APG, inner varicose instabilities are dominant, while in ZPG, outer sinuous modes are more vulnerable. DNS by Hack and Zaki (2014) and Brinkerhoff and Yaras (2015) reaffirmed those predictions at considerably high free-stream turbulence intensities ($Tu \geq 3\%$). In the present simulations, perturbation field has been envisaged from a different perspective. At low $Tu \sim 1\%$, helical $n = 1$ type of modes as in normal modes for axisymmetric jets/ wakes were seen to trigger genesis of turbulent spots. Toroidal $n = 0$ modes mainly appear at the boundary layer edge and are relatively harmless. As the Tu is increased, the helical breakdowns were sudden and much more difficult to identify. Spot inception by outer sinuous instabilities increases at higher Tu.

4.2 Base flow

The motivation of the current simulations was to investigate the effect of adverse pressure gradient on mixed mode transition. Therefore, to facilitate comparison with zero-pressure-gradient (ZPG) simulations, velocity profile specified at the inlet is a ZPG boundary layer at Reynolds number (with respect to momentum thickness) $Re_\theta \sim 265$. Adversity in pressure gradient is applied by diverging the upper boundary of the computational domain in such a way so that the pressure gradient follows a power law. Impermeability and free-slip boundary conditions are applied for the velocity field in that boundary. The curvature of the upper wall is obtained in the following manner.

The 99% Blasius profile thickness δ_{99} is equated to the desired Falkner-Skan 99% thickness which fixes the fictitious leading edge location with respect to the inflow plane. Let this distance to be x_0. We assume Falkner-Skan flow from inlet onwards with Hartree parameter β_H. Then the continuity equation gives

$$[L_y(x) - \delta^*(x)]U_e(x) = \int_0^{Ly(x_0)} u dy \tag{4.1}$$

Here, $L_y(x)$ is the wall normal height of the upper boundary of the domain at a streamwise distance x from the inlet plane. In equation 4.1, $\delta^*(x)$ is the displacement thickness of the desired Falkner-Skan profile. The free-stream velocity $U_e(x) = (\frac{x_0+x}{x_0})^m$, where m is the usual power index related to Hartree parameter β_H and x_0 denotes the distance of the inlet plane from the leading edge. Through out this work $\beta_H = -0.14$ which is equal to that used in Hack and Zaki (2014). This method has been successfully used in recent studies of pressure gradient effects on bypass transition by Zaki and Durbin (2006) and Hack and Zaki (2014). In the left frame of figure 4.1, the scaled streamwise velocity profiles have been plotted at different streamwise locations. After an initial adjustment period ($x \geq 70$) velocity profiles for the base flow are in very good agreement with the corresponding Falkner-Skan similarity solution.

The pressure gradient parameter $\lambda_\theta = \frac{\theta^2}{\nu}\frac{dU\infty}{dx}$ provides a good measure for estimating streamwise pressure gradient imposed upon the boundary layer. In the right frame of figure 4.1, λ_θ has been plotted against streamwise distance x. This plot clearly shows the initial adjustment

period after which λ_θ remains fairly constant. The pressure gradient level matches well with that of the Falkner-Skan boundary layer with $\beta = -0.14$.

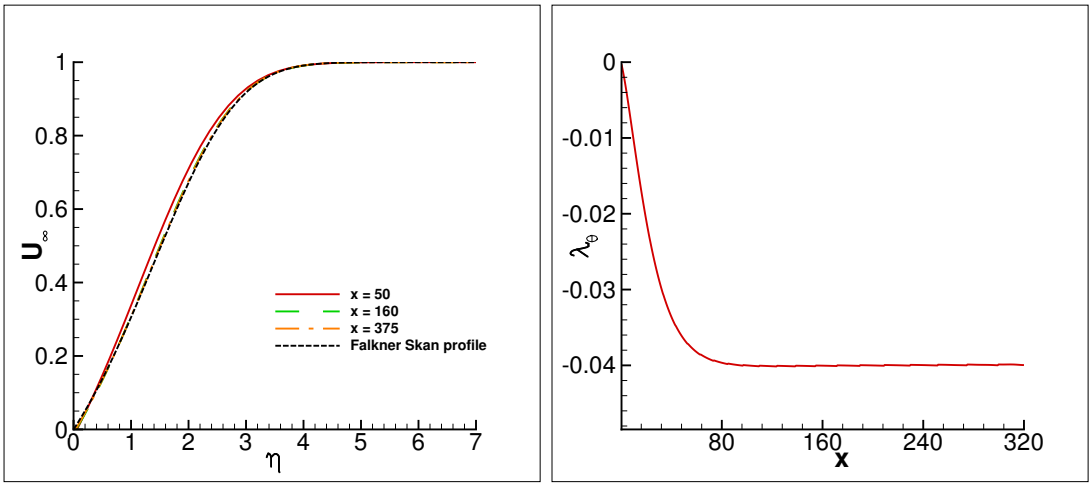

Figure 4.1: Left: U_∞ plotted against similarity variable η at selected streamwise stations. Right: Pressure gradient parameter λ_θ plotted against x.

4.2.1 Instability of the base flow

At selected $\beta_H = -0.14$, the velocity profile is inflectional. When a sufficiently long streamwise domain is used for base flow computation, linearly unstable modes of very small magnitude are excited spontaneously. The numerical noise instigates these instability waves which grow sufficiently quickly to become nonlinear within the computational domain. Instantaneous streamwise and wall normal perturbation velocity components u' and v' at a wall normal height $y = \delta_0/2$ (δ_0 is the inlet boundary layer thickness) have been plotted in the left frame of figure 4.2 to depict the excitation and gradual growth of the instability waves. At around $x = 400$, magnitude of u' attains as high a value as 1% of inlet free-stream velocity. Therefore, around this location the instability waves are likely to be weakly nonlinear. In the right frame of figure 4.2, instantaneous scaled $|u'|$ has been plotted against y/δ_{99}. The instability mode shape is that of an unstable Tollmien-Schlichting (TS) wave.

In the left frame of figure 4.3, frequency spectra of v' component has been plotted at $x = 210$. The peak amplitude is obtained at $\omega = 0.11$. There is another broad peak which is close to

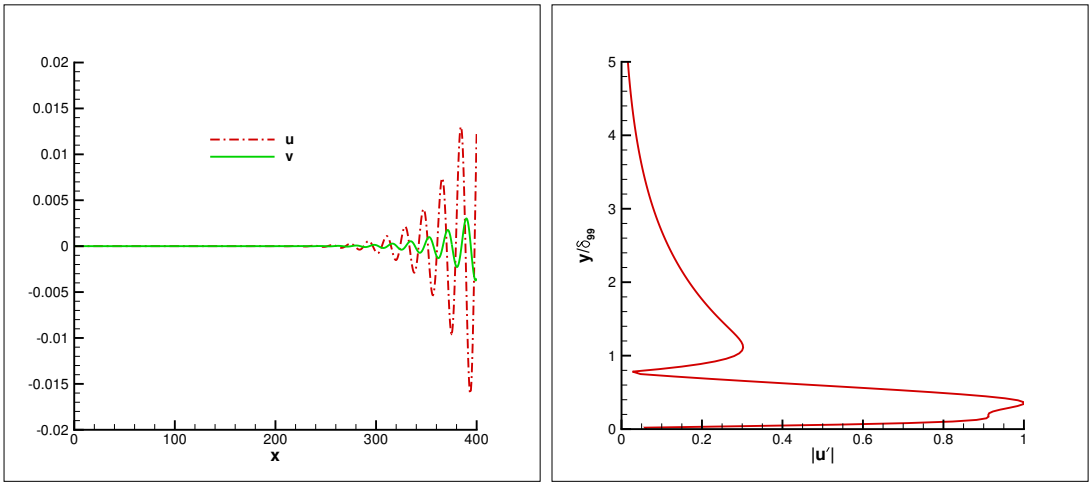

Figure 4.2: Left: Instantaneous u' and v' plotted against x at a wall normal height $\delta_0/2$. Right: Instantaneous scaled $|u'|$ versus y/δ_{99} at $x = 210$.

$\omega = 0.22$. The excitation source, numerical noise, is white noise with infinite bandwidth. Also, the background noise level will be different at different time steps as per instantaneous roundoff error. Hence, Several unstable frequencies inside the neutral curve are expected to be excited with different initial amplitudes. In this context, Walker and Gostelow (1989) and Gostelow et al. (1994) performed experiments of controlled transition on flat plate boundary layer under several adverse pressure gradient levels in a wind tunnel with very low noise level. At high adverse pressure gradients, under very low free-stream turbulence levels ($Tu < 0.1\%$), TS waves were excited spontaneously. They also obtained two peaks in their frequency spectra with frequency ratio 3 : 2. In our case, the second peak is close to the harmonic of the most excited wave.

In the right frame of figure 4.3, $\omega = 0.11$ corresponding to the peak in the frequency spectra has been shown in $(Re_{\delta*}, \omega_{\delta*})$ plane. $\omega_{\delta*}$ and $Re_{\delta*}$ are scaled with respect to the local displacement thickness $\delta*(x)$ and free-stream speed $U_\infty(x)$ at $x = 210$. The corresponding $Re_{\delta*}$ and $\omega_{\delta*}$ have been marked by dashed vertical and horizontal lines respectively. Contours have been plotted for the growth rate (k_i) for the spatially most unstable mode from the discrete spectrum of the OS equation. Clearly, the excited frequency in the DNS is very close to the locally most unstable TS wave. The slightest difference may be due to the non-parallel effect

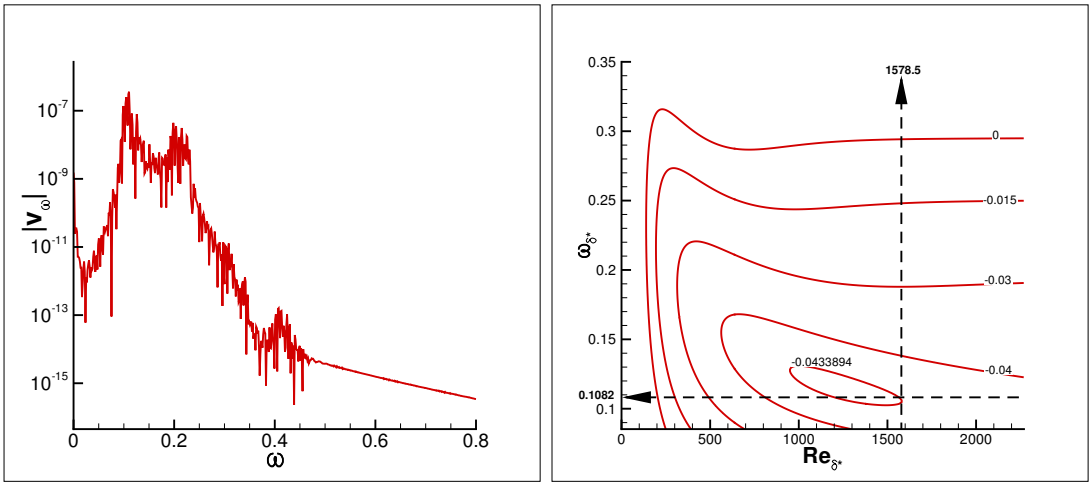

Figure 4.3: Left: Frequency spectra of v' at streamwise station $x = 210$. Right: Peak of the frequency spectra at $x = 210$ shown in plot for linear spatial instability growth rate (k_i) contour plot in $(Re_{\delta*}, \omega_{\delta*})$ plane.

Table 4.1: Summary of simulations.

Case name	Domain size ($lx \times ly \times lz$)	Grid size ($nx \times ny \times nz$)	Tu	Lowest nonzero inlet frequency (ω)
tu001s	$320 \times 40 \times 20$	$1024 \times 192 \times 160$	0.1%	0.636
tu001l	$480 \times 40 \times 35$	$1536 \times 192 \times 280$	0.1%	0.357
tu01	$320 \times 40 \times 20$	$1024 \times 192 \times 160$	1%	0.636
tu02	$320 \times 40 \times 20$	$1024 \times 192 \times 160$	2%	0.636

of the base flow. The linear stability theory predicted wavelength ($17.91\delta_0$) is also very close to the wavelength obtained from DNS ($18.25\delta_0$).

4.3 Excitation cases

Excitation cases were simulated with varying domain size and intensity of free-stream perturbations (Tu). The cases discussed here have been tabulated in table 4.1. The grid resolution has been maintained in all the simulations. Each case has been assigned a name in the table. The assigned short names have been used to identify the corresponding cases throughout this report.

Inlet, free-stream turbulence was synthesized from Orr-Sommerfeld and Squire continuous

modes, by the method of Jacobs and Durbin (2001), Brandt et al. (2004) and Hack and Zaki (2014). 32 modes for a set of frequency, wall normal wavenumber, and spanwise wavenumber were used. The Fourier coefficients for the Orr-Sommerfeld and Squire modes are isotropic, satisfy continuity, and are based on a von-Karman spectrum with the peak at wavenumber $k_p \sim 1$, nondimensionalized by the streamwise integral scale, L_{11}.

Free-stream decay of rms of u', v' and w' components have been shown in the left frame of figure 4.4. Turbulence remains fairly isotropic throughout the domain for all the free-stream turbulence intensities (Tu) considered. The pseudo-integral scale of turbulence is defined as $L_k = -k^{3/2}/(U_\infty dk/dx)$ where k is the kinetic energy of free-stream turbulence perturbations and U_∞ is the free-stream velocity at inlet. L_k scaled by the inlet boundary layer thickness (δ_0) is also shown in the right frame of figure 4.4 for all the cases considered. As expected, the pseudo-integral scale increases with downstream distance. L_k is smaller for lower free-stream turbulence intensities due to faster decay of small scale perturbations.

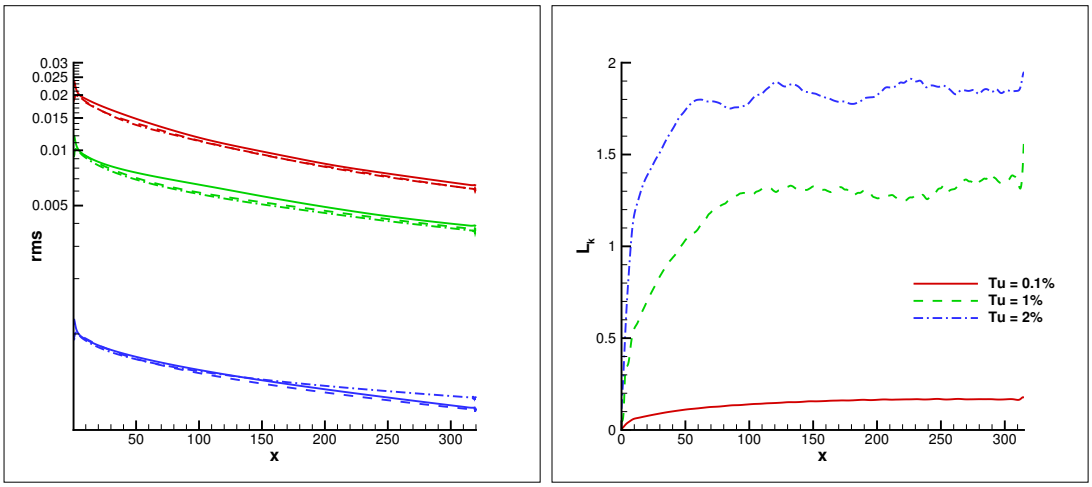

Figure 4.4: Left: u'_{rms}, v'_{rms} and w'_{rms} in free-stream plotted versus downstream distance x. Right: Pseudo-integral length scale (L_k) scaled by inlet boundary layer thickness (δ_0).

In the left frame of figure 4.5, instantaneous spanwise localized skin-friction coefficient C_f has been plotted against Re_x for all the cases mentioned and named in table 4.1. In the inset, a zoomed-in view of the curves is also shown. The presence of instability waves in all cases except case tu02 become apparent from this plot. It may be presumed that even beneath

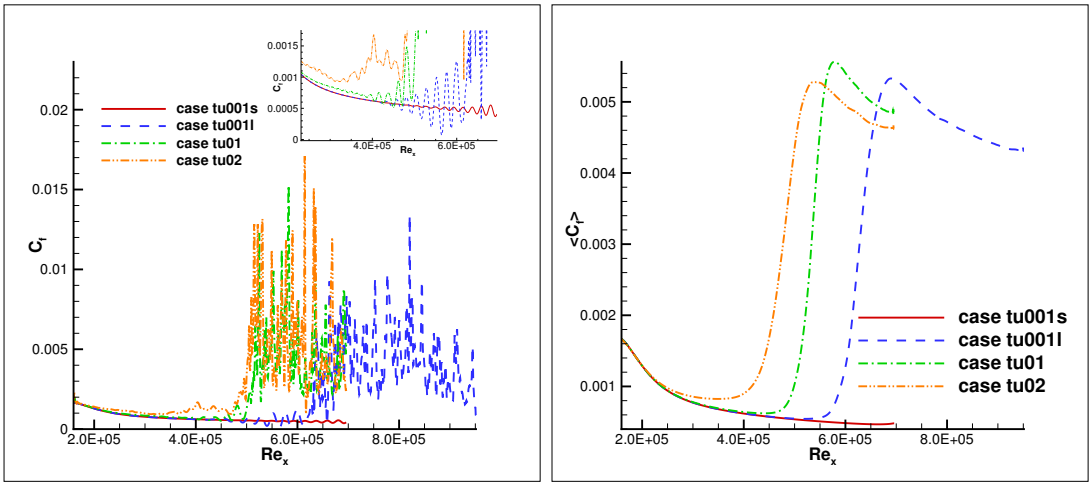

Figure 4.5: Left: Instantaneous spanwise localized skin-friction coefficient (C_f) plotted against Re_x for all cases tabulated in table 4.1. A zoomed-in view of the curves is shown in the inset. Right: Time and span averaged skin-friction coefficient ($< C_f >$) plotted against Re_x for all cases.

high intensity disturbances in free-stream ($Tu \sim 1\%$), instability waves play a significant role. Klebanoff streaks on the other hand are boundary layer response to free-stream disturbances. Hence some of the cases considered are truly mixed mode transition. Yet, there is significant difference in the transition routes undertaken.

In the right frame of figure 4.5, the mean skin-friction coefficient $< C_f >$ has been plotted versus Re_x for all cases. It is clear from both plots in figures 4.5 that for the very low intensity case ($Tu = 0.1\%$) simulated in shorter domain (case tu001s), the flow remains laminar within the computational domain. That is why the large domain case (case tu001l) was simulated. Case tu001l transitions within the larger computational domain considered. Even under same level of free-stream forcing, cases tu001s and tu001l have drastically different instability routes. As Tu at inlet is increased by an order of magnitude ($Tu = 1\%$ and 2% cases) transition is triggered well within the computational domain. Transition Reynolds number is sensitive to free-stream turbulence intensity in the range of $Tu \leq 2\%$. It was reported by Abu-Ghannam and Shaw (1980) that for $Tu \geq 3\%$, the transition onset becomes independent of Tu. On the other hand, at very low Tu, the effect of it is more pronounced as this regime is dominated

Table 4.2: Transition onset and completion locations for all cases.

Case name	Transition onset Re_x (x)	Transition completion $Re_x(x)$
tu001s	–	–
tu001l	5.2×10^5 (211.25)	6.9×10^5 (316.5)
tu01	4.4×10^5 (163.75)	5.8×10^5 (247.5)
tu02	3.5×10^5 (109.3)	5.4×10^5 (224.3)

by orderly transition. Therefore, it may be argued that apart from disturbance magnitude, transition onset, breakdown and its characteristic route is significantly dependent upon the spectral content of the free-stream disturbances, as is shown here.

Throughout the text, transition onset and completion locations for the excitation cases have been referred to. In table 4.2, Reynolds numbers and streamwise locations of transition inception and completion for all cases have been tabulated. The onset of transition is assumed to be the location where $< C_f >$ is minimum in the right frame of figure 4.5. Similarly, completion of transition has been assumed to be the location where $< C_f >$ is maximum. A contrasting attribute may be identified by comparing the transition lengths (distance between onset and completion of transition) for the three cases where transition is triggered within the domain. The transition length is longest for the case tu02 indicating spot formation is abrupt which spreads downstream to complete transition process. This indicates a bypass scenario. Transition length is minimum for the case tu01 implying that either spot spreading rate is higher or breakdown is more evenly spread out along the span. The second possibility is characteristic of orderly transition. For the case tu001l on the other hand, transition length is longer than the case tu01 even though orderly transition is a more likely scenario for this case (Gostelow et al., 1994). This could be due to irregular inception and breakdown of Λ vortices. It is found herein that this is indeed the case. Another reason for longer transition length for the case tu001l compared to tu01 case could be the effect of the periodic boundary condition in the spanwise direction. Nonetheless, transition route evidently influences the transition length.

The following subsections separately describe the instability and transition mechanisms observed for various excitation cases tabulated in table 4.1.

4.3.1 Case tu001s

In figure 4.5, it is shown that the case tu001s does not transition within the shorter computational domain. Instability waves are instigated inside the boundary layer which grow and move out of the domain before secondary instability is triggered. In figure 4.6, streamwise perturbation velocity (u') contours have been plotted in horizontal planes at indicated wall normal heights w.r.t. the inlet 99% boundary layer thickness, δ_0. Far away from the wall, turbulence is almost isotropic. As the planes are moved closer to the wall, streamwise instability waves become apparent from $x \sim 240$ onwards. At $y = \delta_0/2$, the instability waves are almost 2 dimensional. Prior to the instability waves, low frequency weak Klebanoff streaks are seen. Only low frequency components of the free-stream disturbances penetrate the boundary layer (Hunt and Durbin, 1999). But the Klebanoff streaks are weak and so is the lift-up effect. It is intriguing that the low frequency Klebanoff streaks are followed by spanwise coherent 2D instability waves!

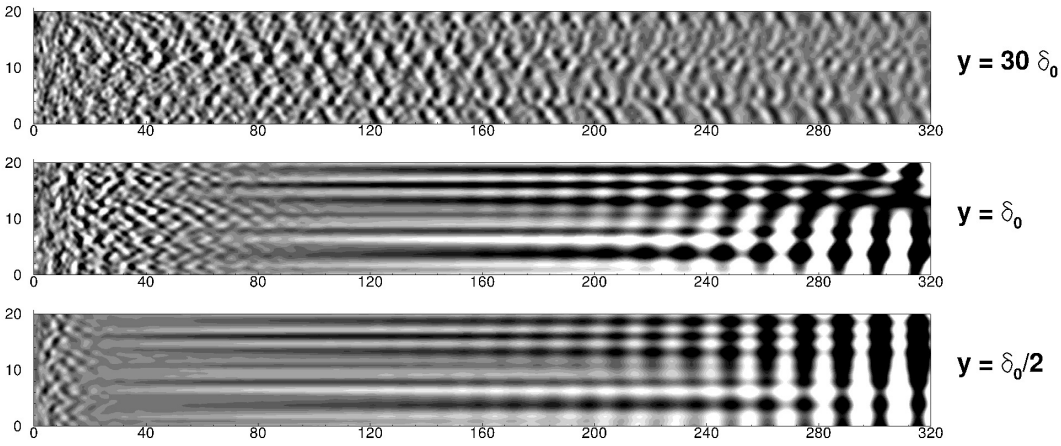

Figure 4.6: Instantaneous $-0.001 \leq u' \leq 0.001$ contours in horizontal $x-z$ planes at indicated wall normal heights for case tu001s. The z axis has been enlarged by a factor of two. Dark is negative.

In figure 4.7, contours of instantaneous wall normal perturbation velocity component (v') has been plotted at the same horizontal planes as in figure 4.6. The Klebanoff streaks are manifested in the u' component. Therefore, the Klebanoff streaks are not seen in the v' contour

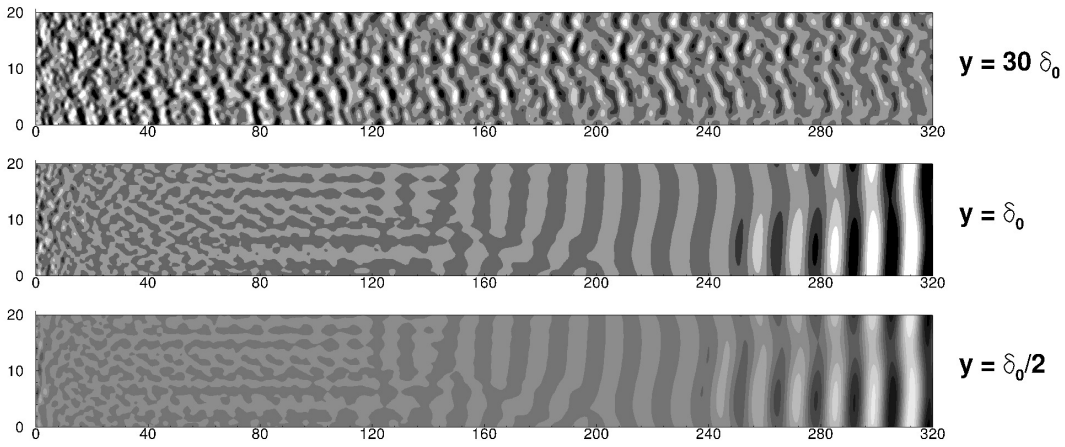

Figure 4.7: Instantaneous $-0.001 \leq v' \leq 0.001$ contours in horizontal $x-z$ planes at indicated wall normal heights for case tu001s. The z axis has been enlarged by a factor of two. Dark is negative.

plots. Consequently the instability waves are more clear in the v' contour plots. These appear as consecutive spanwise patches of light and dark contours.

In the left frame of figure 4.8, wall normal scaled u'_{rms} profiles have been plotted at indicated streamwise stations. The 99% boundary layer thickness of the mean streamwise velocity profiles at these stations have been marked by horizontal arrows. At $x = 100$, the peak of rms fluctuations is in the free-stream. A signature of Klebanoff streak is seen to be excited at this location. Around $x = 200$ the peak of the profile of u'_{rms} is around $y \sim \delta_0/2$. Further downstream, at $x = 300$, where the instability waves may be clearly identified in the contour plot has the peak of the u'_{rms} lower than that at $x = 200$. The rms profile is reminiscent of the TS waves with an upper lobe at the edge of the boundary layer. This plot indicate that a shift in critical layer takes place as the disturbances travel downstream.

The shift of the peak in the disturbance profiles towards lower wall normal heigths may be identified from instantaneous scaled $|u'|$ profiles plotted in the right frame of figure 4.8 at the same streamwise locations as in the left frame. In this plot the ordinate is the wall normal height scaled by the 99% boundary layer thickness at each station. This enables comparison of peak disturbance layers for streamwise thickening boundary layer. The peak disturbance layer

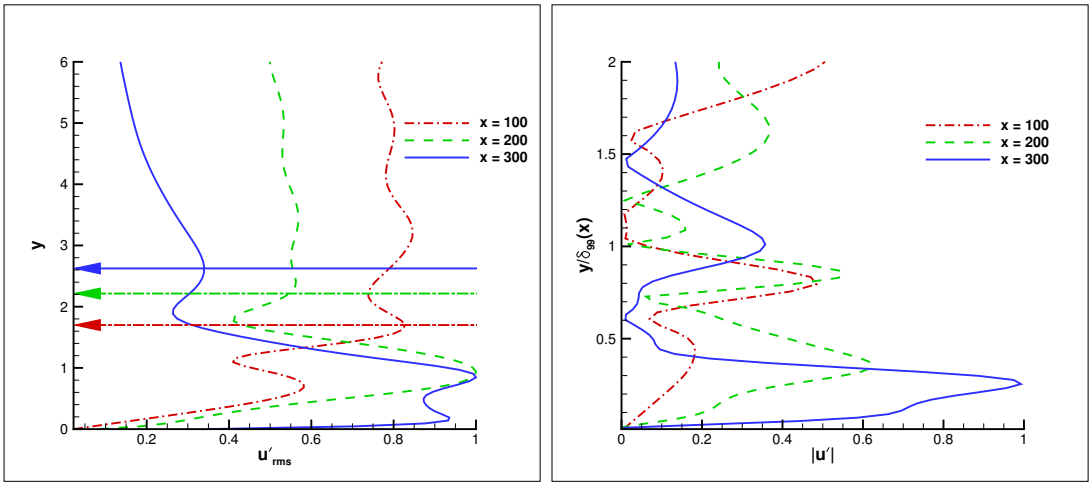

Figure 4.8: Left: Time and span averaged scaled u'_{rms} plotted against y at a few indicated streamwise stations for the case tu001s. The 99% boundary layer thickness at each station is marked by a horizontal arrow. Right: Instantaneous wall normal profiles of scaled $|u'|$ plotted against $y/\delta_{99}(x)$ at indicated streamwise stations for the case tu001s.

of the unstable TS waves is lower than the weak Klebanoff streaks upstream. The appearance of the $|u'|$ profile at $x = 300$ is very similar to TS eigenfunction.

In contour plots of perturbation velocities, excited instability waves remained 2D after their inception. But as the instability waves were also obtained while computing the base flow, 2D perturbation components were excluded from the inlet disturbance spectra. Time-averaged spanwise spectra has been plotted at inlet for u' in the left frame of figure 4.9. Here, the spanwise wavenumber (k_0) of the disturbances has been represented by the integer multiple of the wavenumber corresponding to the wave that spans over the full domain width i.e., $k_0 = k_z \frac{lz}{2\pi}$. Here, k_z is the actual spanwise wavenumber of the disturbance. This plot shows that the inlet disturbance has been generated excluding all possible disturbances with $k_0 = 0$ (excluding 2D disturbances).

In the right frame of figure 4.9, the evolution of 2D disturbances in the spanwise wavenumber spectra of u' and v' perturbations downstream of the inlet has been tracked by plotting the time-averaged amplitude of $k_0 = 0$. At the inlet, the amplitude is infinitesimally small for both u' and v'. Just downstream of the inlet, the amplitude of 2D perturbations jump to finite value. This

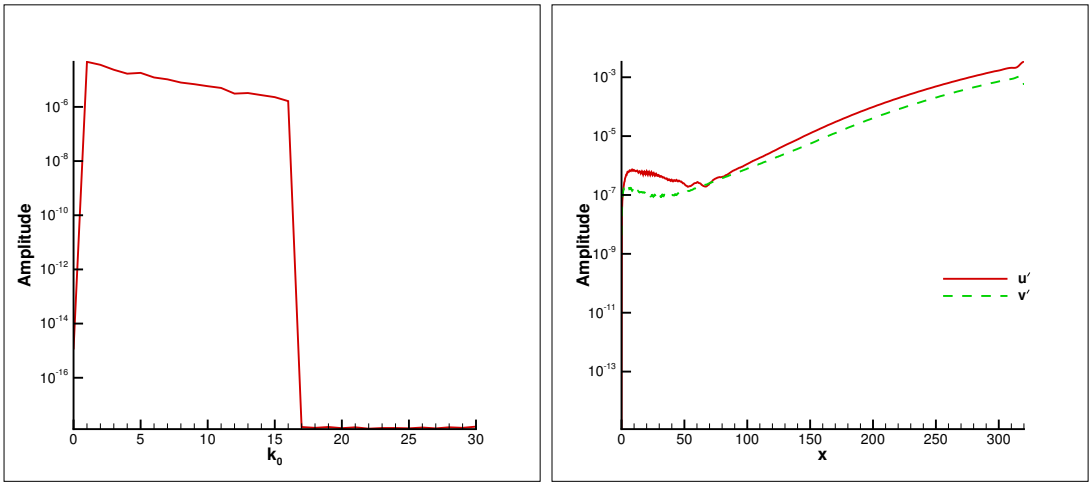

Figure 4.9: Left: Spanwise wavenumber spectra of u' component at inlet for the tu001s case. Here $k_0 = k_z \frac{l_z}{2\pi}$. Right: Time-averaged growth rate of $k_0 = 0$ wavenumber component with downstream distance x.

is most probably due to the initial cascading effect as the synthetic disturbances adjust itself inside the domain. The inlet disturbances are synthesized following the von Karman spectrum which does not include the dissipation range which is quickly established just downstream of the inlet. The 2D components of the u' perturbations initially grows up to $x \sim 15$ before decaying. The growth is weak because the disturbances are linear due to small forcing for $Tu = 0.1\%$. At around $x \sim 70$, the amplitude of $k_0 = 0$ for both components are almost equal after which u' grows faster than v'. The fact that the slope of amplitude growth of 2D modes for u' and v' are almost linear and approximately equal after around $x \sim 150$. The instability waves grow exponentially.

In figure 4.10, the frequency spectra of v' has been plotted at selected streamwise stations. Two inlet frequency modes are also seen within $\omega = 1$. As the flow develops downstream, frequencies lower than the smallest inlet frequency grows and the amplitude of the inlet frequency modes decay. Four frequencies with highest amplitude at $x = 300$ have been marked. The 2D instability waves in the contour plots after $x \sim 200$ have $\omega = 0.17$. This is expected to be the most excited linear instability mode of the time averaged mean flow.

The frequency spectra is broadband. The inlet modes are at higher frequencies than the

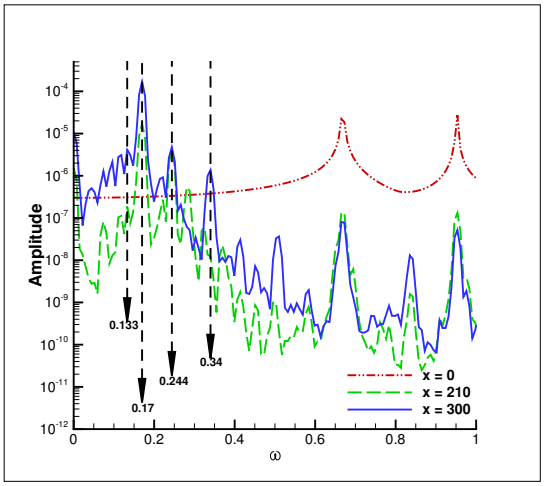

Figure 4.10: Frequency spectra of the v' component at specified streamwise locations for the case tu001s.

most excited 2D instability waves. How does the energy cascade up to higher scales? This could be due to nonlinear resonant triad interaction (Craik, 1971). The lower frequency of a triad must come from a weak Klebanoff streak induced by the free-stream disturbances. In simulations of bypass transition (Jacobs and Durbin, 2001), the Klebanoff streaks are obtained at much lower frequencies, close to $\omega \sim 0$. The interaction of these low frequency modes with the higher frequency free-stream disturbances could lead to excitation of intermediate frequencies. In Craik's resonance mechanism, a 2D disturbance interacts with two oblique disturbances with wavenumber and phase speed half of the 2D disturbance. But the critical layer of the triad must be the same for efficient transfer of energy. Here, the instability modes have lower critical layer than the continuous modes in free-stream. Moreover, in figure 4.9, purely 2D disturbances were seen to grow very quickly just downstream of the inlet. Therefore, resonant instability seems not to be the route of disturbance energy transfer. Nonetheless, once the linearly unstable modes are excited infinitesimally, those grow at a very high rate in APG. The Klebanoff streaks decay due to viscous dissipation after some distance if the disturbance magnitude is not high enough as is the case here.

In figure 4.11, the most unstable linear instability modes from solution of OS equation have been shown for the time and span-averaged mean flow at indicated streamwise stations. The

spatially unstable wavenumbers at a given station are shown in the right frame of figure 4.11 and their growth rates have been plotted as functions of frequency in the left frame of figure 4.11. The plot in the left frame helps in identifying the most unstable frequency at a given station. The most unstable frequency at $x = 30$ is neither of the frequencies marked in figure 4.10. As the flow develops downstream, the frequency of the most unstable mode decreases. The most dominant frequency at $x = 300$ is $\omega = 0.17$ (figure 4.10). But this frequency is the most excited only around $x \sim 140$. At $x = 210$, $\omega = 0.133$ is very close to being the most unstable frequency. This justifies why $\omega = 0.133$ is a peak at $x = 300$ in figure 4.10 but not so prominent at $x = 210$. The growth of $\omega = 0.17$ is evidently smaller than $\omega = 0.133$ between $x = 210$ and $x = 300$. Same is true for $\omega = 0.244$ which is the frequency of the most unstable mode at $x \sim 30$. This mode grows very quickly between inlet and $x = 210$. But, between $x = 210$ and 300, its growth rate decreases. This clarifies the existence of several peaks in figure 4.10. Locally the most unstable frequency grows the most but the unstable mode with the most energy dominates the frequency spectra. $\omega = 0.17$ should also decay as some other lower frequency mode should dominate the flow downstream of the outflow for case tu001s provided the disturbance amplitude does not grow too high for the instability waves to become nonlinear and secondary instability is initiated. This becomes more clear from the analysis of case tu001l.

The unstable wavenumber at all streamwise stations collapse on to a single curve at low frequencies is evident from figure 4.11. The unstable wavenumber corresponding to the most dominant mode at $x = 210$ is also marked in the figure. The wavelength predicted by the linear theory is $13.08\delta_0$ (for $k_r = 0.4805$ at $x = 210$). The average wavelength of disturbances from DNS around the same location is very close to this value at $13.44\delta_0$. The slight difference could be due to nonparallel flow effect which is more significant in APG. The other reasons could be the broadband nature of the disturbances in DNS calculations. The wavelength of the most unstable frequency at $x = 210$ is $18.93\delta_0$.

In figure 4.12, the downstream evolution of $\hat{u'}$ and $\hat{v'}$ for the four frequencies marked in figure 4.10 have been plotted. Plot for the u' component in the left frame of figure 4.12, shows that all four modes initially grow up to $x \sim 50$. The initial growth is due to nonmodal growth

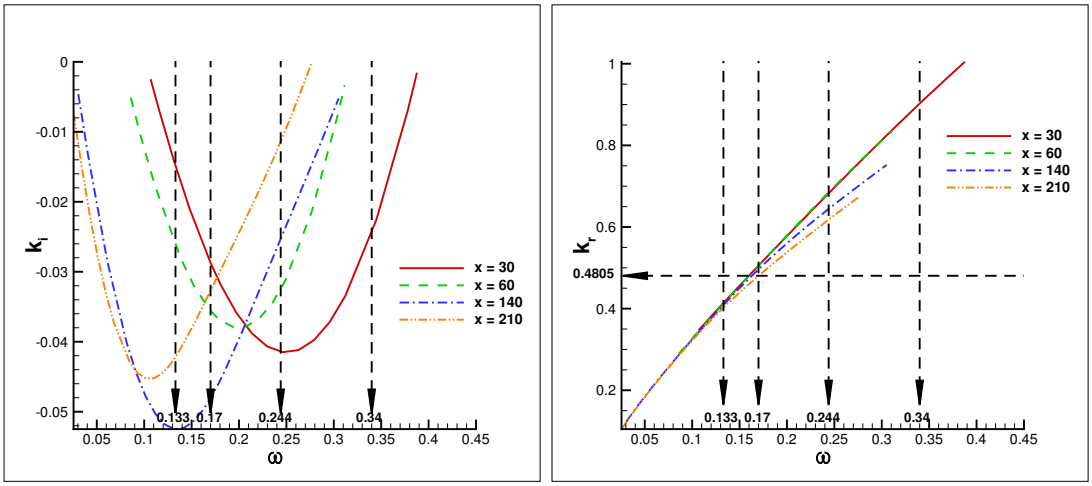

Figure 4.11: Left: Predictions of unstable frequencies by Linear Stability theory at indicated streamwise stations for the case tu001s. The frequency peaks marked in figure 4.10 are also shown. Right: Unstable wavenumbers (k_r) predicted by Linear Stability theory. The unstable wavenumber corresponding to most dominant frequency from DNS at $x = 210$ and 300 is also shown.

of initially infinitesimal perturbations as discussed earlier. It is followed by decay for all four frequencies. The perturbations do not decay at the same rate. The disturbances at these frequencies start growing again after travelling different streamwise distances. $\omega = 0.17$ starts growing earliest, around $x \sim 100$, where this has the highest growth rate as shown in figure 4.11. Disturbances with $\omega = 0.244$ also starts growing around the same streamwise location for the u' component. But as predicted by linear theory, v' disturbances with frequency $\omega = 0.244$ starts growing earlier than $\omega = 0.17$ (the right frame of figure 4.12). Once the disturbances with $\omega = 0.17$ starts growing, due to higher growth rate these reach much higher magnitudes. But the slope of the curves for $\omega = 0.17$ and 0.244 starts decaying close to the outlet indicating that the growth rate of these frequencies are less at the Reynolds numbers close to outflow. As predicted by the linear theory, disturbances with $\omega = 0.133$ start growing much later. $\omega = 0.34$ is the harmonic of $\omega = 0.17$. May be that is why it starts growing much later, only after the amplitude of disturbances with $\omega = 0.17$ reaches sufficient magnitude.

Case tu001s does not transition within the computational domain. Therefore, the domain size needed to be increased. From this case we observe that as the fluctuation amplitudes

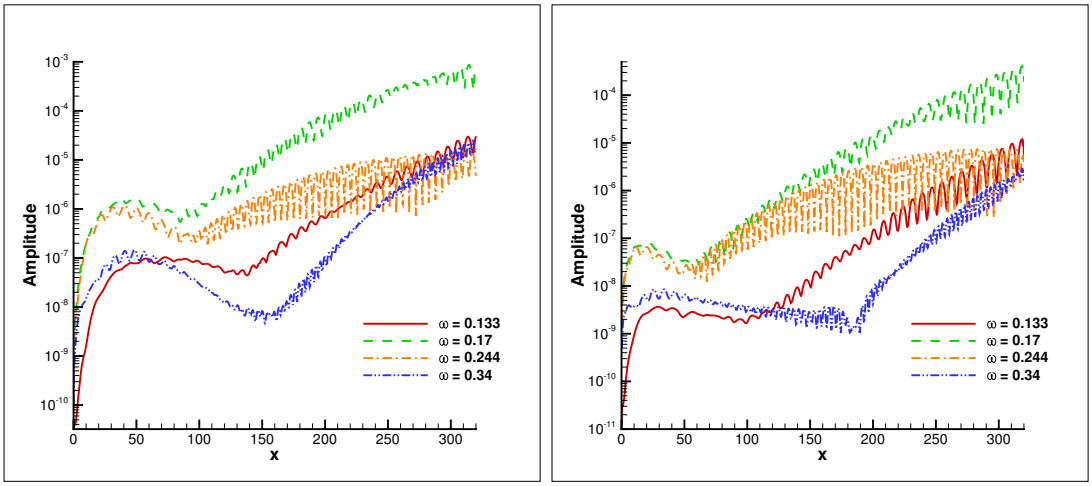

Figure 4.12: Left: Downstream growth of u' due to frequencies marked in figure 4.10. Right: Downstream growth of the same frequencies for v' component.

are low, the disturbances remain linear within the domain. The most unstable mode grows. For triggering early transition, inlet disturbances with frequencies close to linearly unstable regime are required. Therefore, for tu001l case, lowest inlet frequency of inlet disturbances is much lower compared to tu001s case. For case tu001l, transition is obtained. Hence that case demonstrates how spectral content of inlet disturbances is extremely important even at very low $Tu \sim 0.1\%$.

4.3.2 Case tu001l

In figure 4.13, instantaneous contours of u' and v' are plotted in the horizontal $x - z$ plane at a wall normal height $y = \delta_0/2$. The instability waves are clearly identifiable. From both u' and v' contour plots, the Λ vortices are identifiable around $x \sim 250$ which breakdown to trigger transition. An interesting fact is notable from the v' contour plot in the bottom frame. Three zones are identifiable from this plot which have been marked. The demarcation of these zones are depending upon evolution of the most dominant modes from frequency spectra which will be discussed later. In zone 1, the wavelength of the disturbances is shorter compared to those in zone 3. Wavelength transformation takes place in zone 2. The shorter instability waves are visible in the u' contour plot as well but those are distorted by Klebanoff streaks. This feature

was not present for case tu001s and must be due to the difference of the inlet disturbance spectra as all other parameters remained constant between the two cases.

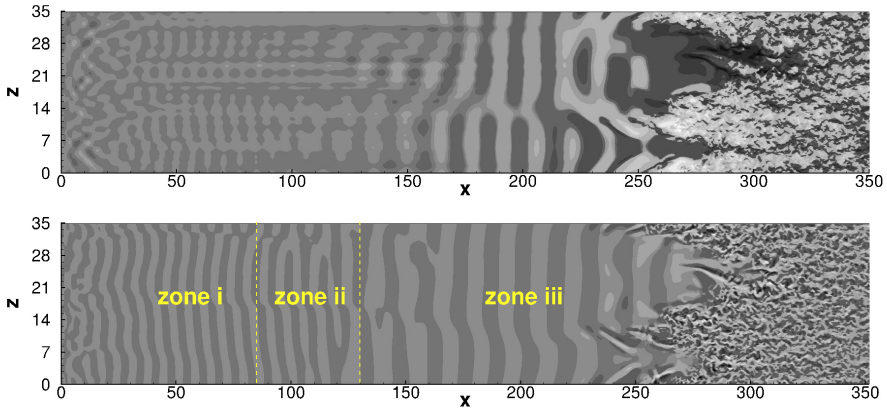

Figure 4.13: Instantaneous contours of $-0.4 \leq u' \leq 0.4$ (top frame) and $-0.2 \leq v' \leq 0.2$ (bottom frame) at a wall normal height $y = \delta_0/2$ for the case tu001l.

4.3.2.1 Primary instability: 2-D instability waves

In figure 4.14, frequency spectra of the u' component has been plotted at selected streamwise stations. The lowest excited frequency at inlet is $\omega = 0.357\delta_0/U_\infty$. The frequency spectra showed in this figure at other three stations are located in zones 1, 2 and 3 respectively. The lowest excited frequency $\omega = 0.357$ is of an unstable instability wave at $x = 50$. At $x = 130$, $\omega = 0.15$ is the frequency with maximum amplitude followed by 0.198. $\omega = 0.357$ is the third highest peak. At $x = 210$, the most dominant frequency in the spectra is still $\omega = 0.15$. $\omega = 0.357$ decays in zones 2 and 3. On the other hand the growth rates of other frequencies such as $\omega = 0.15$, 0.174 and 0.198 are much higher between $x = 130$ and $x = 210$. In the region where transition is taking place at $x > 210$, the frequency spectra is broadband. The unstable frequencies are marked by vertical dashed lines in figure 4.14.

The most dominant frequencies are not the same for cases tu001s and tu001l. If a wave with highest growth rate at a chosen station is to be the most dominant, one would expect to see the same dominant frequency in the spectra of cases tu001s and tu001l. But that is not the case. Due to higher low frequency content, free-stream disturbances penetrate further

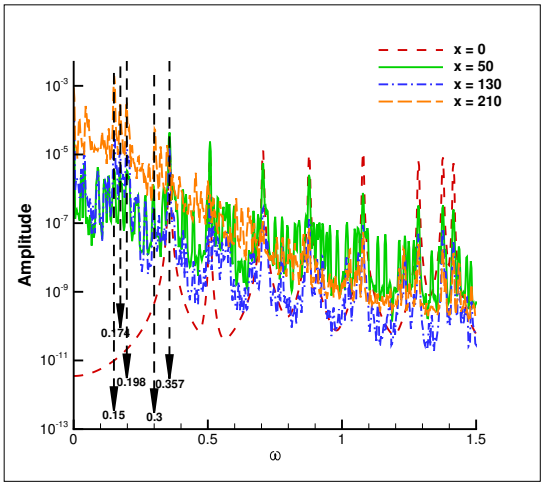

Figure 4.14: Frequency spectra of the u' component at specified streamwise locations for the case tu001l.

inside the boundary layer for case tu001l. This could result in distortion of the mean velocity profiles by the disturbances at inflow which could be different for cases tu001s and tu001l. In figure 4.15, wall normal profiles of mean streamwise velocity have been plotted at chosen streamwise locations for both tu001s and tu001l cases. There is apparently no difference in the profiles of the two cases. The dominant modes in the spectra at a chosen station are due the frequency content of the inlet even at such low perturbation levels. It is clear that initial amplitude of the unstable modes and the local growth rates decide the instability wave that dominate the flow.

In figure 4.16, unstable linear instability modes from solution of the OS equation have been shown for the time and span-averaged mean flow at indicated streamwise stations. The spatially unstable wavenumbers at a given station are shown in the right frame of figure 4.16 and their growth rates have been plotted as function of frequency in the left frame. Figure 4.16 helps in identifying the most unstable frequency at a given station. The most unstable frequency at $x = 50$ is very close to $\omega = 0.198$ marked in figure 4.14. $x = 50$ is in zone 1 shown in the contour plot in figure 4.13. The lowest frequency excited at inlet, $\omega = 0.357$ is also unstable. This mode was seen to have the maximum amplitude at $x = 50$ in figure 4.14 due to its much higher energy content at inlet. But $\omega = 0.357$ is stable at $x = 130$. As the flow develops downstream, the

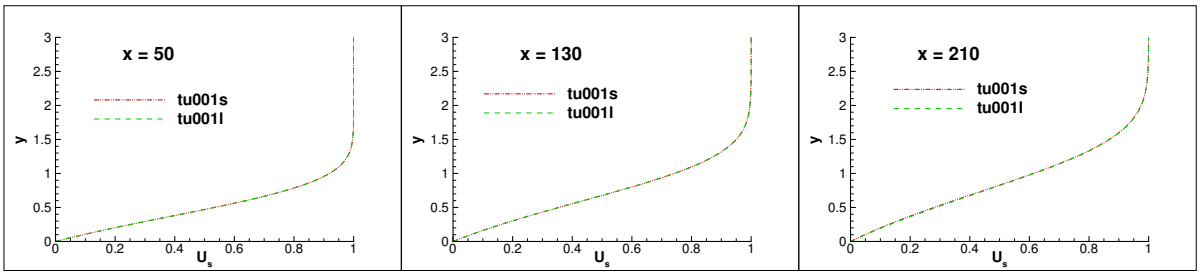

Figure 4.15: Comparison of mean flow velocity (U_s) profiles at indicated streamwise stations for the cases tu001s and tu001l.

frequency of the most unstable mode decreases. The most dominant frequency at $x = 210$ is $\omega = 0.15$ (figure 4.14). But this frequency is the most excited only around $x \sim 130$. Other frequencies such as $\omega = 0.174$ and 0.198 are also close to the most unstable mode. This justifies why these frequencies appear as prominent peaks in figure 4.14 at $x = 130$.

The unstable wavenumber at all streamwise stations collapse on to a single curve at low frequencies is evident from the right frame of figure 4.16. The unstable wavenumber corresponding to the most dominant modes at $x = 50$ and $x = 210$ are also marked. The wavelength predicted by the linear theory for the dominant mode $\omega = 0.357$ at $x = 50$ is $6.8\delta_0$ (for $k_r = 0.9242$ at $x = 50$). The average wavelength of disturbances from DNS around the same location is very close to this value at $6.9\delta_0$ (in zone 1). The linear stability predicted most dominant mode at $x = 210$ (zone 3) is $\omega = 0.15$. The LST predicted wavelength of the disturbance wave is $13.9\delta_0$. The average wavelength observed from DNS is around $13.6\delta_0$. This explains the difference in wavelengths of disturbances in zone 1 and zone 3 in figure 4.13.

In figure 4.17, the downstream evolution of $\hat{u'}$ and $\hat{v'}$ for the five frequencies marked in figure 4.14 have been plotted. Plot for the u' component in the left frame shows that all five modes initially grow up to $x \sim 50$. The initial growth is due to nonmodal growth of initially very small perturbations (Schmid and Henningson, 2001). It is followed by decay for $\omega = 0.3$ and 0.357. Modes with linearly unstable frequencies at $x = 50$, grow. $\omega = 0.357$ keeps decaying until transition process starts around $x \sim 210$. $\omega = 0.15$ grows the most to become the dominant frequency after $x \sim 130$, because this is close to being the most unstable frequency

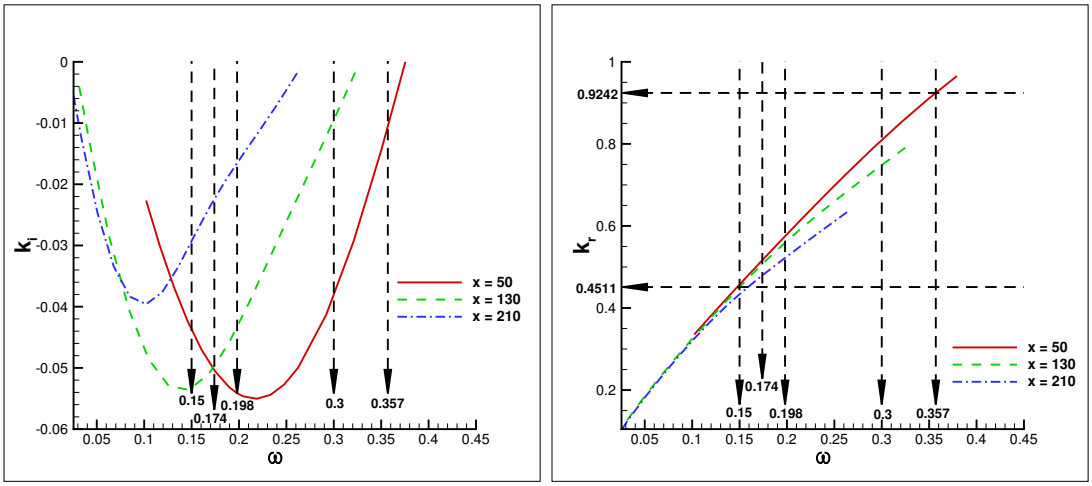

Figure 4.16: Left: Predictions of unstable frequencies by Linear Stability theory at indicated streamwise stations for the case tu001l. The frequency peaks marked in figure 4.14 are also shown. Right: Unstable wavenumbers (k_r) predicted by Linear Stability theory. The unstable wavenumber corresponding to most dominant frequency from DNS at $x = 50$ and 130 are also shown.

around $x \sim 50$ (figure 4.16). Also it remains most dominant up to the transition regime as it is excited at almost the highest growth rate at all stations before the perturbations become nonlinear. u' disturbances with $\omega = 0.174$ and 0.198 grow at a lower rate. Amplitude evolution of v' perturbations at these frequencies plotted in the right frame of figure 4.17 corroborates the same. It is interesting to note that $\omega = 0.198 \sim 0.357 - 0.15$. So disturbances at these frequencies might form a triad where the other two components would extract disturbance energy from the modes with $\omega = 0.357$ as the critical layers of the instability waves would be the same. Also, $\omega = 0.174$ is the subharmonic of $\omega = 0.357$. Therefore, subharmonic mode growth is also possible. Once the disturbances reach high amplitudes to become nonlinear, these modal interactions would be more active.

Figures 4.14, 4.16 and 4.17 and their comparison with tu001s case demonstrate the effect of inlet frequency spectra on the consequent instability. After the perturbation amplitudes become nonlinear, secondary instability is triggered. The inlet spectrum acts as a 'control knob' in deciding the dominant frequency prior to the instability waves becoming nonlinear. By controlling the inlet disturbance spectra, transition may be controlled in APG boundary

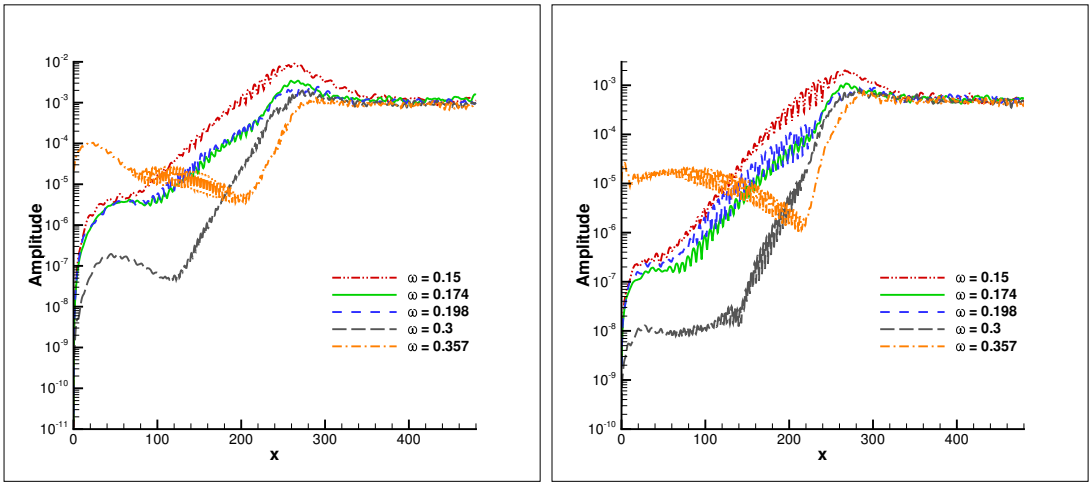

Figure 4.17: Left: Downstream growth of u' due to frequencies marked in figure 4.14. Right: Downstream growth of the same frequencies for v' component.

layers under very low disturbance conditions.

4.3.2.2 Secondary instability and transition

In figure 4.18, u'_{rms} and v'_{rms} have been plotted as a function of downstream distance x at a wall normal height $y = 0.7\delta_0$ for both $Tu = 0.1\%$ cases. The start and end of transition process have been marked by the vertical dashed lines. The amplitude of u'_{rms} first increases followed by decay. Then it monotonically increases until transition to turbulence is complete. The amplitude of u'_{rms} is higher for the case tu001l until $x \sim 60$. This is probably due to greater penetration of the low frequency components of the continuous spectra (Jacobs and Durbin, 1998). As mentioned earlier, the initial growth of u'_{rms} is due to nonmodal growth which does not affect v'_{rms} plotted in the right frame of figure 4.18. The amplitude of u'_{rms} is lower for the case tu001l between $x \sim 70$ and $x \sim 130$. These are the locations where vertical dashed lines are plotted marking the zones in figure 4.13. Most dominant mode changes from $\omega = 0.357$ to $\omega = 0.15$ for the case tu001l. This is due to low initial amplitude of the most excited mode for the case tu001l. Transition does not begin until $u'_{rms} \approx 1\%$. Before that the rms growth is linear. Transition is complete when u'_{rms} magnitude is $\sim 10\%$. Figure 4.18 shows that, depending on inlet disturbance spectra, the flows in two cases take very different

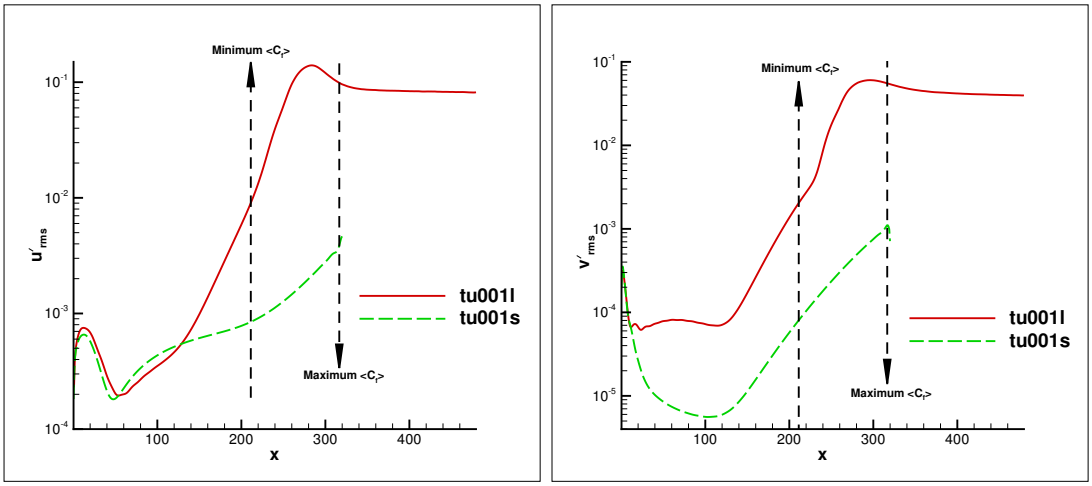

Figure 4.18: Left: u'_{rms} at a wall normal height $y = 0.7\delta_0$ plotted as a function of x for cases tu001s and tu001l. Right: v'_{rms} at a wall normal height $y = 0.7\delta_0$ plotted as a function of x for cases tu001s and tu001l. In both plots, region of transition to turbulence for the case tu001l has been marked by the vertical dashed lines.

transition routes. These instability routes are advanced or delayed enroute to transition but characteristically similar.

The plot for isosurfaces of Q-criteria color contoured by wall normal distance y in figure 4.19 is presented to show the vortical structures inside the transitional boundary layer. The contours of v' are also plotted at a wall normal plane $y = \delta_0$. Λ vortices form and break down from their tip to generate patches of turbulence. On occasions, these vortical structures start breaking down before being fully formed. Also, unlike Λ vortices generated by monochromatic forcing, these are often asymmetric, being tilted in one side or the other. The size of the Λ vortices vary between $9 - 15\delta_0$. The vortices generated in mixed mode transition cases in ZPG had an average size of $\sim 6\delta_0$. The present size is close to the spanwise size of Λ vortices predicted by Floquet stability theory for subharmonic transition in ZPG boundary layer by Herbert (1988). Nondimensional spanwise wavenumber $b \approx 0.68$ (Herbert, 1988) for a Λ vortex of size $12\delta_0$.

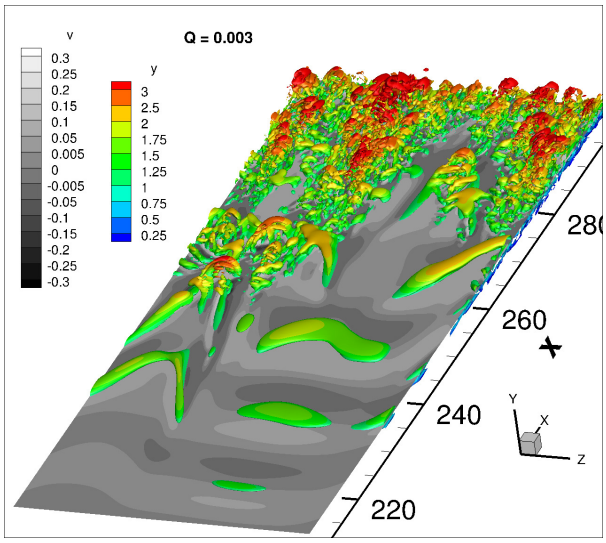

Figure 4.19: Formation and breakdown of Λ vortices depicted by isosurfaces of Q-criteria. The isosurfaces of $Q = 0.003$ are color contoured by distance from the wall. $-0.3 \leq v' \leq 0.3$ contours are also shown in a horizontal plane at a wall normal height $y = \delta_0$.

4.3.3 Case tu01

The lowest energetic disturbance frequency at inlet for the cases tu001s and tu01 are same as tabulated in table 4.1. Tu is an order of magnitude higher in the present case. Transition is earlier than case tu001l. It seems reasonable to conclude, that, with lower frequency disturbances at inlet could result in transition even more upstream.

In figure 4.20, contours of u' and v' have been plotted in a horizontal plane located at a wall normal height $y = 0.87\delta_0$. Wall normal peak of u'_{rms} is located at this wall normal height at the streamwise station with minimum $< C_f >$ indicating the initiation of transition. Streamwise long Klebanoff streaks are the main feature of u' contour plot in the top frame of figure 4.20. One can not identify instability waves. On the other hand, the instability waves are clearly identifiable in the v' contour plot in the bottom frame. These show up almost at the same streamwise station as the first appearance of these instability waves for the case tu001s. The instability waves arise (around $x \sim 140$) before transitional region. But their participation in transition is not so apparent.

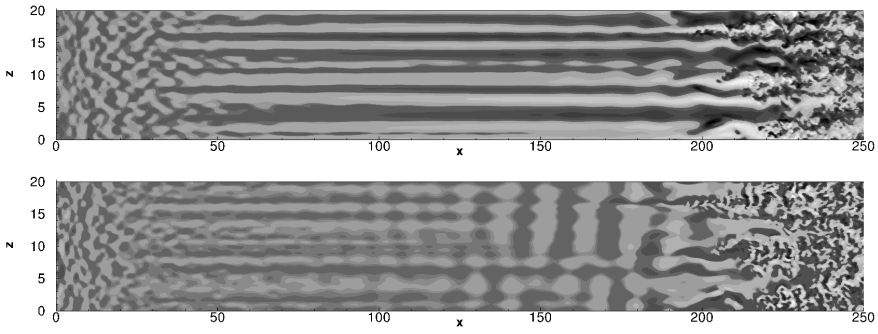

Figure 4.20: Instantaneous contours of $-0.3 \leq u' \leq 0.3$ (top frame) and $-0.2 \leq v' \leq 0.2$ (bottom frame) at a wall normal height $y = 0.87\delta_0$ for the case tu01. The wall normal peak of u'_{rms} is at $y = 0.87\delta_0$ at the transition onset where $< C_f >$ is minimum.

4.3.3.1 Role of instability waves

The frequency spectra computed at $x = 155$ is plotted in the left frame of figure 4.21 for both u' and v' components. This is the location where the instability waves may be identified in v' contour plot. The spectra is expectedly broadband. The vertical dashed lines mark the subharmonic and harmonic of the most dominant instability wave. The excited 2-D instability waves have frequency $\omega = 0.17$. This was also the dominant frequency of 2-D instability waves for the case tu001s (figure 4.10). As if, the spectral content of disturbances at inlet is the 'control knob'. In the right frame of figure 4.21, the wall normal profile of the mean streamwise velocity (U_s) has been plotted at $x = 155$ for the cases tu01 and tu001s. The high amplitude Klebanoff streaks significantly distort the velocity for the case tu01. The velocity profile for the case tu01 is fuller implying this to be more stable. But still the most dominant instability wave is same for the two cases. This demonstrates that the instability waves are very sensitive to the spectral disturbance content at inlet.

In figure 4.22, downstream growth of disturbances with dominant frequency $\omega = 0.17$ and it's subharmonic and harmonic frequencies marked in figure 4.21 have been shown by plotting the amplitude of these frequencies at each streamwise station. The Fast Fourier transformed amplitudes were averaged in span to compute the contribution of the 0 spanwise wavenumber. For both u' and v', growth of $\omega = 0.17$ is exponential after $x \sim 60$. Similar trend of growth was

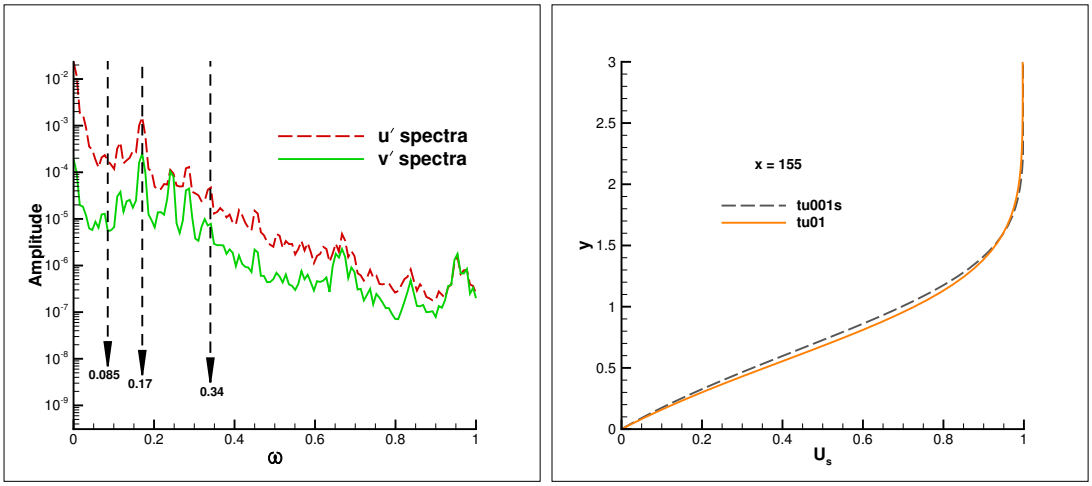

Figure 4.21: Left: Frequency spectra of u' and v' computed at $x = 155$. Right: Comparison of scaled mean flow velocity (U_s) profile at $x = 155$ for the cases tu01 and tu001s.

also obtained for the case tu001s. The amplitude of subharmonic and harmonic frequencies for v' is same in the transitional regime. The amplitude of $\omega = 0.17$ is an order of magnitude higher at the start of transition for v'. The amplitude of 2-D disturbances with $\omega = 0.17$ is highest of all the frequencies for u' in the transitional regime. The amplitude of instability waves with frequency $\omega = 0.17$ is higher than even the low frequency Klebanoff streaks. The instability waves participate in triggering transition, but, it is not clear, how.

Wall normal profiles of rms of perturbations in all three velocity components have been plotted in figure 4.23. The ordinate in this plot is the wall normal direction y scaled by local boundary layer thickness δ_{99} at the streamwise stations indicated. The peak values in wall normal profiles of u'_{rms} are located at $y/\delta_{99} = 0.45$. Therefore, the peak moves away from the wall as δ_{99} increases downstream. Consequently, peak value of v'_{rms} increases at each of these stations as well. At $x = 200$, the breakdown is already underway. There is no distinct peak in the profiles of v'_{rms} inside the boundary layer except for $x = 200$. Peak magnitude of w'_{rms} is higher than v'_{rms} at all stations. The peak magnitude of rms components is similar to bypass transition over compressor blade studied by Zaki et al. (2010) at higher Tu.

Downstream evolution of the wall normal maximum of u'_{rms} has been plotted for the APG case and compared with $Tu = 1\%$ case for ZPG in figure 4.24. Initially both APG and ZPG

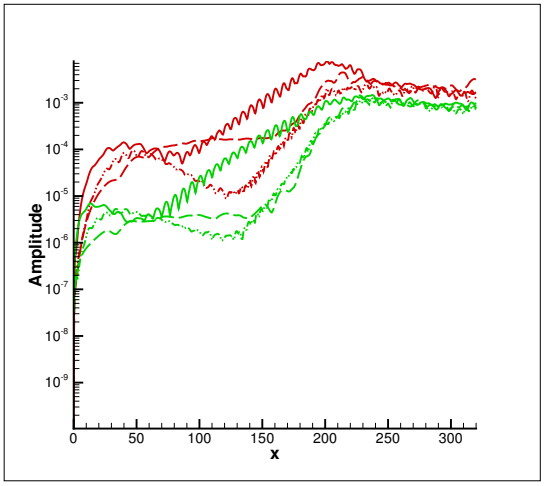

Figure 4.22: Downstream growth of u' (red) and v' (green) due to frequencies $\omega = 0.085$ (dashed), $\omega = 0.17$ (solid) and $\omega = 0.34$ (dash double dotted).

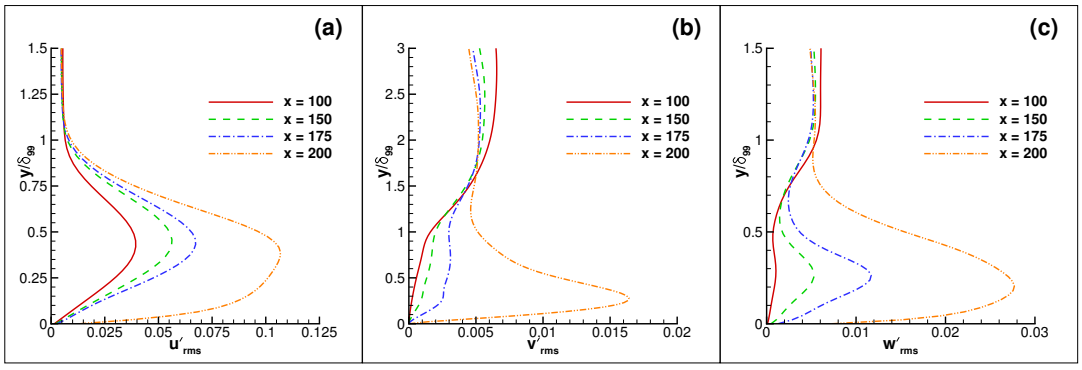

Figure 4.23: Wall normal profiles of *rms* perturbation velocities plotted at selected streamwise stations for the case tu01. The wall normal axis has been normalized by the local δ_{99}.

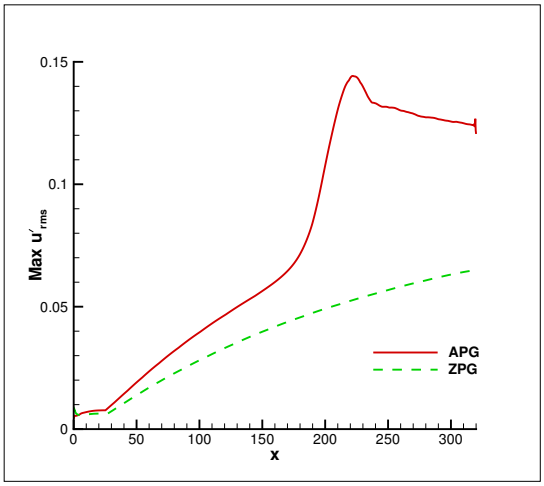

Figure 4.24: Maximum wall normal u'_{rms} plotted as a function of downstream distance x for the case tu01 and also for ZPG case. The transition onset for APG is around $x \sim 164$.

have similar magnitude of maximum of u'_{rms}. This is prior to generation of Klebanoff streaks, when, the maximum in u'_{rms} is at the edge or outside the boundary layer. After around $x = 30$, the APG has higher magnitude of u'_{rms}. In the contour plots in figure 4.20, the Klebanoff streaks are identifiable from this location. The higher magnitude of u'_{rms} for APG may be attributed to two factors, the higher coupling of free-stream disturbances in APG (Zaki and Durbin, 2006) and the higher growth rate of spontaneously excited instability waves in APG. The effect of higher coupling is less apparent and probably less significant. The coupling coefficients were only significantly high at even higher adverse pressure gradient levels compared to present case ($\beta = -0.18$) in Zaki and Durbin (2006). The discrete modes on the other hand grows quickly in APG. It is already noted from FFT of perturbation components that the dominant instability wave corresponding to $\omega = 0.17$ has the highest amplitude of all the frequencies in the transitional regime. Transition inception is around $x \sim 163$, where, the peak of $u'_{rms} = 0.061$. At the same streamwise location, the peak rms for ZPG is 0.042. The difference is not large. This implies that the nature of disturbances are important in transition onset: instability waves play a key role.

In the left frame of figure 4.25, contours of amplitude of time averaged spanwise wavenumber spectra for u' inside the boundary layer has been plotted in $x - k_0$ plane. Here, $k_0 = k_z \frac{l_z}{2\pi}$,

where, k_z is the spanwise wavenumber and l_z is the width of the computational domain. The transition onset is marked by the vertical dashed line. The wavenumber spectra is plotted in a wall normal plane, where, u'_{rms} has its peak at the location of transition onset. The horizontal dashed line indicates the value of k_0 that corresponds to a wavelength of twice the boundary layer thickness (δ_{99}) at transition onset. Prior to transition onset, spanwise spectra is band limited. The spectral band becomes wider after transition is triggered. At around $x \sim 100$ two distinct peaks appear in the k_0 spectra. The lower peak is due to the streaks with spanwise spacing equal to local boundary layer thickness which collapses well onto the horizontal dashed line. This peak corresponds to $k_z\delta_0 \sim 1.59$ which is fairly close to the width of disturbances predicted by Butler and Farrell (1992) that undergo maximum shear amplification. The higher peak is for $k_0 = 7$ which arises due to nonlinear interaction of streaks ($k_0 \sim 5$) with large scale vortices with $k_0 = 2$. This corresponds to vortices with size of half of the domain width ($k_0 = 7$ corresponds to $k_z \sim 2.2$). Higher wavenumbers due to nonlinear interactions are also significant in final stages of transition.

In the right frame of figure 4.25, the spanwise wavenumber spectra of u' and v' has been plotted at two streamwise stations, at $x = 150$ (this is prior to transition onset) and $x = 170$ (after transition onset). These are plotted at the same wall normal height as the contour plot in the left frame. In the wavenumber spectra of u', three distinct peaks are identifiable at both stations, $k_0 = 2, 5$ and 7. The peak corresponding to $k_0 = 5$ is due to the streaks with spanwise width of boundary layer thickness. The peak at $k_0 = 2$ is not present in the spectra for v', is probably due to shear amplification of disturbances with $\omega \sim 0$ generated inside boundary layer as a response to free-stream disturbances with large spanwise size (this corresponds to vortical disturbances of width half of the size of the spanwise domain) that undergoes very slow viscous damping. Higher wavenumbers, due to nonlinear interaction, or their higher harmonics such as $k_0 = 12, 14, 17, 19$ also grow. The spanwise spectra of both u' and v' shows that the growth rate of purely 2-D component ($k_0 = 0$) is highest between these two streamwise stations. Also for v' component, the amplitude of 2-D disturbances is highest at both stations indicating that the disturbances are due to exponentially growing 2-D disturbances. As the u' component is dominated by streaky disturbances, it is harder to identify the contribution of 2-D instability

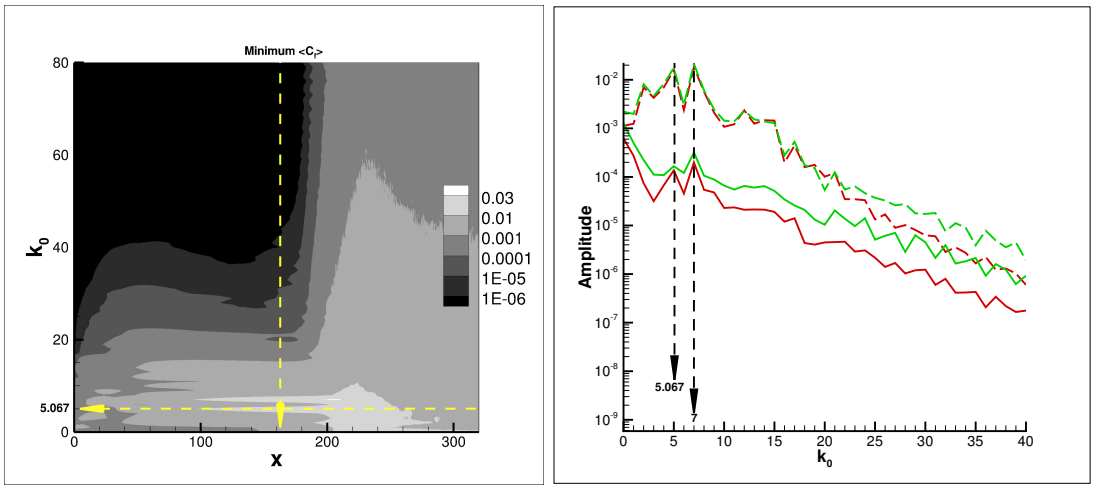

Figure 4.25: Left: Spanwise wavenumber spectra of u' plotted versus downstream distance x for the case tu01. Here, $k_0 = k_z \frac{l_z}{2\pi}$. The horizontal dashed line marks the k_0 value corresponding to streak size of δ_{99} at the location of onset of transition. Right: Spanwise spectra of u' (dashed) and v' (solid) components at locations $x = 150$ (red) and $x = 170$ (green).

waves. Figure 4.25 again emphasizes the role of instability waves in transition at moderate $Tu \sim 1\%$ in APG boundary layers. It must be mentioned here that the 2-D disturbances had been excluded from the inlet disturbance spectrum. These arise due to nonlinear interaction downstream of inlet.

4.3.3.2 Breakdown via helical mode

Breakdown to turbulence for the case tu01 is via the helical structures (Bose and Durbin, 2016a). Helical features are seen in both cases tu01 and tu02, but more frequently identifiable for the case tu01. In figure 4.26(a), an emergent helical $n = 1$ mode is shown by isosurfaces of $u' = -0.15$. The helical structure is fully formed in figure 4.26(b). It develops on a negative streak, in the high shear region between adjacent positive and negative streaks, as is shown in figure 4.26(c). Figure 4.26(d) shows u' contours in the $x - y$ plane passing through the overlap region of these positive and negative streaks. The negative contours are dark. That the helical mode develops close to the wall is indicated by the dashed line marking $\delta_{99}(x)$. Hack and Zaki (2014) found that inner modes develop in similar high shear regions. Contour plots of

perturbation velocities in $x-y$ planes passing through the high shear region between positive and negative streaks have the appearance of Kelvin Helmholtz instability waves, as in free-shear flows. The overlapping surfaces are, of course, 3-dimensional and much more intricate. The 3-D appearance is of a helical structure, being generated in the high shear between a pair of complicated, 3-D, overlapping layers (Brandt and de Lange, 2008).

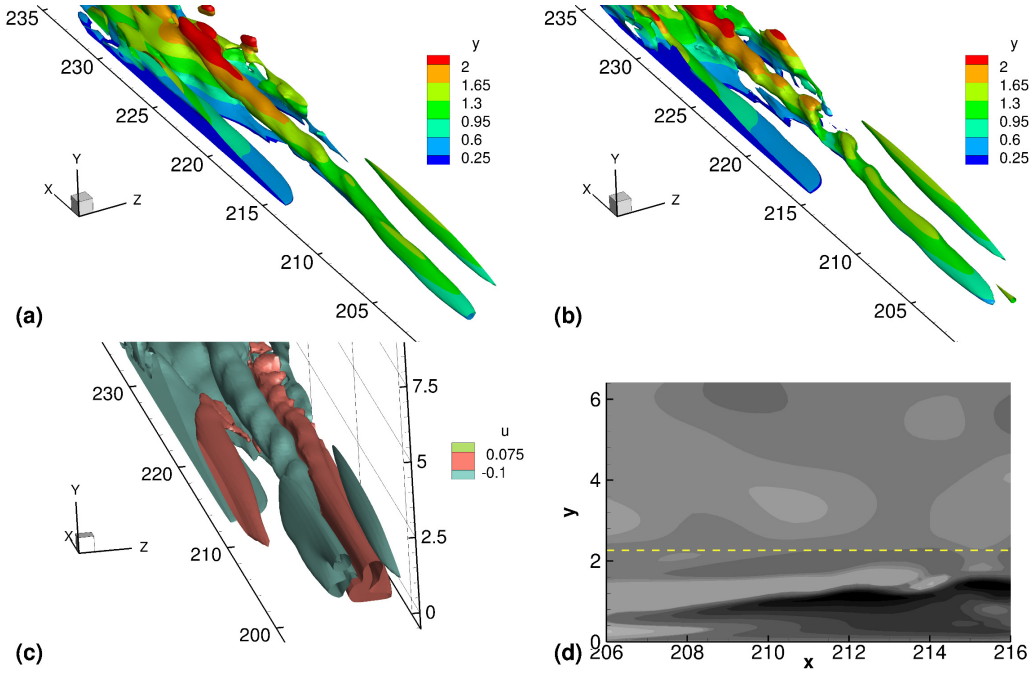

Figure 4.26: (a) Isosurfaces of $u' = -0.15$ colored contoured by wall distance y for the case tu01 depicting a precursor to helical mode. (b) Helical structure prior to turbulent spot formation. (c) Isosurfaces of u' showing the high shear region between high and low-speed streaks at the same instant as (a). (d) $-0.3 \leq u' \leq 0.3$ contours in wall normal $x-y$ plane cutting through the spot precursor in (a). The boundary layer thickness at $x = 215$ is $\delta_{99} = 2.26\delta_0$. The figure is from Bose and Durbin (2016a).

The streaks are jet-like, streamwise perturbations; these may be termed the primary perturbations. The helices are flow structures observed in u' isosurfaces. Therefore, these may be termed secondary perturbations. Decomposition of the instantaneous streamwise vorticity component (ω_x) in the following manner helps identify these secondary perturbations (Hack and Zaki, 2014):

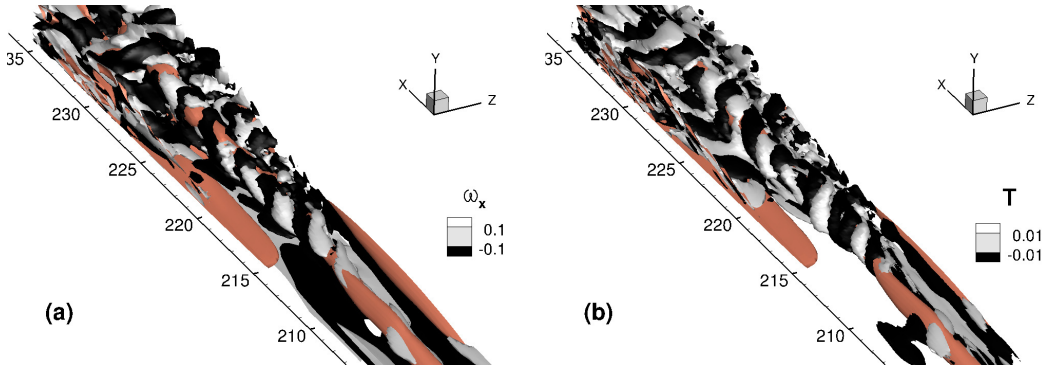

Figure 4.27: (a) Isosurfaces of $u' = -0.15$ (red) for the helical structure shown in figure 4.26(b). Isosurfaces of streamwise vorticity are also shown for $\omega_x = \pm 0.1$. (b) Isosurfaces of streamwise vorticity tilting term $T = \pm 0.01$ at the same instant as (a).

$$\omega_x = \bar{\omega}_x + \omega_x^p + \omega_x^s.$$

Here, $\bar{\omega}_x = 0$ for the mean flow. $\omega_x^p \approx 0$, as the streaks are primarily in u'. Therefore $\omega_x \approx \omega_x^s$, where ω_x^s denotes the streamwise vorticity due to secondary perturbations. Isosurfaces of ω_x for a pair of positive and negative values have been plotted in figure 4.27(a), at the same instant as in figure 4.26(b), along with the isosurfaces of $u' = -0.15$ depicting the helical structure. Prior to formation of the helical structure, isosurfaces of ω_x wrap around the unstable streak. Initially ω_x due to primary instability is weak and grows stronger with formation of the helical structure. After genesis of the helical structure, the isosurfaces of ω_x also orient in an approximately helical pattern. For $x > 215$, troughs and crests in ω_x become apparent along the helical structure. The isosurfaces of ω_x wrap around the isosurfaces of u'.

In the transport equation for ω_x, the tilting term is $T = \omega_y \frac{\partial U}{\partial y} + \omega_z \frac{\partial U}{\partial z}$. (As, initially ω_x is weak and the streamwise gradient of U is small, the tilting term is larger than the stretching term.) In figure 4.27(b), instantaneous isosurfaces of $T = \pm 0.01$ have been plotted. Clearly, the isosurfaces are very nicely correlated with the helical structure, indicating that the secondary perturbations are of vortical nature. The positive component wraps around the negative part of u' and maintains a phase difference of π in the azimuthal direction with the negative component, in a given plane.

4.3.4 Case tu02

The effect of higher intensity free-stream disturbances on boundary layer transition is also investigated. $Tu = 2\%$ intensity free-stream turbulence is prescribed as inlet disturbance. As shown in table 4.1, the lowest nonzero inlet frequency is same for cases tu001s, tu01 and tu02. The higher amplitude free-stream disturbances instigate high amplitude Klebanoff streaks as boundary layer response. Consequently, transition is earlier for the case tu02 (also seen from C_f plots in figure 4.5).

Instantaneous u' and v' perturbation velocity components have been plotted in figure 4.28 in a horizontal $x - z$ plane. This plane is at a wall normal height where local peak of u'_{rms} is obtained at the streamwise location of transition onset. Streamwise long Klebanoff streaks smoothly continues into the transitional regime in the u' contour plot in the top frame where these appear to breakdown. The v' contour plot in bottom frame also depict the signature of the Klebanoff streaks indicating that the lift-up effect is significant from inlet onwards. The instability waves, clearly identifiable in the v' contour plots for all of the earlier discussed cases, is not so clear for this case. Locally 2-D patches are recognizable from $x \sim 130$ onward. But the instability waves are not too obvious.

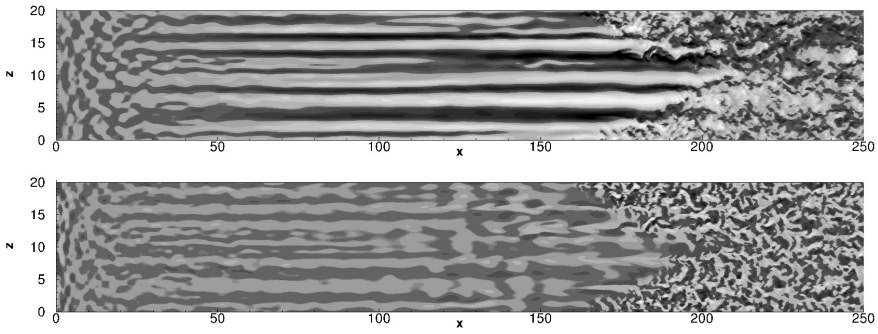

Figure 4.28: Instantaneous contours of $-0.3 \leq u' \leq 0.3$ (top frame) and $-0.2 \leq v' \leq 0.2$ (bottom frame) at a wall normal height $y = 0.75\delta_0$ for the case tu02. The wall normal peak of u'_{rms} is at $y = 0.75\delta_0$ at the location of transition onset where $< C_f >$ is minimum.

In figure 4.29, the wall normal profiles of *rms* of perturbation velocity components have been plotted at indicated streamwise stations upstream of transition. The ordinate in this plot

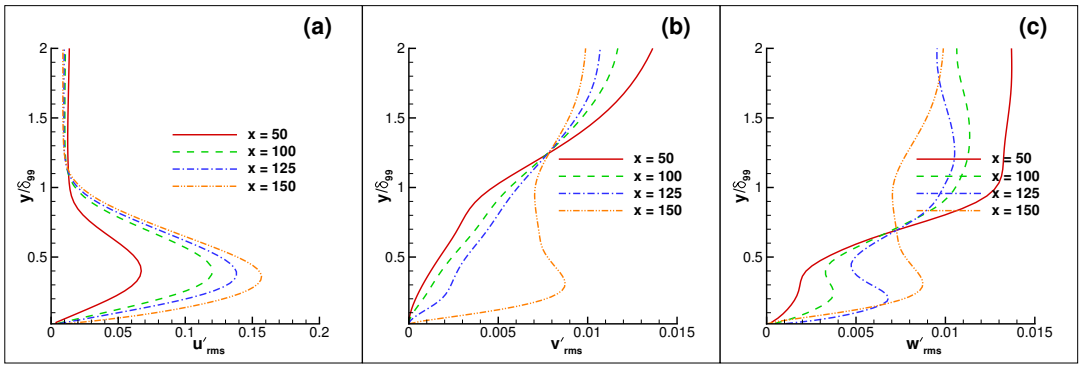

Figure 4.29: Wall normal profiles of rms perturbation velocities plotted at selected streamwise stations for the case tu02. The wall normal axis has been normalized by the local δ_{99}.

is the wall normal distance y scaled by the local 99% boundary layer thickness. The peak of u'_{rms} is located around $y/\delta_{99} \sim 0.4$ at all stations considered. The peak location for u'_{rms} is closer to the wall compared to the case tu01. The wall normal peak in the profiles of v'_{rms} is only prominent in the transitional regime. A peak in the profile of w'_{rms} at $x = 50$ appears close to the wall. Downstream, this peak moves away from the wall. The v'_{rms} and w'_{rms} peak locations at these stations are not the same as the peak locations for u'_{rms}. The peak of v'_{rms} and w'_{rms} at $x = 150$ are located at a wall normal height $y/\delta_{99} \sim 0.3$.

The peak value of u'_{rms} for the case tu02 (about 0.15 in transitional regime) is higher than that for the case tu01 (the peak at $x = 200$ is around 0.1) in the transitional regime. This could be due to higher magnitude of streaks caused by higher amplitude ambient disturbances. But it is to be noted that the peak values of v'_{rms} and w'_{rms} are lower for the case tu02 in the transitional regime. This implies that the wall normal and spanwise fluctuating components have lower contribution in generation of turbulence in the transitional regime. Also the rms peak value is almost an order of magnitude higher for the u' compared to v' and w' components for the case tu02. The fact that most of the fluctuations are generated in u' component indicates a more active role of Klebanoff streaks in the transition process. In the case tu01 on the other hand, all the perturbation components have contribution of same order of magnitude even in the final stages of transition. Therefore, it appears that transition in case tu01 is mixed mode type while for the case tu02 is predominantly bypass transition.

Frequency spectra of u' and v' components have been plotted in the transitional regime in figure 4.30. The FFT of the perturbation velocity components have been plotted at the wall normal height corresponding to local peak in u'_{rms} at the streamwise location where $< C_f >$ is minimum. To identify the contribution of the 2-D instability waves, frequency spectra of spanwise invariant perturbations ($k_z = 0$ spanwise wavenumber component) have also been shown in both plots. The frequency spectra is well distributed due to nonlinear interaction of high amplitude primary disturbances. The amplitude is highest for disturbances with frequency $\omega \sim 0$. These are due to very low frequency Klebanoff distortions. The contribution of the 2-D disturbances is almost an order of magnitude smaller than the spanwise localized disturbances for the u' component up to $\omega \sim 0.6$. Inlet disturbance with lowest frequency (tabulated in table 4.1) is 0.636. The frequency spectra for v' shown in the right frame of figure 4.30 shows that the most unstable disturbances lie within the frequency range of linearly unstable modes. In fact, 2-D disturbances with linearly unstable frequencies have higher amplitudes than the wall normal disturbances due to very low frequency Klebanoff streaks. The most unstable mode is with frequency $\omega = 0.17$. This is same as cases tu001s and tu01 which again emphasizes the importance of spectral content of inlet disturbances. 2-D linearly unstable disturbances contribute almost fully towards magnitude of the spanwise localized v' disturbances. Even at this high level of free-stream forcing, instability waves contribute significantly toward destabilizing the boundary layer .

Time averaged spanwise wavenumber spectra of u' has been plotted in the $x-k_0$ plane in the left frame of figure 4.31, similar to figure 4.25 for the case tu01. The transition onset location is marked. The horizontal dashed line is for $k_0 = 5.25$ corresponding to half wavelength equated to the local δ_{99} at the location of onset of transition. Peak clearly appears around this k_0 from $x = 40$ onwards. This is due to the Klebanoff streaks. Another peak at $k_0 = 7$ also appears. This could be due to nonlinear interaction of $k_0 = 5$ and $k_0 = 2$. After start of transition process, the spectra diverges. Very high magnitude of the peak corresponding to $k_0 \sim 5$ in the transitional regime indicates that the secondary instability involves the Klebanoff streak. The spanwise wavenumber spectra at $x = 130$ has been shown in the right frame of figure 4.31. The peaks at $k_0 = 5$ and 7 have higher magnitude compared to other wavenumbers. $k_0 = 2$

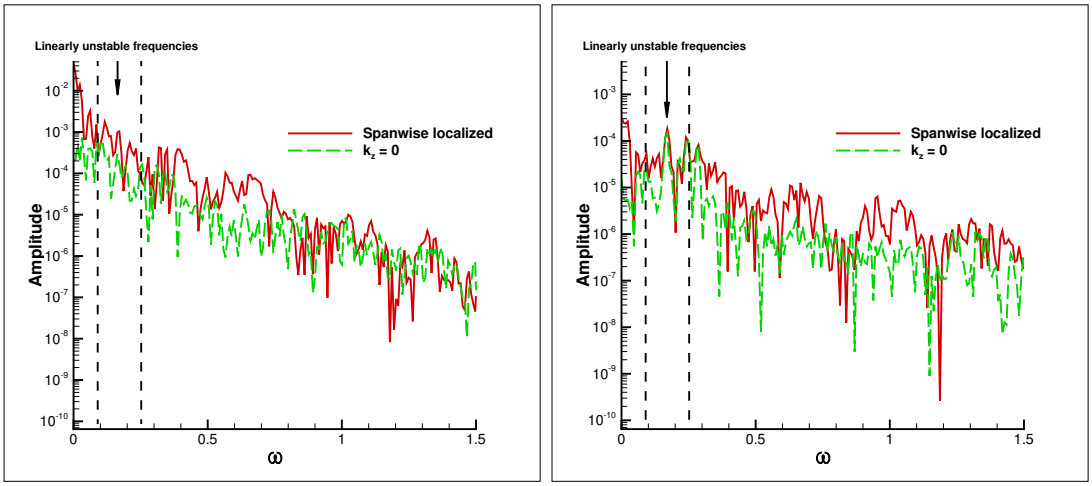

Figure 4.30: Left: Frequency spectra of u' computed at $x = 130$ at the wall normal location of maximum u'_{rms} at transition onset station. Right: Frequency spectra of v' computed at $x = 130$ at the same location. Spectra for both spanwise localized and $k_z = 0$ wavenumber have been shown. Linearly unstable frequency range at the selected station has been marked by vertical dashed line.

also has high magnitude for u', but does not appear as a distinct peak for v'. The nonlinear interaction between these three spanwise wavenumber components and the same among the offspring components is evident from the other distinguishable peaks in the plot for u'. The $k_0 = 0$ is a significant peak in v' only indicating that the instability waves are still significant for v'.

Local maximum of u'_{rms} has been plotted against downstream distance in figure 4.32 and compared to the $Tu = 2\%$ case in ZPG. Unlike the case tu01 (similar figure plotted in figure 4.24), downstream evolution of peak u'_{rms} is not linear prior to transitional regime indicating strong nonlinear interactions. The frequency spectra plotted in figure 4.30 also indicated the same. Transition inception in the ZPG case is initiated very close to outflow. At the location of transition inception for APG at $x \approx 109.375$, the peak u'_{rms} has a value 0.1275. At this same streamwise station the peak for ZPG is 0.091. It is important to note that the flow does not transition in ZPG even when the peak rms is as high as 0.15. This indicates that the transition mechanism is different among zero and adverse pressure gradients. Even though rms computation masks the effect of instantaneously high amplitude streaks, the comparison

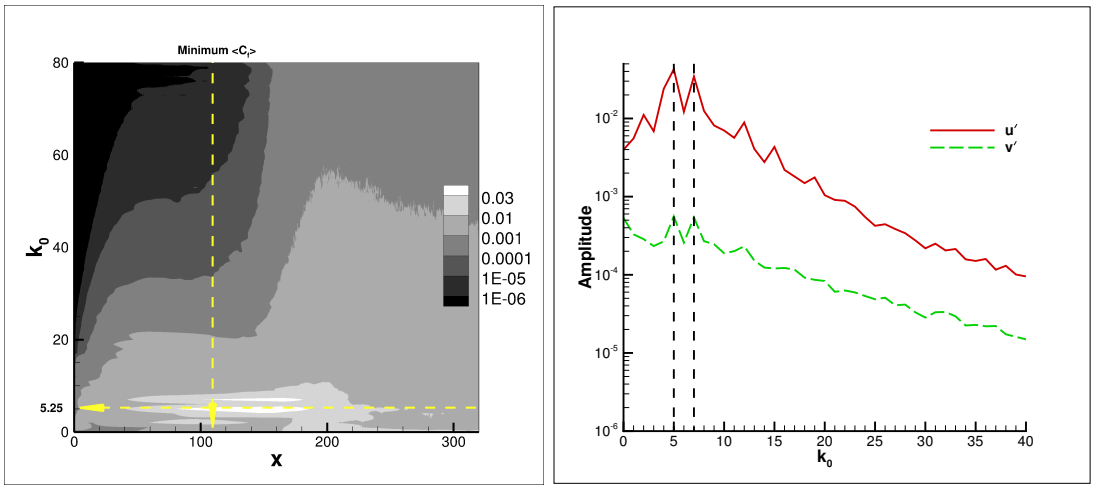

Figure 4.31: Left: Spanwise wavenumber spectra of u' plotted versus downstream distance x for the case tu02. Here, $k_0 = k_z \frac{l_z}{2\pi}$. The horizontal dashed line marks the k_0 value corresponding to streak size of δ_{99} at the location of onset of transition. Right: Spanwise spectra of u' and v' components at $x = 130$.

of locally maximum u'_{rms} shows that instantaneous streaks that breakdown in APG have comparatively lower magnitude. Instantaneous streaks are much more stable at large magnitudes in ZPG. Streak magnitude at the point of breakdown could be as high as $u' \approx 30\% U_\infty$ in ZPG (Hack and Zaki, 2014).

4.3.4.1 Breakdown via inner and outer modes: Bypass transition

Transition beneath high intensity free-stream turbulence in favorable, zero and moderately adverse pressure gradients is well documented. The dominant mode is outer sinuous secondary instability that break down to form turbulent spots. Comparatively, bypass transition in APG boundary layers is less explored. It is generally agreed that the spot inception in APG is most frequently via inner secondary instabilities (Brandt and de Lange, 2008; Vaughan and Zaki, 2011). But the exact reason in the shift in critical layer from outer to inner is not known yet. Most of the breakdowns seen for the case tu01 were through inner modes. Outer modes were entirely absent. For the case tu02 though, a few instances of outer sinuous mode breakdown were seen. Most of the breakdowns were again via inner mode. This qualitatively imply

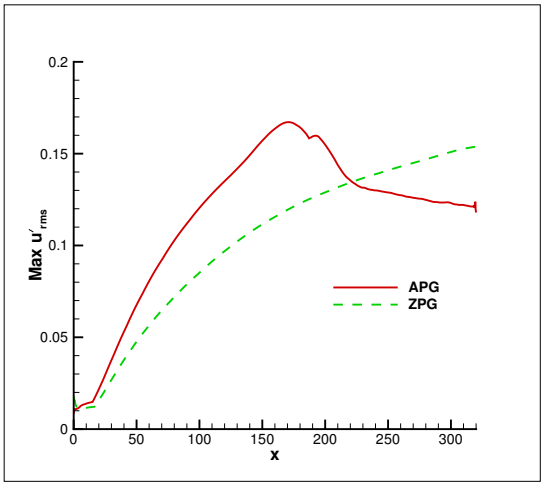

Figure 4.32: Maximum wall normal u'_{rms} plotted as a function of downstream distance x for the case tu02 and also for ZPG case. The transition onset for APG is around $x \sim 109$.

that outer modes are the result of streak instabilities. On the other hand, inner modes are not directly related to sensitive high amplitude streaks (figure 4.32) and consequent small amplitude secondary perturbations that grow over these. Here, these are perceived as interaction of linear or nonlinear instability waves and Klebanoff streaks.

A inner helical breakdown in the case tu02 has been shown in figure 4.33. These breakdowns are less clearly identifiable at high $Tu \sim 2\%$. The critical layer of these instabilities lie well inside the boundary layer (approximately $y/\delta_{99} \sim 0.4$) and their phase speed is around $\frac{1}{2}U_\infty$. The wavelength of these instabilities are much shorter (1–1.3δ_{99}) than the very large wavelength Klebanoff streaks ($k_x \sim 0$). These develop at the overlap region of low and high speed streaks, is shown in figure 4.33(b), which makes it even harder to identify in an ambience of high amplitude streaks. Nonetheless, there is evidence that these could trigger transition at even high Tu (Nagarajan et al., 2007; Brinkerhoff and Yaras, 2015). The instigator seems to be the enhanced wall normal shear at the overlap region of the streaks. It should be also noted though that these develop on streaks characteristically shorter than long Klebanoff streaks.

In the top frame of figure 4.34, isosurfaces of u' have been plotted for selected values to visualize breakdown of streaks to turbulent spots at an instant. At this instance two inner mode breakdowns are underway. At the same time an outer sinuous mode developing prior to

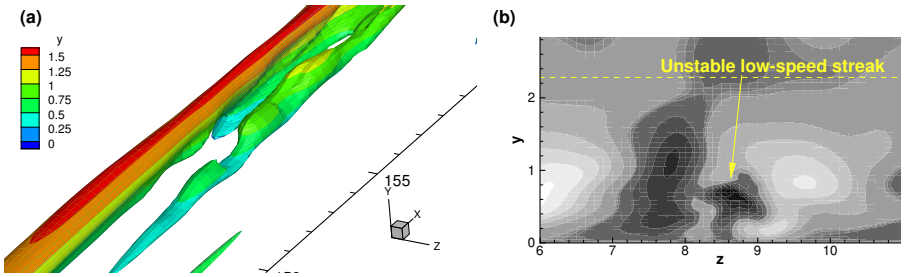

Figure 4.33: (a) Isosurfaces of $u' = -0.085$ color contoured by wall distance y for the case tu02 depicting a helical structure prior to turbulent spot formation. (b) $-0.25 \leq u' \leq 0.25$ contours in wall normal $y-z$ plane at $x = 155$. The boundary layer thickness at $x = 155$ is $\delta_{99} = 2.28\delta_0$. The figure is from Bose and Durbin (2016a).

breakdown can be seen. These have been enclosed by the dotted boxes. In the bottom frame of figure 4.34, the isosurfaces have been color contoured by wall normal distance y to qualitatively identify the wall normal location of the streaks. That the outer mode grows on low-speed streak is evident. On the other hand, inner breakdowns take place on streaks closer to the wall, become clear from the bottom frame. The inner mode breakdown is abrupt, without any clear precursor, while for outer mode, one can identify the spanwise modulation of the streaks more upstream of breakdown.

In the frequency spectra plots in figure 4.30, it was observed that the instability waves are detectable in the transitional regime, specially in v'. Moreover, most of the contribution in the spanwise localized spectra came from the 2-D instability waves. The frequency of these instability waves matches with those in lower Tu cases which had the same inlet disturbance wave vectors with different magnitude. The instability waves affect the transition process even at high Tu. It should be pointed out that the linear inner modes became TS waves when the streak amplitude was reduced to zero in the work on streak instabilities by Vaughan and Zaki (2011). In a streaky boundary layer, the discrete instability waves are the inner modes. If the current hypothesis that instability wave – Klebanoff streak interaction triggers secondary instability is true, then it also helps in explaining the appearance of inner *varicose* modes in APG. Spanwise invariant 2-D instability wave superimposed on a streak would indeed trigger a symmetric instability with spanwise fundamental wavenumber governing the secondary

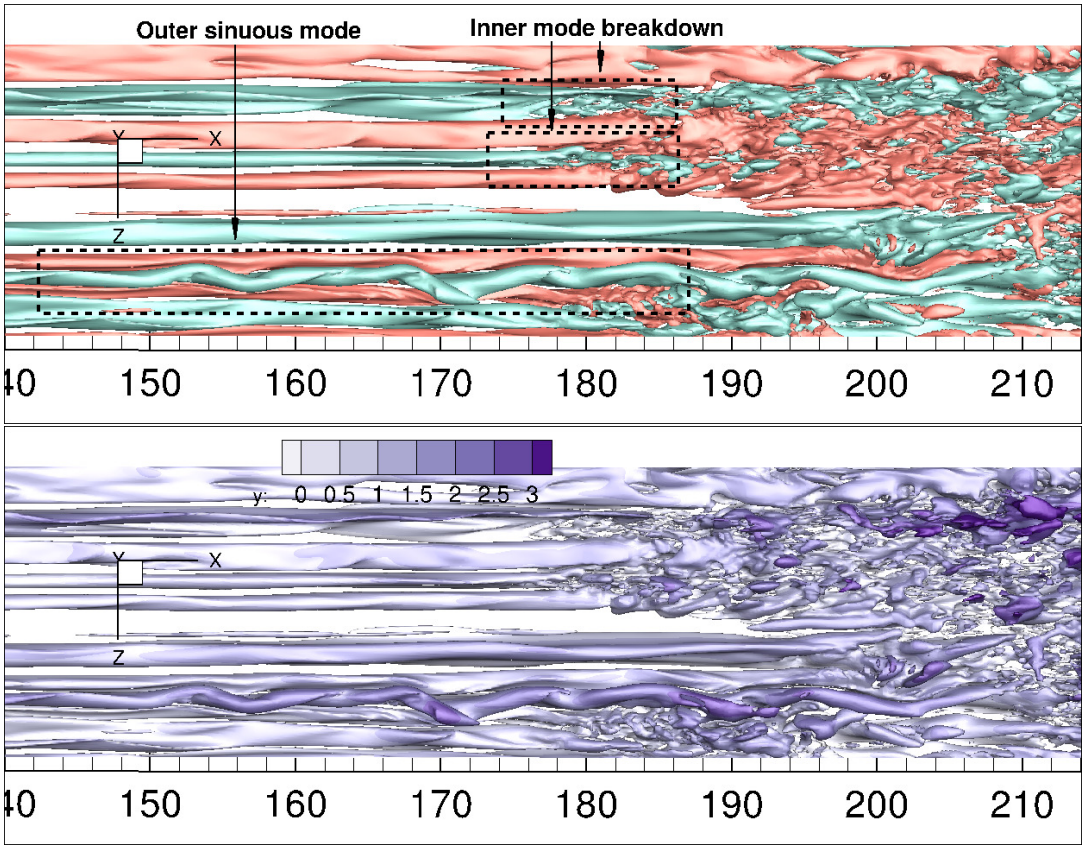

Figure 4.34: Top: Instantaneous isosurfaces of $u' = 0.1$ (red) and $u' = -0.1$ (green) depicting inner mode breakdown and outer sinuous mode spot precursor for the case tu02. Bottom: Isosurfaces of $u' = \pm 0.1$ color contoured by the wall normal distance y. Boundary layer thickness at $x = 155$ is $\delta_{99} = 2.28\delta_0$.

perturbations (Cossu and Brandt, 2004).

The outer mode breakdowns are more frequent at high Tu. There could be two reasons. One point is that higher amplitude Klebanoff streaks are prone to high frequency forcing from free-stream making these more conducive for growth of secondary perturbations. The other reason is an indirect role of the Klebanoff streaks in decreasing the propensity of appearance of inner modes. The streaks distort the boundary layer. The inflectional base APG profile becomes fuller due to favorable distortion by the Klebanoff streaks (Cossu and Brandt, 2002). The stabilization of base profile is more significant by higher amplitude Klebanoff streaks. That decreases the growth rate of instability waves over more stable mean base profile. Consequence is the reduced appearance of inner modes. Perhaps this is the reason why almost all breakdown scenarios in the present tu01 simulation are via inner modes. Other bypass simulations in APG under high intensity free-stream turbulence, for example, by Nagarajan et al. (2007); Hack and Zaki (2014) and Brinkerhoff and Yaras (2015) observed more frequent outer mode breakdowns. Same is the case here for tu02. The reason for a shift in critical layer therefore is not an inflectional base profile, rather, the role of instability waves in destabilizing Klebanoff streaks or the Klebanoff streaks indirectly affecting the proclivity of the base profile toward inner mode breakdown.

4.4 Conclusion

Transition to turbulence in APG boundary layers have been investigated. The base flow is obtained by diverging the upper boundary of the computational domain, where, impermeability and free-slip boundary conditions are imposed. Downstream of the inlet, base flow velocity profile matches very well with the Falkner Skan solution for desired Hartree parameter ($\beta = -0.14$). When the base flow computations are carried out over a sufficiently long domain, 2-D TS waves appear spontaneously inside the boundary layer. Such instability waves were also obtained in experiments of APG boundary layers under controlled conditions ($Tu \sim 0.3\%$) (Walker and Gostelow, 1989; Gostelow et al., 1994). In the simulation, these are instigated by the numerical noise. The TS wave properties match very well with the predictions of the linear stability theory. In APG boundary layers, which are highly sensitive to such infinitesimal

disturbances, spectral content is as important as the amplitude of disturbances in deciding the instability and transition route.

When the boundary layer is perturbed by free-stream turbulence, these instability waves appear further upstream. The inlet spectrum does not contain disturbances with similar wavenumber-frequency combination as the instability waves. The exact reason of the excitation of these waves from free-stream disturbances remain unknown. The nonlinear excitation of the linearly unstable frequencies and corresponding wavelength transformation of the free-stream disturbances to excite the instability waves is truly intriguing. Perhaps a perturbation evolution formulation in a nonlinear framework is necessary including nonparallel flow effects.

Beneath very low intensity free-stream turbulence ($Tu = 0.1\%$), the flow undergoes natural transition to turbulence. Instability waves trigger transition almost as quickly as bypass transition in APG boundary layers. Current simulations in that sense validate the experimental findings of Gostelow et al. (1994). Once the instability waves are instigated inside the boundary layer, locally most unstable modes grow, yet, the most dominant instability mode could be different depending upon the spectral content of the inlet disturbances and their local growth rates. Depending on these factors, the most dominant mode might change as the flow evolves downstream as is seen in the case tu001l. The locally unstable waves grow quickly and fill up the disturbance spectrum. The spectrum prior to development of secondary instability is therefore broadband. Considerably different instability routes are undertaken by the flow for cases tu001s and tu001l depending on the spectral content of the inlet disturbances, even though, the free-stream forcing magnitude is the same. The breakdown is via secondary instability of the TS waves. These simulations show that natural transition in APG boundary layers is likely to be due to formation and breakdown of Λ vortices in irregular pattern. H or K type secondary instability is unlikely in APG other than forcing the subharmonic or fundamental secondary perturbations under controlled conditions. This may be attributed to the very high local growth rate of the instability waves.

When the free-stream forcing is higher, about $Tu = 1\%$ (case tu01), on the basis of available evidence, instability waves participate in the transition process. In the perturbation velocity contour plots, these instability waves are clearly recognizable. The Klebanoff streaks are

prevalent in streamwise perturbations, but instability waves are manifested in the wall normal perturbation. The 2-D dominant instability wave frequency has the highest magnitude in the transitional regime. The spanwise wavenumber spectra of u' indicates Klebanoff streaks with spanwise spacing equal to the local boundary layer thickness. But $k_0 = 0$ has the highest magnitude for spanwise wavenumber spectra of v', highlighting the role of the instability waves. Breakdown is via formation of helical structures (Bose and Durbin, 2016a). These are inner instabilities which breakdown quickly to trigger transition. The trigger seems to be the interaction between Klebanoff streaks and the instability waves. In such breakdowns, streak magnitude is not as high as outer modes, rather, the instability grows in the high shear region between a low and a high speed streak.

Apparently, the instability waves are relevant in transition even at high $Tu \sim 2\%$ (case tu02). The instability waves are not clearly identifiable in the perturbations velocity field, even in v'. The local u'_{rms} profiles have peak magnitude an order of magnitude higher than v'_{rms} and w'_{rms}. The Klebanoff streaks are dominant in the transitional regime. The frequency spectra of the v' indicates a significant contribution by the 2-D instability waves. Comparing the maximum u'_{rms} of APG and ZPG boundary layers, it is shown that in APG, transition may be triggered earlier by streaks of much lower amplitude. In ZPG, high amplitude Klebanoff streaks are more stable. For the case tu02, breakdown is mostly via inner modes. But outer modes are relevant at high Tu and a few instances of outer mode breakdown are also seen. The Klebanoff streaks, at high Tu, play a dual role. Stronger streaks are receptive to outer streak instability by high frequency free-stream forcing. Furthermore, these stabilize the boundary layer profile diminishing the instability wave growth rate.

Frequent inner breakdowns in APG is not due to an inflectional base profile per se. Present simulations indicate that this is due to inception of instability waves in APG and their high growth rate. At high Tu, the mean profile is of a more favorable pressure gradient boundary layer in which instability waves are less significant. Consequently, the outer mode is the favored bypass mode. At low Tu, outer modes are not seen as in the case tu01 herein, even though the transition route is essentially bypass. Transition beneath low intensity free-stream turbulence is truly mixed mode transition.

CHAPTER 5. CONCLUSIONS

Numerical experimental setup for the study of mixed mode transition for the present work is much more realistic. Simulations and experiments thus far were performed mainly with monochromatic disturbances. Although such simplification helps in identifying the interaction more clearly, such idealization excludes the multi-modal interactions that is very important in the transitional regime. Current simulations of mixed mode transition, specially the simulations of APG boundary layers demonstrate this point. Expectedly, the interaction observed is more complex. Analysis based on DNS data and visualizations have been the basis of qualitative understanding and empirical characterization of various regimes in mixed mode transition in zero and adverse pressure gradient boundary layer flows. Much remains to be understood still, specifically the connection between instability waves and helical breakdown, mechanism of spontaneous appearance of instability waves in adverse pressure gradient and their participation in transition.

5.1 Mixed mode transition in ZPG

Boundary layer under moderate free-stream turbulence ($Tu \leq 2\%$) did not transition up to $Re_x \approx 7.5 \times 10^5$, the exit plane of the computational domain considered. But a TS wave was sufficient to trigger transition well upstream of the exit plane. When the TS mode strength was high $A = 1\%$ at inlet, transition was as early as bypass transition under $Tu = 3.5\%$ intensity free-stream turbulence. This demonstrates the consequence of a modal interaction scenario. General consensus is that bypass transition is the dominant route in ZPG boundary layers. Present direct simulations help in identification of, equally, if not more dangerous apparently innocuous initial disturbance conditions. Moreover, present simulations identify three regimes

of transition in presence of both TS waves and discrete mode. Monochromatic or bimodal disturbances are able to capture only two of those regimes.

The three regimes identified, are based on individual strength of perturbations of the TS mode and free-stream turbulence. At high turbulence intensities, transition is via pure bypass mechanism. The presence of an either strong or weak TS mode slightly accelerates the transition process. The transition is triggered via breakdown of low-speed Klebanoff streaks. Over high amplitude lifted Klebanoff streaks, sinuous type secondary perturbations develop. The secondary instabilities are subharmonic to the streak spanwise wavenumber.

At low turbulence intensities, breakdowns are deep inside the boundary layer. These are governed by 'inner' modes. Two special cases may occur. When the TS mode is strong, formation and breakdown of Λ vortices trigger transition as in Liu et al. (2008a). The secondary instability of the TS wave is forced by the Klebanoff streaks inside the boundary layer. Tip of Λ vortices form on the low-speed streaks due to higher lift-up effect. The spanwise width of these vortices are close to those predicted by Herbert (1988). The pattern of evolving Λ vortices or neither H or K type as the secondary instability is forced by broadband free-stream turbulence.

When both TS mode strength and intensity of turbulence in free-stream are low, breakdown is via formation of helical structures (Bose and Durbin, 2016b). The helices tend to form at the high shear region between streaks when a high speed streak glides over a low-speed speed streak. These were most frequently observed for the case when $Tu = 1\%$ and TS amplitude $A = 0.5\%$ at the inlet. At higher Tu, these are more difficult to identify. This is an unconventional bypass mechanism where TS waves also participate in transition. Perhaps this is the intermediate transition route between secondary instability of TS waves and Klebanoff streaks.

5.2 Mixed mode transition in APG

In APG, discrete modes appear spontaneously experimentally under controlled conditions ($Tu \approx 0.1\%$), see Walker and Gostelow (1989). In the present simulations of APG boundary layer with Hartree parameter $\beta = -0.14$, TS waves were instigated. These waves were obtained in an extended computational domain when free-stream turbulence was not invoked at inlet.

The TS waves were instigated by numerical noise. The instability waves remained 2-D and flow remained laminar within the computational domain considered. The property of the TS waves matched very well with the LST predictions. When free-stream turbulence was prescribed at inlet, these waves appear much earlier. The most dominant TS waves were highly sensitive to the spectral content of the inlet disturbances. The appearance of instability waves is delayed if the inlet disturbances had higher frequencies than the instability waves. The opposite effect takes place when inlet disturbance frequency is brought closer to the linearly unstable frequency range. Once the inlet spectra was fixed, irrespective of Tu, most dominant instability wave was always the same. These facts indicate a nonlinear process involved in generation of these instability waves as opposed to linear mechanisms known thus far (Goldstein, 1983).

The three regimes identified in ZPG are also evident in APG. A major difference being the TS wave is not required to be introduced at the inlet. These grow naturally and participate in transition. Simulations of APG boundary layer transition under various levels of free-stream turbulence showed peculiar behaviour. In experiments performed by Gostelow et al. (1994), the flow transitioned quicker for $Tu = 0.3\%$ compared to $Tu = 1.2\%$. They attributed this puzzling result to quick subharmonic breakdown even though the flow was not otherwise externally forced. In the present simulations for $Tu = 0.1\%$, transition was also triggered by secondary instability of the spontaneously arising TS waves. But due to high local growth of instability waves of different wavelengths, disturbance spectra is broadband prior to secondary instability. Consequently the breakdown is due to broadband TS waves that spawn Λ vortices with irregular shape, size and pattern.

For $Tu = 1\%$, the instability waves evidently participate in the transition process, as the most dominant 2-D instability wave frequency has the highest amplitude in the transitional regime. The spanwise wavenumber spectra in the transitional region also corroborate the same. The instability waves interact with Klebanoff streaks resulting in inception of helical structures that break down to trigger transition. At even higher $Tu = 2\%$, both inner and outer breakdowns are seen. Inception of inner modes could be due to instability waves interacting with Klebanoff streaks. The outer modes are comparatively more frequent at high Tu in APG. Strong Klebanoff streaks are sensitive receptivity spot for secondary perturbation growth. At

the same time, the streaks favorably distort the boundary layer diminishing growth of instability waves. Result is relatively reduced chance of occurrence of inner breakdown. Participation of instability waves in APG even at high Tu implies that almost all transition scenarios in APG are of mixed mode type.

BIBLIOGRAPHY

Abu-Ghannam, B. J. and Shaw, R. (1980). Natural transition of boundary layers – the effects of turbulence, pressure gradient, and flow history. *Journal of Mechanical Engineering Science*, 22:213–228.

Andersson, P., Berggren, M., and Henningson, D. S. (1999). Optimal disturbances and bypass transition in boundary layers. *Phys. Fluids*, 11(1):134–150.

Andersson, P., Brandt, L., Bottaro, A., and Henningson, D. S. (2001). On the breakdown of boundary layers streaks. *J. Fluid Mech.*, 428:29–60.

Batchelor, G. K. and Gill, A. E. (1962). Analysis of the stability of axisymmetric jets. *J. Fluid Mech.*, 14:529–551.

Bhaumik, S. and Sengupta, T. K. (2014). Precursor of transition to turbulence: Spatiotemporal wave front. *Phys. Rev. E*, 89:043018.

Boiko, A. V., Westin, K. J. A., Klingmann, B. G. B., Kozlov, V. V., and Alfredsson, P. H. (1994). Experiments in a boundary layer subjected to freestream turbulence. Part II. The role of TS-waves in the transition process. *J. Fluid Mech.*, 281:219–245.

Borodulin, V. I., Kachanov, Y. S., and Roschektayev, A. P. (2006). Turbulence production in an APG-boundary-layer transition induced by randomized perturbations. *Journal of Turbulence*, 7,N8.

Borodulin, V. I., Kachanov, Y. S., and Roschektayev, A. P. (2011). Experimental detection of deterministic turbulence. *Journal of Turbulence*, 12,N23.

Bose, R. and Durbin, P. (2016a). Helical modes in boundary layer transition. *Phys. Rev. Fluids*, 1:073602.

Bose, R. and Durbin, P. (2016b). Transition to turbulence by interaction of free-stream and discrete mode perturbations. *Phys. Fluids*, 28:114105.

Brandt, L. and de Lange, H. C. (2008). Streak interactions and breakdown in boundary layer flows. *Phys. Fluids*, 20:024107.

Brandt, L., Schlatter, P., and Henningson, D. S. (2004). Transition in boundary layers subject to free-stream turbulence. *J. Fluid Mech.*, 517:167–198.

Brinkerhoff, J. R. and Yaras, M. I. (2015). Numerical investigation of transition in a boundary layer subjected to favourable and adverse streamwise pressure gradients and elevated free stream turbulence. *J. Fluid Mech.*, 781:52–86.

Butler, K. M. and Farrell, B. F. (1992). Three-dimensional optimal perturbations in viscous flow. *Phys. Fluids*, 4(8):1637–1650.

Cossu, C. and Brandt, L. (2002). Stabilization of tollmien-schlichting waves by finite amplitude optimal streaks in the blasius boundary layer. *Phys. Fluids*, 14(8):L57–L60.

Cossu, C. and Brandt, L. (2004). On tollmien-schlichting like waves in streaky boundary layers. *European Journal of Mechanics B/Fluids*, 23:815–833.

Craik, A. D. D. (1971). Nonlinear resonant instability in boundary layers. *J. Fluid Mech.*, 50:393–413.

Crouch, J. D. (1992). Non-localized receptivity of boundary layers. *J. Fluid Mech.*, 244:567–581.

Drazin, P. and Reid, W. H. (1981). *Hydrodynamic Stability*. Cambridge University Press.

Dubief, Y. and Delcayre, F. (2000). On coherent-vortex identification in turbulence. *Journal of Turbulence*, 1, N11.

Durbin, P. A. and Wu, X. (2007). Transition beneath vortical disturbances. *Annu. Rev. Fluid Mech.*, 39:107–128.

Emmons, H. W. (1951). The laminar-turbulent transition in a boundary layer: Part I. *Journal of Aeronautical Science*, 18:490–498.

Fasel, H. F. (2002). Numerical investigation of the interaction of the Klebanoff-mode with a Tollmien-schlichting wave. *J. Fluid Mech.*, 450:1–33.

Fransson, J., Brandt, L., Talamelli, A., and Cossu, C. (2005). Experimental study of the stabilization of tollmien-schlichting waves by finite amplitude streaks. *Phys. Fluids*, 5:1–15.

Fransson, J., Talamelli, A., Brandt, L., and Cossu, C. (2006). Delaying transition to turbulence by a passive mechanism. *Physical Review Letters*, 96(6):064501–4.

Goldstein, M. E. (1983). The evolution of tollmiensclichting waves near a leading edge. *J. Fluid Mech.*, 127:59–81.

Gostelow, J. P., Blunden, A. R., and Walker, G. J. (1994). Effects of free-stream turbulence and adverse pressure gradients on boundary layer transition. *Journal of Turbomachinery*, 116:392–404.

Grosch, C. E. and Salwen, H. (1978). The continuous spectrum of the Orr-Sommerfeld equation. Part 1. The spectrum and the eigenfunctions. *J. Fluid Mech.*, 68:33–54.

Hack, M. J. P. and Zaki, T. A. (2014). Streak instabilities in boundary layers beneath free-stream turbulence. *J. Fluid Mech.*, 741:280–315.

Heisenberg, W. (1951). On stability and turbulence of fluid flows. *Ann. Phys. Lpz.*, pages 577–627. (translated in NACA technical memo 1291).

Herbert, T. (1988). Secondary instability of boundary layers. *Annu. Rev. Fluid Mech.*, 20:487–526.

Hodson, H. P. and Howell, R. J. (2005). Bladerow interactions, transition, and high-lift aerofoils in low-pressure turbines. *Annu. Rev. Fluid Mech.*, 37:71–98.

Hughes, J. D. and Walker, G. J. (2001). Natural transition phenomena on an axial flow compressor blade. *Journal of Turbomachinery*, 123:392–401.

Hunt, J. C. R. and Durbin, P. A. (1999). Perturbed vortical layers and shear sheltering. *Fluid Dynamics Research*, 24:375–404.

Jacobs, R. G. and Durbin, P. A. (1998). Shear sheltering and the continuous spectrum of the Orr-Sommerfeld equation. *Phys. Fluids*, 10(8):2006–2011.

Jacobs, R. G. and Durbin, P. A. (2000). *Bypass transition phenomena studies by computer simulation.* Report no. TF-77, Stanford University, Dept. of Mechanical Engineering.

Jacobs, R. G. and Durbin, P. A. (2001). Simulations of bypass transition. *J. Fluid Mech.*, 428:185–212.

Kambe, T. (1969). The stability of an axisymmetric jet with parabolic profile. *Journal of the Physical Society of Japan*, 26:566–575.

Kendall, J. M. (1985). Experimental study of disturbances produced in a pre-transitional laminar boundary layer by weak freestream turbulence. *AIAA-85-1695.*

Klebanoff, P. S. (1971). Effect of freestream turbulence on the laminar boundary layer (abstract). *Bulletin of the American Physical Society*, 10(11):1323.

Klebanoff, P. S., Tidstrom, K. D., and Sargent, L. M. (1962). The three-dimensional nature of boundary layer instability. *J. Fluid Mech.*, 12:1–24.

Kleiser, L. and Zang, T. A. (1991). Numerical simulation of transition in wall-bounded shear flows. *AnnRev*, 23:495–537.

Landahl, M. T. (1980). A note on an algebraic instability of inviscid parallel shear flows. *J. Fluid Mech.*, 98:243–251.

Leib, S. J., Wundrow, D. W., and Goldstein, M. E. (1999). Effect of free-stream turbulence and other vortical disturbances on a laminar boundary layer. *J. Fluid Mech.*, 380:169–203.

Lessen, M. and Singh, P. J. (1973). The stability of axisymmetric free shear layers. *J. Fluid Mech.*, 60:433–457.

Liu, Y., Zaki, T. A., and Durbin, P. A. (2008a). Boundary-layer transition by interaction of discrete and continuous modes. *J. Fluid Mech.*, 604:199 – 233.

Liu, Y., Zaki, T. A., and Durbin, P. A. (2008b). Floquet analysis of secondary instability of boundary layers distorted by Klebanoff streaks and Tollmien-Schlichting waves. *Phys. Fluids*, 20(124102).

Luchini, P. (2000). Reynolds-number-independent instability of the boundary layer over a flat surface: optimal perturbations. *J. Fluid Mech.*, 404:289–309.

Michalke, A. (1984). Survey on jet instability theory. *Progress Aerospace Science*, 21:159–199.

Mollendorf, J. C. and Gebhart, B. (1973). An experimental and numerical study of the viscous stability of a round laminar jet with and without thermal buoyancy for symmetric and asymmetric disturbances. *J. Fluid Mech.*, 61:367–399.

Morkovin, M. V. (1969). *The many faces of transition.* Viscous Drag Reduction. Plenum Press, New York.

Nagarajan, S., Lele, S. K., and Ferziger, J. H. (2007). Leading-edge effects in bypass transition. *J. Fluid Mech.*, 572:471–504.

Ovchinnikov, V., Choudhari, M. M., and Piomelli, U. (2008). Numerical simulations of boundary-layer bypass transition due to high-amplitude free-stream turbulence. *J. Fluid Mech.*, 613:135–169.

Phillips, O. M. (1969). Shear-flow turbulence. *Annu. Rev. Fluid Mech.*, 1:245–264.

Rosenfeld, M., Kwak, D., and Vinokur, M. (1991). A fractional step solution method for the unsteady incompressible Navier–Stokes equations in generalized coordinate systems. *J. Comput. Phys.*, 94:102–137.

Salwen, H. and Grosch, C. E. (1981). The continuous spectrum of the Orr-Sommerfeld equation. Part 2. Eigenfunction expansions. *J. Fluid Mech.*, 104:445–465.

Saric, W. S., Reed, H. L., and Kerschen, E. J. (2002). Boundary-layer receptivity to freestream disturbances. *Annu. Rev. Fluid Mech.*, 34:291–319.

Sayadi, T., Hamman, C. W., and Moin, P. (2013). Direct numerical simulation of complete H-type and K-type transitions with implications for the dynamics of turbulent boundary layers. *J. Fluid Mech.*, 724:480–509.

Schlatter, P., Brandt, L., de Lange, H. C., and Henningson, D. S. (2008). On streak breakdown in bypass transition. *Phys. Fluids*, 20:101505.

Schlichting, H. (1933). Zur entstehung der turbulenz bei der plattenstromung. *Nachr. Ges. Wiss.*, pages 182–208.

Schmid, P. J. and Henningson, D. S. (2001). *Stability and Transition in Shear Flows*. Springer.

Schubauer, G. B. and Skramstad, H. (1947). Laminar boundary layer oscillations and transition on a flat plate. *Journal Res. Nat. Bur. Standards*, 38:251–292.

Tollmien, W. (1929). Über die entstehung der turbulenz. *Nachr. Ges. Wiss. Göttingen*, pages 21–44. (translated in NACA technical memo 609).

Vaughan, N. J. and Zaki, T. A. (2011). Stability of zero-pressure-gradient boundary layer distorted by unsteady Klebanoff streaks. *J. Fluid Mech.*, 681:116–153.

Voke, P. R. and Yang, Z. (1995). Numerical study of bypass transition. *Phys. Fluids*, 7(9):2256–2264.

Walker, G. J. and Gostelow, J. P. (1989). Effects of adverse pressure gradients on the nature and length of boundary layer transition. *Journal of Turbomachinery*, 112:196–205.

Westin, K. J. A., Boiko, A. V., Klingmann, B. G. B., Kozlov, V. V., and Alfredsson, P. H. (1994). Experiments in a boundary layer subjected to freestream turbulence. Part I. Boundary layer structure and receptivity. *J. Fluid Mech.*, 281:193–218.

White, F. M. (1991). *Viscous Fluid Flow*. McGraw-Hill, Inc., 2nd edition.

Zaki, T. and Durbin, P. A. (2006). Continuous mode transition and the effects of pressure gradient. *J. Fluid Mech.*, 563:357–388.

Zaki, T., Wissink, J., Rodi, W., and Durbin, P. (2010). Direct numerical simulations of transition in a compressor cascade: the influence of free-stream turbulence. *Journal of Fluid Mechanics*, 665:57–98.

Zaki, T. A. and Durbin, P. A. (2005). Mode interaction and the bypass route to transition. *J. Fluid Mech.*, 531:85–111.